UNIVERSITÀ DEL SALENTO

FACOLTÀ DI SCIENZE MATEMATICHE FISICHE E NATURALI

DOTTORATO DI RICERCA IN FISICA
XX CICLO

TESI DI DOTTORATO

ZINC OXIDE NANOSTRUCTURED FILMS GROWN BY PULSED LASER DEPOSITION FOR OPTICAL GAS SENSING APPLICATIONS

Tutori:

Ch.mo Prof. MAURIZIO MARTINO

Dr. MAURO LOMASCOLO

Dottorando:

DANIELE VALERINI

Lecce, 2008

Index

Introduction

Nanostructured zinc oxide (ZnO) has attracted a great attention over the recent years because of its interesting properties making this kind of material particularly appealing for a wide range of applications in several technological fields.

Indeed ZnO is a very attractive material thanks to its features, like wide band gap, large exciton binding energy, chemical stability, biocompatibility, piezoelectricity, nonlinear optical effects, radiation hardness. Moreover, when passing from bulk material to nanostructures, the interest is highly enhanced, since the properties deriving from the reduced dimensionality of nanostructures add to the intrinsic ZnO properties. Furthermore, the intense studies in this research field are promoted by the possibility to realize a huge variety of ZnO nanostructures, such as dots, wires, rods, tetrapods, belts, tubes, needles, hierarchical structures and so on.

ZnO, as bulk material or film, is very appealing for electronic and opto-electronic devices, such as Ohmic contacts [1], Schottky contacts [2], LEDs [3], LASERs [4], transparent FETs [5], photodetectors [6], solar cells [7]. In addition, thanks to their properties, semiconductor nanostructures represent a matter of very intensive research activities for opto-electronics [8, 9]. Dealing with ZnO nanostructures a lot of different possible electronic and opto-electronic applications have been explored. Realization of nano-contacts by evaporation of different metals onto ZnO nanostructures has been reported, showing the possibility to obtain Ohmic or Schottky contact behaviors [10]. Electroluminescence for LED applications has been extensively studied with devices based both on ZnO nanorod arrays [11, 12] and on single ZnO nanorod [13]. Thanks to ZnO high refractive index (~ 2.0) and to the well-faceted ends of the nanowires acting as reflecting mirrors, ZnO nanowires work as ideal optical resonance cavities; indeed lasing

action at room temperature has been demonstrated on ZnO aligned nanorod arrays [14, 15] and single nanorods [16], but also in random oriented nanorod arrays [17] and other nanostructures [18, 19]. Even random lasing in ZnO nanoparticle films has been studied [20]. Field effect transistors (FETs) based on single ZnO nanorods [21, 22], nanobelts [23], and hybrid ZnO tetrapods/polymer blends [24] have been realized. ZnO nanorods/nanowires have been studied for applications as ultraviolet photodetectors and optical switches [25, 26]. UV photodiodes based on ZnO nanotetrapods with Schottky contacts have been reported [27]. In view of possible applications of ZnO nanostructures to solar cells, it is believed that aligned nanorods can highly improve the solar energy conversion efficiency through a faster electron transport than conventional solar cells; for this reason many studies are conducted towards this potential application [28, 29]. By combinations of metal-semiconductor Schottky diodes or FETs, ZnO nanorods have been also used to realize logic circuits [30].

Due to its high refractive index ZnO is also useful for optical waveguides thus, for example, light can be guided inside a nanowire, acting like an optical nano-fiber, and this is particular appealing for nanoscale photonics integration [31]. Even light coupling between nanostructures of different materials (like ZnO and SnO_2) has been reported [31].

Since zinc oxide presents strong piezoelectric properties [32] it appears to be suitable for electro-mechanical transducers, sensors and actuators [33] and for surface acoustic wave (SAW) devices [34]. For example ZnO piezoelectricity has been exploited to realize pressure sensors [35]. Also pyroelectricity is observed in ZnO, so this property makes possible to realize pyroelectric sensors [36]. Piezoelectric properties of ZnO nanostructures have been widely explored [37]. A method to convert mechanical energy into electrical energy through piezoelectricity of ZnO nanowires has been showed [38], suggesting the possibility to convert biological mechanical energy, acoustic vibration energy, and bio-fluid hydraulic energy into electricity at nanoscale levels. Piezoelectricity can be also used for pressure or force sensors: for example, in a single nanowire FET a variation of pressure or a force acting on the wire cause its bending and thus a consequent change in the current-voltage characteristic of the FET, which can be measured [39] and related to the pressure variation or applied force. ZnO nanostructures are also interesting

for use as nano-cantilevers [40], for example for atomic force microscopy (AFM), thanks to their piezoelectric properties and smaller dimensions than conventional cantilevers (e.g. made of Si_3N_4 and SiC).

Bulk zinc oxide and films have also shown large nonlinear optical coefficients, suggesting its potential application in quantum electronics and integrated optical devices. Second harmonic generation (SHG) in bulk ZnO [41] and films [42] and third harmonic generation (THG) [43] have been reported, hence showing the possibility to use this material, which is cheaper and easier to be integrated than other nonlinear optical single crystals like $LiNbO_3$ and $LiTaO_3$, in this technological field. Optical nonlinearity has been studied also in ZnO nanostructures; for example SHG and THG have been reported for ZnO nanowires [44].

Ferromagnetism in zinc oxide doped with transition metals, like e.g. Mn and Co, has been experimentally evidenced at room temperature [45] and theoretically studied [46], thus showing the possible appliance of doped ZnO in spintronics [47].

Another useful ZnO property is its radiation hardness [48, 49], making it interesting for devices to be used in space applications.

Zinc oxide is also biosafe and biocompatible [50]. This feature supports the possible use of ZnO for biomedical applications without the need to add a protective coating.

The possibility to realize very ordered arrays of ZnO nanostructures is particularly useful for realization of photonic crystals. Theoretical and experimental results have shown the possibility to obtain photonic structures for example by means of ZnO inverted opals [51] and ZnO nanopillar arrays [52].

Another very interesting possible application of ZnO nanostructures is as field emitters to be used, for example, for flat panel displays, cold cathodes and other photoelectric devices. Oxide nanostructures may have high efficiency, reduction of cost and device sizes in comparison with conventional thermo-ionic emitters, and they are more stable in harsh environment and controllable in electrical properties compared, for example, to carbon nanotubes [53]. The great interest derives also from the fact that many nanostructures have a needle-like tip, so that the electron field emission is highly enhanced due to the local field enhancement on their tips. Several reports exist about field

emission from different ZnO nanostructure arrays, such as nanowires [53], nanopencils [54], nanoneedles [55], nanotubes [56], nanotetrapods [57] and other nanostructures [58, 59]. Also the field emission properties of hybrid arrays of ZnO nanorods and carbon nanotubes [60] and of individual ZnO nanowires [61] have been studied.

Other possible applications of ZnO nanostructures are related to their wettability properties, since hydrophilic or hydrophobic materials are interesting for several applications, like in microfluid devices, chemical sensors or biosensors and for industrial uses like cleaning, drying etc. Conversion from hydrophobic to hydrophilic surface of ZnO nanorod arrays by UV illumination [62] or by oxygen plasma treatment or annealing [63] have been reported.

Certainly one of the most attractive applications of zinc oxide is for chemical or biological sensors. Thanks to their properties, semiconductor nanostructures are a subject of intensive studies in this technological field [64, 65]. The use of ZnO for sensing applications is discussed in more details in paragraphs 4.1 and 4.2.

As a consequence of all the possible applications mentioned above, it is clear that a great interest towards ZnO nanostructures arose in the last years. Evidence of this great interest is also showed by the huge number of papers and reviews dealing with zinc oxide and its nanostructures in the last years (see e.g. [66] and refs. therein).

The intense attention in this research field is also promoted by the possibility to grow ZnO nanostructures with excellent crystal quality by using several different techniques (see par. 1.3), thus allowing the possible realization of low-cost good-quality devices. Some of these techniques are thermal evaporation, chemical vapor deposition (CVD), laser ablation (or pulsed laser deposition, PLD), electrodeposition, hydrothermal methods and other solution-based techniques, sputtering, molecular beam epitaxy (MBE), template-directed methods.

In particular, PLD is known to be a suitable technique to realize good quality ZnO films and nanostructures. This technique is relatively simple and versatile and it is reported to be able to employ lower temperatures for the growth of nanostructures with respect to other methods like thermal evaporation. Moreover the deposition of multiple layers of different materials or the doping process *in situ* are easy aims by means of this

technique. The number of publications dealing with ZnO nanostructures grown by using this deposition technique greatly rose in the last few years, since PLD represents a very interesting method which allows the easy and high quality growth of such structures.

The great interest towards ZnO and its nanostructures and the possibility to grow them by the relatively simple PLD technique are the central keys of the research activity conducted during the Ph.D. course whose results are presented in this Thesis. Here excimer laser ablation has been used to grow ZnO films and nanostructures; the experimental set-up has been opportunely modified to allow the deposition of such structures. The changes in the morphology of the samples grown using different deposition parameters have been studied by Scanning Electron Microscopy - Field Emission Gun (SEM-FEG), and some discussions about the possible growth mechanisms are reported. For some samples also Energy Dispersive X-ray Spectroscopy (EDS or EDX), Rutherford Backscattering Spectroscopy (RBS), and X-Ray Diffraction (XRD) measurements have been reported in order to gain information about the sample quality. The photoluminescence (PL) properties of the deposited samples have been studied at room and low temperature and also a study of the temperature dependence of the PL properties has been conducted; these analyses allowed to show the high quality of the deposited samples, to deduce the origin of several emission peaks and to obtain information about the recombination mechanisms. Finally, an experimental set-up has been arranged for optical gas sensing measurements; for some samples, preliminary gas sensing measurements by quenching of the photoluminescence intensity have been performed, in order to examine the possible application of the obtained materials in the gas sensing field.

This Thesis is organized in four chapters:

» *First Chapter – "General properties"*

The first chapter represents a general overview on the properties which make zinc oxide and its nanostructures remarkably interesting for all the

applications mentioned in this introduction, and on the different growth techniques employed for the realization of this kind of materials.

» *Second Chapter – "Zinc oxide growth by Pulsed Laser Deposition"*

This chapter is focused on the ZnO growth performed during this research activity by Pulsed Laser Deposition. A summary of some reports in literature about PLD of ZnO nanorod/nanowire arrays is presented as a starting-point for the following depositions of this research activity. Then the description and discussion about the deposited samples are conducted on the base of the sample morphology observed by SEM investigations.

» *Third Chapter – "Compositional and structural analyses and photoluminescence measurements"*

This chapter shows some analyses performed on the deposited samples in order to get information about their quality and properties. Some compositional and structural properties are investigated by EDS, RBS and XRD analyses. The photoluminescence properties are studied at room and low temperature and also a study of the temperature dependence of the PL emission is shown from 7 K to room temperature, allowing to obtain significant information about sample quality and recombination processes.

» *Fourth Chapter – Optical sensing*

The preliminary nitrogen dioxide (NO_2) sensing measurements based on quenching of the PL intensity performed on some deposited samples are shown in this chapter. Before these results, an overview is presented about the sensing applications of bulk ZnO, films and nanostructures in literature.

In a brief summary, this Ph.D. Thesis has the importance to: report the growth of different ZnO nanostructures as well as smooth and rough films by PLD, comparing the depositions made by using two different excimer laser wavelengths (248 nm or 193 nm) for the target ablation; to report some compositional, structural and optical analyses showing the high quality of the deposited samples and allowing to deduce information about some fundamental properties; to test the possibility to use some of the deposited samples for technological applications in the gas sensing field. Additionally, some of the obtained structures (like hexagonal hierarchical structures and pencils) could be very interesting for some technological applications such as field emitters and chemical and biological sensors. The possible growth mechanisms of the deposited samples are discussed together with the possible reasons of the very different morphological and optical properties of the samples deposited by using the two different ablating wavelengths. The comparisons between depositions by using these two different wavelengths represent a significant result of this Thesis. Besides the comparison between the two ablating wavelengths, the PL measurements, together with the study of the temperature dependence of the PL properties, show the high quality of the samples and help to confirm some features reported for ZnO PL emission. Finally, preliminary studies about one of the possible applications (gas sensing) of the deposited samples are presented: low concentrations (down to 3 ppm) of nitrogen dioxide are detected and some observations about probable incomplete reversibility of NO_2 adsorption are discussed.

The research activity presented in this Thesis has been conducted in cooperation between the L^3-group in the Physics Department of the University of Salento in Lecce and the Institute for Microelectronics and Microsystems of the National Research Council (IMM-CNR) – Department of Lecce.

Chapter I
General properties

Chapter 1 - Overview

This chapter aims to present a general outline on the properties and growth techniques of zinc oxide and its nanostructures.

In the first paragraph some information are given about ZnO crystal structure and about some useful properties for technological applications of bulk ZnO and ZnO nanostructures.

Then, in the second paragraph, some details are presented about ZnO photoluminescence properties. The general features of bulk ZnO photoluminescence, such as excitonic emission and defect emission, are shown; then, some important features observable in photoluminescence of ZnO nanostructures, like surface exciton emission, are introduced.

The last paragraph presents a list of some growth methods used for the realization of ZnO nanostructures. Some information for each technique and some examples are reported.

1.1 General properties of ZnO and its nanostructures

Zinc Oxide (ZnO) is a II-VI semiconductor which can crystallize in three different crystal structures: hexagonal wurtzite, cubic zinc-blend and cubic rocksalt. At ambient conditions the stable phase is wurtzite (**Fig. 1.1**), while the zinc-blend structure can be obtained by appropriate growth on cubic substrates and the rocksalt structure can be obtained at relatively high pressures [67].

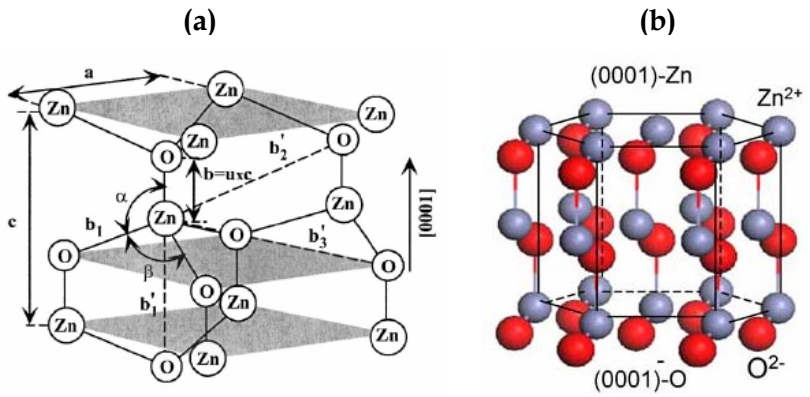

Fig. 1.1. Two schematic representations of the ZnO wurtzite crystal structure. (Image **(a)** from ref. [67]. Image **(b)** from ref. [50]).

For a ZnO ideal wurtzite crystal structure, the ratio between the two lattice parameters of the hexagonal unit cell is $c/a = 1.633$, and the displacement b between the two hexagonal close-packed (hcp) sublattices along the c-axis is 0.375 times the c parameter. In real ZnO crystals the wurtzite structure slightly deviates from the ideal arrangement, by changing the c/a ratio or the u value (where $b=u \cdot c$). In the ZnO crystal structure every atom of one kind (for example O) is surrounded by four atoms of the other kind (Zn), coordinated at the edges of a tetrahedron, therefore the ZnO structure can be described as a sequence of alternating planes composed of tetrahedrally coordinated O^{2-} and Zn^{2+} ions, alternated along the c-axis. The angles α and β of the tetrahedron in the ideal cell are 109.47°. In **Tab. 1.1** the wurtzite ZnO lattice parameters are reported, together with some other useful properties.

Property	Value
Lattice parameters at 300 K	
a_0	0.324 95 nm
c_0	0.520 69 nm
a_0/c_0 (*)	1.602 (ideal hexagonal structure shows 1.633)
u	0.345
Density	5.606 g cm^{-3}
Stable phase at 300 K	Wurtzite
Melting point	1975 °C
Thermal conductivity	0.6, 1–1.2
Linear expansion coefficient (/C)	a_0: 6.5×10^{-6}
	c_0: 3.0×10^{-6}
Static dielectric constant	8.656
Refractive index	2.008, 2.029
Energy gap	3.4 eV, direct
Intrinsic carrier concentration	$<10^6$ cm^{-3}
Exciton binding energy	60 meV
Electron effective mass	0.24
Electron Hall mobility at 300 K for low n-type conductivity	200 cm^2 V^{-1} s^{-1}
Hole effective mass	0.59
Hole Hall mobility at 300 K for low p-type conductivity	5–50 cm^2 V^{-1} s^{-1}

Tab. 1.1. Some zinc oxide properties. (Table from ref. [68]). (*) It should be c_0 / a_0.

As told in the introduction of this Thesis, two zinc oxide properties interesting for many technological applications are its direct wide band-gap (energy gap E_g ~ 3.37 eV at room temperature) and large exciton binding energy* (~ 60 meV) [67].

The wide band-gap makes ZnO suitable for opto-electronic devices operating in the UV-blue spectral range and transparent to the visible light, while the high exciton binding energy, much higher than the thermal energy (~ 26 meV at 300 K) can ensure the exciton stability also at room temperature (RT), thus allowing, for example, a high luminescence efficiency at RT. The large exciton binding energy makes ZnO more interesting than other wide band-gap semiconductors used for UV-blue opto-electronic devices like GaN (E_g ~ 3.39 eV at 300 K) having a lower exciton binding energy ~ 25 meV. Another advantage of ZnO over GaN is the higher commercial availability of bulk single crystals, due to a simpler crystal-growth technology, resulting in a possible lower cost of ZnO-based devices [67, 49].

* Energy needed to separate an electron and a hole of an exciton.

In addition, usually ZnO has an intrinsic n-type conductivity, mainly due to native defects such as oxygen vacancies or zinc interstitials in the crystal lattice. This n-type conductivity can be easily further increased, by intentionally increasing the presence of oxygen vacancies during the growth process or by doping with Al, Ga or In atoms. On the contrary, p-type conductance is less easily obtainable, but doping that allows to gain such kind of conductivity has been reported [69].

All the features mentioned above make ZnO very appealing for electronic and opto-electronic devices: many of these applications have been listed in the introduction.

Moreover the tetrahedral coordination in ZnO crystal structure results in the non-centrosymmetric wurtzite structure which, combined with a large electro-mechanical coupling, causes ZnO to present strong piezoelectric properties. Therefore many studies have been reported about possible technological applications exploiting these piezoelectric properties, as showed in the introduction of this thesis.

Bulk zinc oxide and ZnO films also present other interesting properties (nonlinear optical effects, radiation hardness, biocompatibility, ferromagnetism through doping, etc.) which can be usefully employed in many different technological applications, as reported in the introduction. For an extensive review about ZnO properties, like mechanical, thermal and electrical properties see for example ref. [67].

In addition, when ZnO is provided in nanostructured forms, the interest is highly enhanced, since the properties deriving from the reduced dimensionality of nanostructures add to the intrinsic ZnO properties.

Among the interesting properties deriving from nanostructures, the importance of their surface should be mentioned. Indeed nanostructures have a high surface-to-volume ratio, thus greatly enhancing the properties related to surface states with respect to the corresponding bulk material or non-nanostructured films. Looking to gas or biological sensing applications, it is evident that species binding to the surface of a nanostructure have influence on the electrical or optical properties of the whole nanostructure, while in bulk materials or films only the superficial layers are affected. For example, molecules binding to the surface of a nanowire lead to a charge-carrier depletion or accumulation region which extends till the inner part of the structure, compared with only the surface

region of a planar device [70]. In addition it should be noticed that nanostructure arrays have also a higher global surface than that one of a non-nanostructured film having the same thickness and area, thus allowing a much higher number of available sites for adsorption of the incoming molecules. As a consequence of these features, nanostructures may be more and more sensitive than the corresponding non-nanostructured material and they also allow a further miniaturization of technological devices.

Additionally, quantum confinement effects (such as quantization of the charge-carrier energy levels and possible tuning of the energy gap, increased probability of the energetic transitions, etc.) may appear when nanostructure dimensions are comparable to the exciton Bohr radius of the constituting material, thus further enhancing the possible usefulness in technological devices. Anyway it must be underlined that quantum confinement effects are hardly obtainable in zinc oxide nanostructures, due to the very small Bohr radius of the exciton in ZnO (~ 1.8 nm). However quantum confinement in ZnO nanostructures has been reported in literature [71-73].

1.2 Photoluminescence properties

1.2.a General features about zinc oxide photoluminescence

A typical high-quality ZnO photoluminescence (PL) spectrum usually presents two main features: an UV emission centered at about 375 nm (~ 3.31 eV) at room temperature and one or more visible bands going from the blue to the orange-red region. A typical ZnO photoluminescence spectrum is reported as an example in **Fig. 1.2(a)**.

Both the former emission, here called *excitonic emission* (or *near band-edge emission*), and the latter one, usually associated with emission from defects or impurities and here called *defect emission*, are briefly described below.

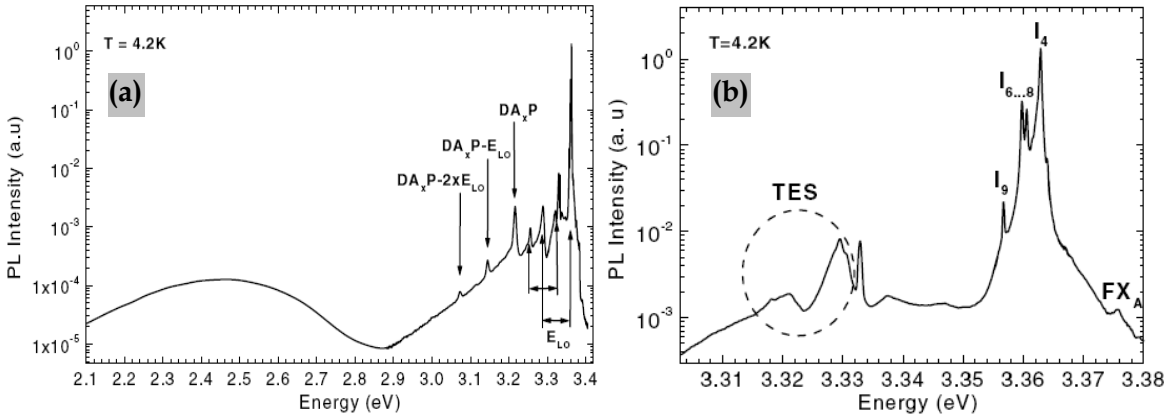

Fig. 1.2. Typical ZnO PL spectra at T = 4K. **(a)** Whole range from 2.1 to 3.4 eV; the DAP peak and some phonon replicas are indicated (see text for details) **(b)** Excitonic range (see text for details). (Images from ref. [74]).

- *Excitonic emission (near band-edge emission)*

As told before, zinc oxide is a direct band gap semiconductor crystallizing in the wurtzite crystal structure. The valence band is six-fold degenerate, but the spin-orbit coupling partially removes this degeneracy, splitting one sub-band, and due to the wurtzite crystal structure the crystal field splitting separates the other two sub-bands; therefore the valence band is constituted by the three two-fold degenerate sub-bands, named *A* (heavy hole band), *B* (light hole band) and *C* (crystal-field split band).

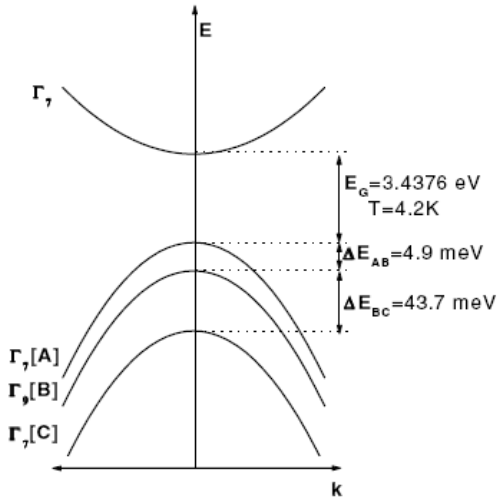

Fig. 1.3. Schematic representation of the ZnO band structure near the band-gap. (Image from ref.[74])

In **Fig. 1.3** the ZnO band structure near the band-gap is schematized, together with the values of the energy gap E_g and of the splitting of the three sub-bands at temperature of 4.2 K [74].

In **Tab. 1.2** the values of energy gap, band splitting and other properties of wurtzite ZnO are reported.

Usually, at low temperatures (~ 10 K) excitons are bound to donors or acceptors in ZnO lattice and PL emission comes predominantly by their recombination. This luminescence is called *bound exciton* (*BX*) emission and it is placed at energies (~ 3.36-3.38 eV, ~ 366-369 nm, at low temperature) slightly lower than ZnO energy gap. The chemical nature of donor and acceptor species in zinc oxide is not still fully determined, as atoms of many different impurities may act as donors/acceptors, but also lattice defects may do the same: for example zinc vacancies may act as acceptors and oxygen vacancies as donors. More than eleven *BX* recombinations have been observed (see [74] and refs. therein) and they are usually labeled with notations from I_0 to I_{11} (some of them are visible in the spectrum of **Fig. 1.2(b)**). In bulk ZnO usually the most intense peak is attributed to the I_4 transition and assigned to excitons bound to a neutral donor; this is usually called *neutral-donor-bound exciton* and often indicated as D^0X.

Free exciton (*FX*) emission (~ 3.38-3.40 eV, ~ 364-367 nm, at low temperature), coming from recombination of excitons not bound to donors/acceptors and thus from conduction and valence band-edges, begins to be significant when thermal energy of excitons is high enough to allow their un-binding from donors/acceptors; thus, when the temperature increases, dissociation of *BX* into *FX* may happen (see par. 3.2.d). Because of the three valence sub-bands, three *FX* emissions may occur from the conduction band to the *A*, *B* and *C* bands; these transitions are denoted with FX_A , FX_B and FX_C respectively, but the FX_C transition is hardly observed in PL spectra since it is theoretically forbidden for some light polarizations [75, 67]. Moreover it must be taken into account that free excitons may also exist in their excited states, having energies about 40-45 meV higher than the respective ground states [75, 76].

In addition, apart of *BX* and *FX* transitions, other emission peaks can be observed in the UV region of ZnO PL spectra.

E_{gA}	3.437 eV	(T = 1.6 K)
E_{AB}	4.9 meV	
E_{BC}	43.7 mev	
E_{gB}	3.4425 eV	
E_{gC}	3.4813 eV	
Temperature dependence of the band gap up to 300 K		
$E_g(T) = E_g(T=0) \frac{5.05 \cdot 10^{-4} \cdot T^2}{900 - T}$		
Dielectric constants		
$\varepsilon(0) \perp c$	7.8	
$\varepsilon(0) \parallel c$	8.75	
$\varepsilon(\infty) \perp c$	3.7	
$\varepsilon(\infty) \parallel c$	3.75	
Electron effective (polaron) mass in units of m_0		
$m_e^* \parallel$	0.28	
$m_e^* \perp$	0.24	
Hole effective mass in units of m_0		
m_h^* (A)	$0.59 \parallel = \perp$	
m_h^* (B)	$0.59 \parallel = \perp$	
Crystal field splitting in meV		
Δ_{cf}	41.7	
Spin orbit splitting in meV		
Δ_{so}	−8.0	
Electron g-values		
$g_e^{\parallel}$	1.956 – 1.958	
$g_e^{\perp}$	1.955 – 1.956	
Hole g-values		
$g_A^{\parallel}$	−2.45	
$g_A^{\perp}$	0.09	
$g_B^{\parallel}$	1.5	
$g_B^{\perp}$	0	
$g_C^{\parallel}$	1.95	
$g_C^{\perp}$	1.91	
Landé g-factors for the hole participating in the 1S exitons		
$g_A^{\parallel}(1S)$	−1.32	
$g_B^{\parallel}(1S)$	3.04	
$g_C^{\parallel}(1S)$	1.06	
Phonon modes at T = 300 K in cm^{-1}		
E_2^{low}	101	
E_2^{high}	437	
TO (A_1)	380	
LO (A_1)	574	
TO (E_1)	591	

Tab. 1.2. Energy gap, band splitting and other properties for wurtzite zinc oxide. (Table from ref. [74]).

A characteristic transition in ZnO PL spectra is the *two-electron satellite* (*TES*) recombination of the neutral-donor-bound exciton: in the recombination of an exciton bound to a neutral donor, the donor final state can be the *1s* state (giving the normal D^0X line) or the *2s,2p* state (giving the *TES* line). Therefore the energetic separation between the D^0X and its *TES* is the difference between the donor energies in the *2p* and *1s* states, which in first approximation, by using the hydrogenic effective mass approximation (EMA), is ¾ of the donor binding energy. By introducing further corrections to the hydrogenic EMA, more accurate values of this energy separation can be calculated [74].

In **Tab. 1.3** there is a list of values of FX_A energies, BX ($I_0 - I_{11}$) energies and their *localization energies* (defined as the energetic separation from the FX_A), *TES* separation from the respective donor-bound exciton, donor binding energies, and chemical identity of the donors for bulk ZnO. Some of these peaks are visible in the PL spectrum reported in **Fig. 1.2(b)**.

line	wavelength (nm)	energy (eV)	localisation energy (meV)	two-electron-satellite separation ($2P_{xy} - 1S$) (meV)	donor binding energy (meV)	chemical identity
A_L^*	367.12	3.3772				
A_T^*	367.26	3.3759				
I_0	367.63	3.3725	3.4			
I_1	367.71	3.3718	4.1			
I_{1a}	368.13	3.3679	8.0			
I_2^{**}	368.19	3.3674	8.5			
I_3^{**}	368.29	3.3665	9.4			
I_{3a}	368.34	3.3660	9.9			
I_4	368.34	3.3628	13.1	34.1	46.1	H
I_5	368.86	3.3614	14.5			
I_6	368.92	3.3608	15.1	38.8	51.55	Al
I_{6a}	368.96	3.3604	15.5	40.4	53	
I_7	369.01	3.3600	15.9			
I_8	369.03	3.3598	16.1	42.1	54.6	Ga
I_{8a}	369.08	3.3593	16.6			
I_9	369.37	3.3567	19.2	50.6	63.2	In
I_{10}	369.76	3.3531	22.8	60.2	72.6	
I_{11}	370.28	3.3484	27.5			

* A_L and A_T are the longitudinal and transversal free A-exciton states. A_T is the reference for the determination of the bound excition localisation energy.
** I_2 and I_3 are assigned to ionised donor bound exciton recombinations.

Tab. 1.3. *A*-free exciton and bound exciton energies and related properties. (Table from ref. [74]).

Another characteristic PL peak comes from the *donor-acceptor pair* transition, labeled as *DAP* [74, 76, 77], due to recombination from donor to acceptor levels.

In addition to all the transitions reported above, also some of their phonon replicas are usually clearly visible in the PL spectra, due to interactions of excitons with longitudinal optical (*LO*) or transversal optical (*TO*) phonons. The phonon energies in zinc oxide are $E_{LO} \sim 72$ meV and $E_{TO} \sim 51$ meV, therefore in the PL spectra phonon replicas may appear at energies lower than the respective primary peak, with a separation equal to E_{LO} or E_{TO} (when a single exciton-phonon scattering event occurs) or multiples or combinations of E_{LO} and E_{TO} (when multiple exciton-phonon scattering events occur). Some phonon replicas of the *BX* and *DAP* transitions are clearly visible in the photoluminescence spectrum reported in **Fig. 1.2(a)**.

It is important to observe that usually, also at low temperatures, not all the peaks mentioned above are clearly visible or identifiable since many of them (like the different transitions associated with bound excitons) are very close to one other; therefore generally the whole fine structure of the UV emission can only be observed on high-quality crystals, at very low temperatures and by using set-ups with high spectral resolution. At high temperatures the whole fine structure cannot be observed anyway, since the emission linewidths of the different transitions are broad due to exciton-phonon interaction, thus their overlap results in a broad PL spectrum. As a consequence, at room temperature the excitonic emission in the PL spectrum is mainly constituted by the *FX* emission and its phonon replicas.

More details about the temperature dependence of the PL measurements are reported in par. 3.2.d.

- *Defect emission*

Emission coming from defects in ZnO (here the term "defect" is intended as both lattice defects or impurities) is a very controversial and discussed subject, since a lot of different explanations have been proposed for this emission, occurring in the range going from the violet-blue to the orange-red region [67, 78 and ref. therein].

Usually the PL defect emission is considered composed by three spectral regions: green, yellow and orange-red.

The nature of the green band, usually centered at about 500-540 nm (~ 2.3-2.5 eV), is a very controversial topic. This band is often attributed to singly ionized oxygen vacancies [79-82], but other proposed hypotheses are antisite oxygen [83], Cu impurities [84], or also other attributions have been proposed [67, 78]. Anyway in literature it is reported that green emission appears to originate from the first layers on the sample surface, and not from deep regions inside the material [82, 78].

The yellow band has been attributed to oxygen interstitial levels observed at ~ 590 nm (~ 2.1 eV) at RT [81] or to Li impurities [85].

The orange-red band has been observed at ~ 630-650 nm (~ 1.9-2 eV), and up to the near infrared, in oxygen-rich ZnO and ascribed to oxygen interstitials [82, 86].

In addition to the three bands discussed above, sometimes a violet and blue/green emission has also been observed. It has been attributed to transitions from zinc interstitial levels to the valence band (~ 413 nm ~ 3 eV at 10 K in ref. [87], and ~ 420 nm ~ 2.94 eV at RT in ref. [83]), or from the conduction band to zinc vacancy levels (~ 413 nm ~ 3 eV in ref. [88], and ~ 405 nm ~ 3.06 eV in ref. [81] at RT) or from zinc interstitial levels to zinc vacancy levels (~ 477 nm ~ 2.6 eV at RT) [89]. In all these cases, this band has been attributed to zinc-related defects.

As a consequence of the previous observations, it is evident that the nature of the species giving rise to the defect emission in ZnO is very complex. This complexity is also demonstrated by the presence of a lot of publications in literature showing band diagrams with defect energy levels slightly differing from one paper to another. Some band diagrams reporting the defect levels inside the ZnO energy-gap can be found in refs. [89-91, 66, 87]. In **Fig. 1.4** the calculated defect energy levels in ZnO from different literature sources are reported together with their energy position measured from the bottom of the conduction band: V_{Zn}, V_{Zn}^{-} and V_{Zn}^{2-} denote neutral, singly charged, and doubly charged zinc vacancies, respectively; Zn_i^0 and Zn_i indicate neutral zinc interstitials, while Zn_i^+ denotes a singly charged zinc interstitial; V_O^0 and V_O denote neutral oxygen vacancies,

while V_O^+ denotes a singly charged oxygen vacancy; O_i represents an oxygen interstitial; $V_O Zn_i$ denotes a complex of an oxygen vacancy and zinc interstitial.

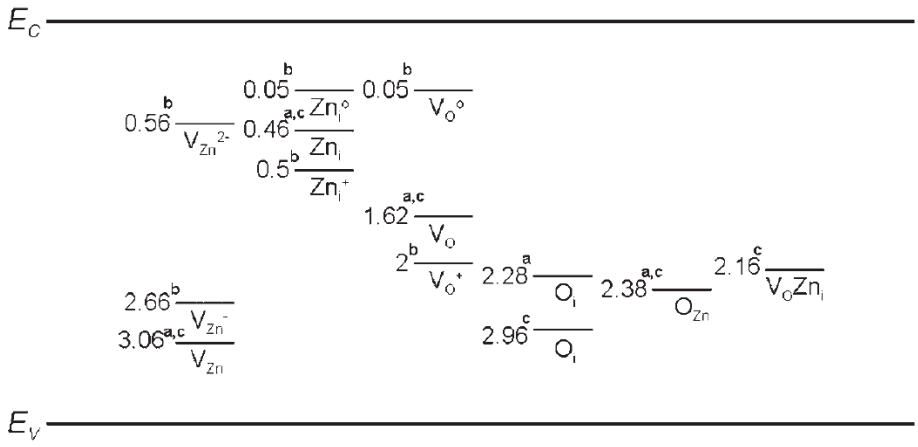

Fig. 1.4. Illustration of the calculated defect energy levels in ZnO from different literature sources. (Image from ref. [78]; superscripts *a*, *b* and *c* are related to literature sources in ref. [78]).

1.2.b Photoluminescence properties of zinc oxide nanostructures

All the PL properties discussed in the previous paragraph for bulk ZnO stand for its nanostructures too. That is, in a brief summary:

- The typical PL spectrum presents two main bands, namely the UV band (near band-edge emission) and the visible band (defect emission);
- The near band-edge emission results from several transitions, including free exciton *FX* emission and bound exciton *BX* emission (usually reported to come mainly from neutral-donor-bound excitons D^0X), together with other peaks like *TES*, *DAP* and phonon replicas;
- The *BX* emission dominates at low temperature, while at high temperature, due to *BX* thermal dissociation into *FX*, free exciton emission prevails together with its phonon replicas.
- The nature of the visible emission is controversial, but it is usually believed to come mainly from zinc-related defects (violet-blue band), singly ionized oxygen vacancies (green band) and oxygen interstitials (yellow and orange-red-NIR);

In addition to the general PL properties summarized above, other features must be underlined for ZnO nanostructures.

As observed for bulk ZnO, also for its nanostructures it appears from literature that green emission comes mainly from the first layers of the material [78 and refs. therein].

If the nanostructure dimensions are comparable with the Bohr radius of the exciton, then a blue-shift of the near band-edge emission can appear as a consequence of the increasing of the band-gap due to quantum confinement effects [71-73].

An important feature often observed in the PL spectra of ZnO nanostructures is the appearing of a peak not observed in bulk ZnO. This peak, sometimes visible only as a shoulder near the *BX* emission, is usually attributed to emission from excitons bound to surface states [92-95] and thus called *surface exciton* (*SX*) emission. This occurrence can be explained by considering that in small nanostructures the surface-to-volume ratio becomes very high, and so the influence of the emission from surface excitons to the overall emission becomes significant, while it is almost irrelevant in bulk materials.

More extensive information on ZnO optical properties can be found for example in refs. [67], [74], [76] and [78].

1.3 Growth techniques

Usually bulk zinc oxide crystals are grown by hydrothermal methods, seeded vapor phase (SVP) method or melt growth. ZnO films have been grown by several techniques (like sputtering, CVD and metal-organic CVD, PLD, MBE, vapor phase epitaxy) on a large number of different substrates (like glass, sapphire, diamond, silicon, GaAs, CaF_2). More details about the growth of bulk ZnO and films can be found for example in ref. [67].

As mentioned in the introduction, a wide number of zinc oxide nanostructures has been obtained, like e.g. dots [72], wires [96], rods [97], belts, combs, rings, springs, tubes,

cages [98], ribbons [99], needles [100], tetrapods [101], hierarchical structures [102], and so on. **Fig. 1.5** shows a collection of some ZnO nanostructures.

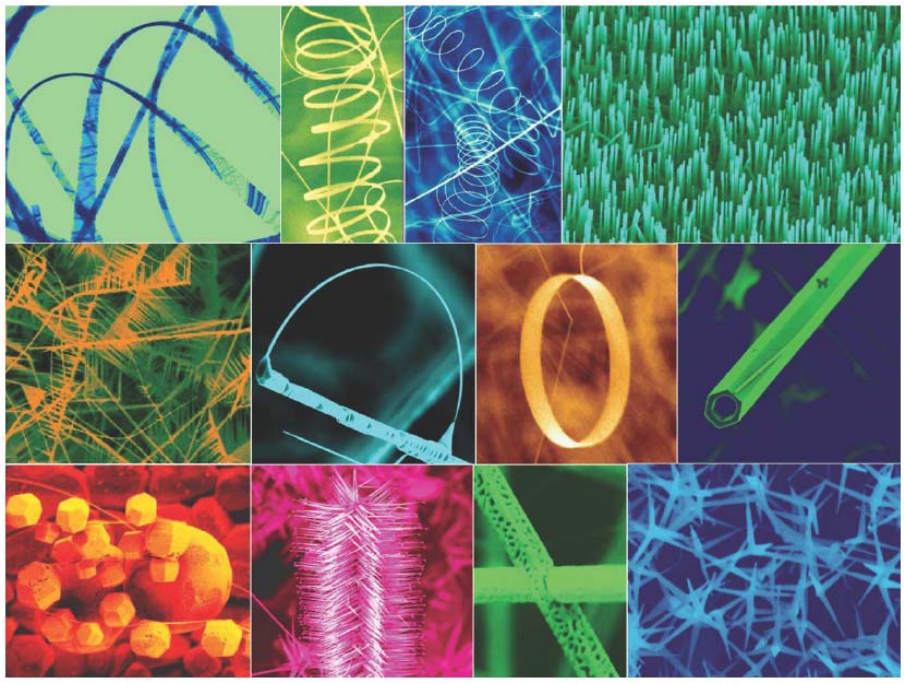

Fig. 1.5. Some zinc oxide nanostructures grown by thermal evaporation. (Image from ref. [98]).

Several growth techniques have been used to realize these ZnO nanostructures. Some of them are listed below.

- A typical extensively used technique is *thermal evaporation*. This vapor-phase method involves the evaporation of a source material, e.g. zinc or zinc oxide, in a furnace; the evaporated species are transported onto a substrate, maintained at the chosen temperature, through a flux of an inert gas or a mixture containing a gas which must interact with the evaporated species (for example oxygen if only zinc is evaporated); by properly tuning the growth parameters, the condensation of the gaseous species on the substrate leads to the growth of different nanostructures [98].

  Often, in order to get nanostructures, the growth must be aided by a catalyst. For example sometimes the catalyst is dispersed together with ZnO in the source

material (e.g. a mixture of graphite and ZnO powders [96]) and, during the condensation process, it catalyzes the nanostructure growth. In other cases a thin layer of a catalyst (e.g. Au, Cu, Ni, Sn, Pt, etc.) is previously deposited on the substrate. Usually the growth process in this technique is reported to be related to a vapor-liquid-solid (VLS) mechanism [96], that is: on the substrate the catalyst forms liquid droplets which promote the adsorption of the gaseous molecules; when supersaturation is reached, the nucleation and subsequent growth of nanometric structures start.

Usually, when no catalyst is used during the growth, a vapor-solid (VS) sublimation mechanism is proposed [98].

In order to aid the nanostructure formation or to modify their properties (like density on the substrate, dimensions, etc.), sometimes a ZnO film (*buffer layer*) is deposited on the substrate before the nanostructure deposition [103].

Thermal evaporation is a very simple technique, but it usually requires high temperatures (even ~ 900°C or more) in order to evaporate the source material or to form the liquid catalyst droplets on the substrate. Moreover sometimes reproducibility is not very easily obtainable.

In **Fig. 1.5** some ZnO nanostructures grown by thermal evaporation are presented.

- *Chemical Vapor Deposition* (*CVD*) [104] and *Metalorganic CVD* (*MOCVD*) [97, 100] are also widely used methods for growth of ZnO nanostructures. In this technique volatile precursors containing the elements of the material to be deposited are transported onto the heated substrate where they react or decompose allowing the growth of the material. As for thermal evaporation, even in this case catalysts are sometimes used, and VLS or VS (for catalyst-free CVD) mechanisms are proposed as possible growth processes.

  Also *plasma-enhanced CVD* (*PECVD*), in which a plasma is used in order to enhance chemical reaction rates of the precursors, has been employed to obtain ZnO nanostructures [105].

- Direct *oxidation* of zinc powders has been showed to allow the realization of ZnO nanostructures. For example ZnO tetrapods have been obtained by placing zinc powders in a furnace at 850-900°C in oxygen atmosphere [101].
- ZnO nanostructures have been synthesized by *hydrothermal methods* [106], which consist in the growth from hot (~ 90°-300°C) aqueous solutions at high vapor pressures (~ 1 atm or more). The aqueous solution contains the precursors for the growth of the material of interest, which dissolve in the high-temperature solution and condense in the cooler part of the chamber.
- Apart of hydrothermal synthesis, other *solution-based* methods have been used to synthesize ZnO nanostructures, like *electrochemical methods* (or *electrodeposition*) [107], *sol-gel methods* [72, 108], other solution-based chemical routes [109], *sonochemical* synthesis and *microwave-assisted* synthesis [110].
- ZnO nanostructure deposition can be obtained by *sputtering* [111] of a solid target through bombardment of highly energetic ions. Sometimes the plasma generated in the deposition chamber can be properly modified by the help of radio-frequency and magnetic fields (*RF magnetron sputtering*) [112].
- *Molecular Beam Epitaxy* (*MBE*) has been used to realize ZnO nanostructures. Even in growth by *MBE* a catalyst can be used to aid the nanostructure formation. For example the cation flux coming from a zinc source is oxidized in a plasma of ozone/oxygen mixture and the material deposits on a catalyst-coated (e.g. Ag) heated substrate [113].
- *Pulsed Laser Deposition* (*PLD*) is another very useful technique for ZnO nanostructure growth. Briefly, in this technique a high-power pulsed laser beam is focused onto a target material (for example metallic zinc or sintered/ceramic zinc oxide) placed in a vacuum chamber, causing the ablation (ejection) of the material which interacts with the background atmosphere (for example oxygen) and deposits on a substrate. Even in PLD, as in other techniques, a catalyst can be used to help the growth of nanostructures.

Various reports exist about ZnO nanorods/nanowires deposited by laser ablation (see e.g. [114, 115] and par. 2.1.b). ZnO quantum dots have been obtained by PLD and subsequent thermal annealing [116] and Co-doped ZnO nanoneedles have been realized by PLD [117].

Moreover different variants can be used instead of the conventional PLD technique, in order to get, for example, other morphologies of the deposited samples.

More details on the growth of ZnO nanostructures by PLD are reported in par. 2.1.

- Zinc oxide nanostructures can be realized by using *template-directed methods*, in which a periodic structured template (for example an anodic alumina membrane or a polymeric membrane) is exploited to lead the growth of the material. The pores of the template can be filled by using other techniques. For example nanodots have deposited by PLD using an anodic alumina membrane [118] and nanorods have been obtained by evaporation on a gold membrane [119].
- Finally, it must be added that different methods, other than the previous ones, have also been used to deposit ZnO nanostructures. Moreover, techniques made by combinations of different methods can be used: for example ZnO nanorods have been grown by chemical vapor deposition combined with pulsed laser deposition [120]. Another example of a mixed technique is a combination between laser ablation and chemical synthesis (see par. 2.1.a).

Chapter 2
Zinc oxide growth by Pulsed Laser Deposition

Chapter 2 - Overview

In this chapter the samples deposited during the research activity of this Ph.D. Thesis are presented.

The first paragraph, after a brief introduction on the PLD technique, shows some results presented in literature about the deposition of ZnO nanorod/nanowire arrays by PLD, providing an idea on the used deposition parameters and the proposed growth mechanisms presented in literature for such structures.

In the second paragraph the experimental PLD set-up and the deposition parameters used in this work are described.

The last paragraph shows the study of the morphology made in this work for the deposited samples. The possible growth mechanisms are proposed to explain the observed morphologies and some comparisons are made between the results obtained when the two different laser wavelengths (248 nm or 193 nm) were used for the target ablation.

2.1 Pulsed Laser Deposition of zinc oxide nanostructures in literature

2.1.a Introduction

As stated in par. 1.3, Pulsed Laser Deposition (PLD) is a technique used to deposit ZnO nanostructures. PLD is known to be a suitable technique to realize good quality ZnO films [121, 122] and, by properly tuning the deposition parameters, it has been also used to obtain nanostructures by employing either conventional or unconventional experimental set-ups. The schematization of a conventional PLD system is reported in **Fig. 2.1**: the laser beam is focused onto a target material inside the vacuum chamber, causing the ablation of the material. The ablation can be conducted in vacuum or in the presence of a background atmosphere of a particular gas. The ejected species continue absorbing energy from the laser and eventually interact with the background atmosphere, giving rise to a composite material (RPLD – Reactive Pulsed Laser Deposition). The generated plasma plume expands and the material deposits onto a substrate generally placed in front of the target (on-axis configuration). Usually the target holder is rotated and moved to avoid continuous ablation on the same point, and the substrate can be heated to the suitable temperature for the desired purpose and moved to gain a uniform thickness of the deposited sample.

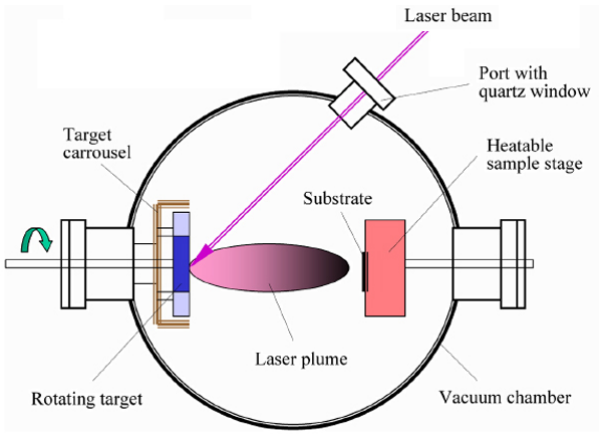

Fig. 2.1. Schematization of a conventional PLD system. (Image from http://superconductivity.et.anl.gov)

In unconventional PLD systems [123, 124], laser ablation and deposition take place in modified experimental set-ups, appearing for example as mixed systems between furnaces and laser ablation systems.

PLD is known to have some advantages over other deposition techniques. For example the stoichiometry of complex target materials can be easily preserved in the deposited sample, by suitably choosing the deposition parameters. More than one target can be placed and exchanged inside the chamber, thus allowing simple *in situ* deposition of multi-layers or doped materials. Moreover, due to the high kinetic energy of the ablated species, high sticking on the substrate and high mobility of the species on the substrate are allowed, therefore it is possible to obtain growth of nanostructures at lower deposition temperatures with respect to other techniques.

By using the classical PLD technique, ZnO nanostructures have been deposited by using different lasers as ablation sources, such as KrF [114] or ArF excimer lasers [115], frequency-quadrupled Nd:YAG laser [125], and femtosecond laser [126].

Also some variants of the classical PLD technique have been reported to deposit ZnO nanostructures. For example laser ablation of metallic zinc in aqueous solutions containing other surfactants has been reported for growth of ZnO nanostructures, such as nanoparticles [127], nanoleaves [128], nanorods and other nanostructures [129]. ZnO nanoparticles have been also obtained by laser ablation of a zinc oxide target in pure liquids, like deionized water and ethanol [130]. This technique can be considered as a mixed method between laser ablation and chemical synthesis.

Usually for the usual PLD technique, as for other deposition techniques, three modes of film nucleation and initial growth are reported (see e.g. ref. [131]): the *Frank-Van der Merwe* mechanism consists in a 2D layer-by-layer growth, occurring when the cohesive energy of the depositing species with the substrate is higher than the cohesive energy among the depositing species; the *Volmer-Weber* mechanism occurs when the cohesive energy of the depositing species with the substrate is lower than the cohesive energy among the depositing species, thus resulting in a 3D growth of isolated islands; the *Stranski-Krastanov* mechanism is a mixed mode between the previous ones, consisting in island formation after the growth of few 2D layers and occurring because of strain effects

due to lattice mismatch between the substrate and the growing film. The first mechanism results in the growth of a smooth epitaxial film, while the other two modes result in the growth of rough or polycrystalline films or nanostructures. However, as shown in the next paragraph, different mechanisms can be proposed for the growth of nanostructures.

2.1.b PLD of zinc oxide nanorod/nanowire arrays by excimer laser ablation

By focusing the attention on excimer laser ablation (since this kind of laser has been used in the research activity of this Ph.D. Thesis), it can be observed that several different parameters have been used in order to deposit ZnO nanorod/nanowire arrays. For example, depositions have been performed in high (> 100 Pa) or low (~ 1 Pa) oxygen background pressure, with or without the help of a catalyst, on different substrates (sapphire, silica or silicon), and with target-substrate distance ranging from 5 to 70 mm. In some cases, a ZnO film has been deposited as a buffer layer on the substrate before the subsequent growth of the nanostructures, or the substrate was placed in an off-axis configuration (parallel to the direction of propagation of the expanding plasma plume). Usually oxygen was used as background gas in order to preserve the ZnO stoichiometry, since oxide materials deposited in vacuum are generally lacking in oxygen (see e.g. [132]). In addition, sometimes high oxygen pressure was used to increase the stopping power and the number of scattering events of the ablated species, thus changing the properties of the deposited samples (see for example ref. [131] and the discussions presented below). Sometimes a different background gas, other than oxygen, was used during the depositions.

In **Tab. 2.1** a summary of the deposition parameters used by some research groups to grow ZnO nanorod/nanowire arrays is reported: the different groups are labeled with capital letters from *A* to *G*, and the subscripts indicate different references related to the same group; in the "Laser parameters" column, the mixture of the excimer laser (KrF [λ=248nm] or ArF [λ=193nm]), the laser fluence (energy per unit area) on the target and

Refs.		Laser parameters	Target	Substrate	$T_{substrate}$	Catalyst	Background Atmosphere	D_{T-S} (mm)	Deposition Time (min)	Proposed growth mechanism
A	A_1	KrF 3 J/cm² 20 Hz	Sintered ZnO	Sapphire (0001)	400-800°C [700°C]	/	O_2 133-1330Pa	20	30	nanoparticle-assisted (nanoparticles are formed in the plume and deposit onto the substrate, forming the nanorods)
	A_2						O_2 13.3-2700Pa He 400Pa	20-70		
	A_3		Sintered ZnO or metallic Zn	Sapphire (0001) or silica	700°C		O_2 13.3-2700Pa or He 13.3-2700Pa	20-50	/	
	A_4	KrF 3J/cm² 20 Hz	ZnO	Sapphire (0001) or (1120)	$T_{furnace}$ 1000°C	/	Ar 35000-66500Pa	/	/	/
B	B_1	ArF 6-10 J/cm² 10 Hz	Ceramic ZnO	Silicon (100)	300-750°C [600°C]	/	O_2 1.33Pa	40-60	15, 30, 45	VLS catalyzed by Zn droplets
	B_2			Silicon (100) or Silicon (100) with a ZnO buffer layer	300-750°C (buffer layer at 300°C)				45 (buffer layer 1 min)	VLS catalyzed by Zn droplets on bare Si. VS when the buffer layer is deposited.
	B_3	ArF 2-20J/cm², 10Hz		Silicon (100)	600°C			20,50	45	/
C		ArF, 10 Hz	ZnO	Sapphire (0001)	500°C	/	Ar 10Pa	/	60	VS nanoparticle-assisted (Stranski-Krastanov)
D		KrF	Sintered ZnO	Sapphire or Silicon (100)	550-780°C	/	O_2 33-2660Pa	20-42	/	/
E		KrF	ZnO	Silicon	150-800°C [500°C]	/	O_2 133-930Pa	25	2-20	nanoparticle-assisted
F		KrF 1-5 J/cm²	Sintered ZnO	Silicon	500-900°C	without or with Au (5-30Å)	O_2 26.6-1330Pa	/	/	VLS (atypical)
G	G_1	KrF, 2J/cm² 3-10 Hz	Sintered ZnO	Sapphire $(11\bar{2}0)$ or (0001) (off-axis)	870-950°C	Au (1nm)	Ar 2500-20000Pa	5-35	/	VLS (atypical)
	G_2	KrF, 10 Hz	Sintered ZnO	Sapphire $(10\bar{1}0)$ (off-axis)	690-900°C	/	O_2 and Ar (total pressure 5000-30000Pa)	25	/	/

Tab. 2.1. Deposition parameters used by different research groups to grow ZnO nanorod/nanowire arrays.

the repetition rate of the laser pulses are reported; $D_{T\text{-}S}$ is the target-to-substrate distance; in the last column the proposed growth mechanism is also summarized, if reported in the corresponding papers. Rows colored with light gray indicate references where unconventional PLD systems have been used. Some comments about the results obtained by the different groups and about the different proposed growth mechanisms are reported below.

A) T. Okada et al.

A_1) Refs. [114, 133]:

In an oxygen background pressure of 665 Pa and $T_{substrate}$=700°C the authors observed c-axis oriented hexagonal rods with mean diameter ~ 300 nm and lengths ~ 6 μm, while at lower temperatures they observed ball-like structures (at 400°C), hexagonal structures and particles (at 500°C) and hexagonal structures with diameters of 100-700 nm (at 600°C). A thin layer between the substrate and the rods was observed. By Rayleigh scattering the authors observed that nanoparticles were formed in the gas-phase and transported onto the substrate. On the base of this observation the authors assumed that these nanoparticles stacked on the substrate and, since their melting temperature is far lower than the bulk ZnO melting temperature, they fused forming the nanorods. Moreover they supposed that formation of nanorods is possible at high background pressures (from ~ 100 Pa) since at these pressures nanoparticles can be formed in the gas gas-phase.

A_2) Refs. [134, 135]:

At $T_{substrate}$=700°C and $D_{T\text{-}S}$=30mm the authors observed the growth of rods when the oxygen background pressures was in the range ~ 100-600 Pa. At lower pressure (~ 13.3 Pa) micro-crystals (~ 1-2 μm) on a smooth film were grown while at higher pressure (> 1330 Pa) the rods fused together and the surface became flattened. Increasing $D_{T\text{-}S}$ the rod diameter and length decreased. By using helium background atmosphere (~ 400 Pa) instead of oxygen, no rods were observed, while only hexagonal micro-crystals were obtained on a smooth film.

A_3) Refs. [136]:

In oxygen background pressure the same structures described in the previous references were observed. On sapphire substrate at 700°C by increasing the helium background atmosphere the deposited samples passed from a smooth film (at ~ 13.3 Pa), to hexagonal micro-crystals (at ~ 133-665 Pa), to a meshlike structure (at > 1330 Pa). When a metallic zinc target was ablated, the rods on sapphire were similar to those grown from a ZnO target, while on silica substrate the rods were bigger (diameter ~ 1 μm) and somewhat tilted from the substrate normal.

A_4) Ref. [137]:

Here the authors used a modified PLD system, consisting of a quartz furnace where a ZnO target was ablated. In this way the laser ablation occurred in a high-temperature gas background. Moreover the depositions were performed at very high background pressures and with different substrate positions. In argon atmosphere of 36000 Pa and at a furnace temperature of 1000°C, on sapphire (0001) a web-like structure of nanowires with diameters ~ 50 nm together with some large crystals (~ 200 nm) or bigger wires (~ 500 nm) with smaller wires (< 100 nm) on their top were deposited for different positions of the substrate. On sapphire (1120) cone-shaped crystals perpendicular to the substrate surface were obtained.

B) Y. Sun, M.N.R. Ashfold et al.

B_1) Ref. [115]:

At $T_{substrate}$=600°C the authors observed the growth of rods (base diameter ~ 60 nm, length ~ 200-800 nm) on a thin ZnO layer; at lower temperatures polycrystalline films or with a network-like morphology were grown, and at higher temperatures irregularly shaped larger particles were observed. On the tip of the rods ZnO capping particles were present: on the base of this observation the authors supposed that the growth followed a VLS mechanism, catalyzed by Zn liquid droplets where adsorption of oxygen took place.

B_2) Ref. [138]:

A thin ZnO layer was grown at 300°C for 1 minute before increasing the substrate temperature to 600°C for the growth of the nanorods. With respect to nanorods grown

without this layer, nanorods on pre-coated substrate were denser, thinner (base diameter ~ 20 nm) and longer (~ 1-1.2 μm). Moreover in this case no capping particles were observed, thus suggesting to the authors that the growth occurred by a VS mechanism, with rods starting to grow from nucleation sites which were nanosized crystallites on the ZnO layer.

B_2) Ref. [139]:

The authors observed a decreasing of the rod diameters from ~ 100 nm to ~ 10 nm with decreasing the laser fluence, and they ascribed this behavior to a higher bombardment effect of high energy species in the plume at higher fluences thus allowing only the bigger rods to survive.

C) S. Choopun et al. [140]:

In argon atmosphere the authors obtained rods with diameter ~ 500-700 nm at higher fluences* and ~ 40-100 nm at lower fluences, while only 3D hexagonal islands where observed in oxygen atmosphere. They explained this behavior observing that the mean free path of the particles in the plume was shorter in argon atmosphere than in oxygen, thus allowing more scattering events and the consequent formation of nanoparticles and zinc sub-oxide species in the gas phase; these nanoparticles started the growth on the substrate and then acted as nucleation sites for the growth of the rods; therefore the authors supposed a Stranski-Krastanov growth mode allowed by the formation of nanoparticles in argon atmosphere.

D) Z.W. Liu et al. [141]:

On sapphire substrate at 700°C, rods with a mean diameter of ~ 400 nm were obtained at oxygen background atmosphere of 1330 Pa, while increasing the oxygen pressure the rods started to contact each other forming a continuous film. Also at pressure lower than 665 Pa a continuous film was deposited. At oxygen pressure of 1330 Pa and sapphire temperature of 600-700°C, the authors observed the growth of rods, while

* The fluence values were not reported in the paper; only the laser energy (75-125 mJ) was reported.

hexagonal crystals were obtained at 550°C (~ 120 nm) and continuous films were deposited at temperatures lower than 500°C or higher than 750°C. On silicon substrate at 600°C in 1330 Pa of oxygen, rods with a mean diameter of ~ 400 nm were observed.

E) V. Gupta et al. [142, 143]:

In oxygen atmosphere of 665 Pa the authors observed the growth of rough and porous polycrystalline film at low substrate temperature (< 450°C), rods with a low size dispersion (~ 120-200 nm) at ~ 500°C, rods with high size dispersion (~ 70-350 nm) at ~ 600°C and a film having densely packed large size grains at ~ 800°C. Again the growth mechanism was believed to be related to the nucleation of the nanoparticles formed during the scattering events in the high background pressure.

F) J.-H. Park et al. [124]:

Like in ref. A_4 , the unconventional PLD system here used was a furnace where the ablation of the target was performed. Here the authors deposited ZnO rods either without or with a 5-30 Å layer of Au catalyst. Without the catalyst, rods with diameters ~ 200-600 nm were deposited in the temperature range of 800-900°C with a fluence of ~ 3-5 J/cm^2, while at lower temperatures a wrinkled patterns (600-800°C) or rough or grain-shaped films (500-600°C) were observed. With the catalyst, thinner rods (30-100 nm) were deposited with a fluence of ~ 2-5 J/cm^2 in the temperature range of 700-900°C, and again wrinkled patterns or rough films were obtained at lower temperatures. When the Au catalyst was used the authors supposed a VLS growth mechanism but, since no Au presence was revealed on the rod tips, they retained that the catalyst had an important role only during the initial growth of the rods, thus remaining at their bottom.

G) M. Lorenz, M. Grundmann et al.

G_1) Ref. [123]:

The unconventional PLD system used was a T-shaped quartz furnace in which the laser ablation was performed. The authors obtained the growth of rods or needles only in

the regions of the substrate covered by the Au catalyst, while only a wetting layer was observed on the uncoated regions. No Au particles were detected on the top of the rods, while gold nanodrops were identified near the ZnO wetting layer, so the authors supposed that gold had an important role only in the nucleation steps of the rods.

G_2) Ref. [144]:

The used PLD system is the same as in G_1. By depositing on sapphire $(10\bar{1}0)$ substrates, the authors found that the grown rods were 30°-inclined to the right or to the left with respect to the substrate normal. By increasing the furnace temperature, the mean rod dimensions (both diameter and length) increased. By decreasing the total pressure in the tube under 10000 Pa, the rods began to coalesce, while, fixed the total pressure at 10000 Pa, the authors observed an increase of the lateral rod dimensions with increasing the oxygen partial pressure.

In **Fig. 2.2** some examples of nanorods grown by PLD by different groups are reported.

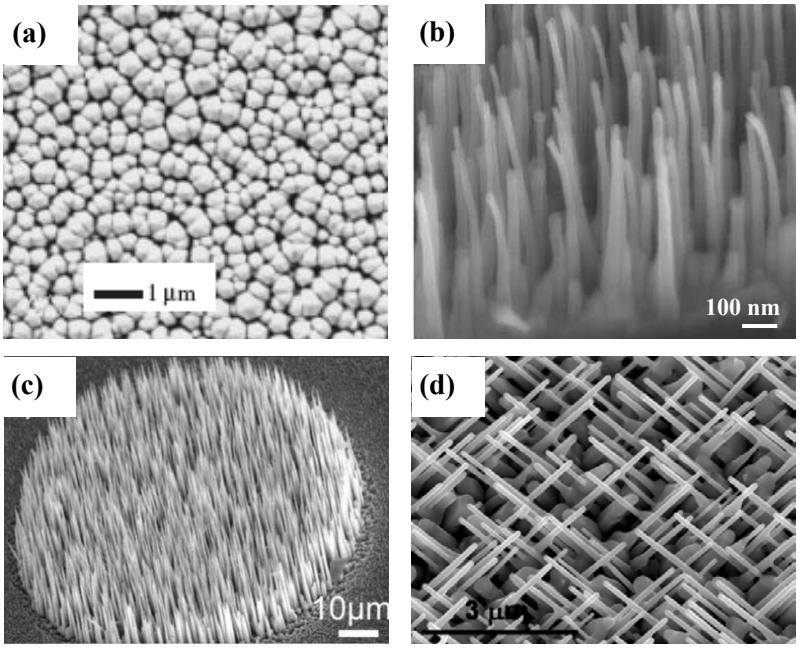

Fig. 2.2. Some examples of nanorods grown by PLD. **(a)** from ref. [114], **(b)** from ref. [115], **(c)** from ref. [123], **(d)** from ref. [144].

As seen in the discussion above, different mechanisms have been proposed to explain the growth of ZnO nanorods: formation of nanoparticles in the plume which form nucleation sites on the substrate for the nanorod growth (for example in a Stranski-Krastanov mode), VLS catalyzed by zinc droplets or VS on a ZnO buffer layer, atypical VLS with the Au catalyst on the bottom of the rods instead of the top as in classical VLS. It should be noticed that formation of nanoclusters in the gas phase during ablation of ZnO has been also demonstrated by photoluminescence measurements [145].

Moreover, it is evident that several different sets of deposition parameters have been used to successfully grow ZnO nanostructures. This implies that obviously it is not possible to choose a unique set of parameters to obtain nanostructure growth and that the right set of deposition parameters must be found and optimized on one's own experimental system.

2.2 Experimental set-up and deposition parameters

2.2.a Experimental set-up

The experimental set-up used during the research activity described in this Thesis was a conventional PLD system, similar to that one schematized in **Fig. 2.1**.

The excimer laser used for the target ablation was a Lambda-Physik LPX 305 I, with the possibility to change the working gas mixture (KrF or ArF) and thus the corresponding output wavelength: 248 nm (~ 5 eV) for KrF, 193 nm (~ 6.4 eV) for ArF. The laser pulse duration was ~ 25 ns. The laser beam was shaped through a mask with a 1cm×1cm aperture in order to select the most uniform region of the beam. The beam was focused onto the target by a f = 30 cm lens. The target was placed in a stainless steel vacuum chamber evacuated by a pumping system constituted of a scroll pump and a turbomolecular pump; the pressure was monitored by two capacitive vacuum gauges

(Leybold Inficon CR1000 and CR090) operating from atmospheric pressure to ~ 1 Pa, and a ionization gauge (Leybold ITR100 IONIVAC) operating in the range from ~ 10 Pa to ~ 2×10^{-8} Pa. In order to detect possible contaminants in the residual atmosphere, a mass spectrometer (Leybold Inficon Transpector 2) with a range of 1÷100 amu was used before starting each deposition. The vacuum chamber was provided with micrometric valves for gas input; for this research activity, oxygen gas with 99.999% purity was used. The target was put on a target-holder rotated and translated to avoid continuous ablation on the same point. The substrate was placed on a substrate holder/heater which could be moved in order to get uniform thickness of the deposited sample; however, for the depositions performed in this research activity, no substrate movement was used due to the small deposited areas (1cm×1cm). The substrate heater was a home-made lamp heater, designed and realized during the research activity of this Thesis, allowing to set the substrate temperature up to ~ 700°C. A K-type thermocouple was fixed on the front face of the substrate holder, nearly in direct contact with the substrate (distance ~ 1 mm) in order to measure the actual substrate temperature, and protected against the incoming ablated material; moreover the thermalization of the heater surface was obtained awaiting about one hour after the desired temperature was reached, before starting the target ablation. The value of the laser fluence on the target was obtained by measuring, before evacuating the vacuum chamber, the laser energy arriving onto the target by a joulemeter (Gentec ED-500) and the area of the laser spot directly on the target surface by a caliper.

In **Fig. 2.3** a photo of a detail showing the target and the substrate on the heater is reported. The plasma plume in the photo was produced by the ablation of the ZnO target by the KrF excimer laser in 1 Pa of oxygen background pressure. In the image the thermocouple can be noticed: it comes from the upper side of the heater/holder and it goes down, shielded and tightly pressed on the heater by a stainless steel sheet, arriving almost in direct contact with the substrate.

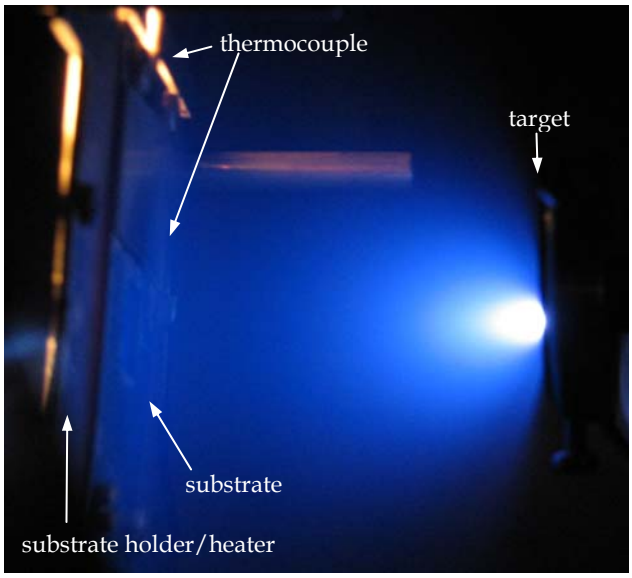

Fig. 2.3. A detail inside the vacuum chamber showing the ZnO plume produced by the KrF laser beam in 1 Pa of oxygen background gas; some elements of the set-up are visible.

2.2.b Deposition parameters

As reported in par. 2.1.b, different sets of deposition parameters have been used in literature to grow ZnO nanowire/nanorod arrays by excimer laser ablation. Anyway, by a comparison of the parameters used by the different research groups (see par. 2.1.b and **Tab. 2.1**), it is possible to draw some observations:

- by KrF (λ = 248 nm) laser ablation, fluences from ~ 1 to 5 J/cm^2 have been used, while by ArF (λ = 193 nm) laser ablation a study (group *B* in **Tab. 2.1**) by varying the fluence from ~ 2 up to 20 J/cm^2 has been reported;
- usually a zinc oxide target has been ablated for the depositions, although reports by using a metallic zinc target exist;
- the possibility to deposit these structures on different substrates (silicon, sapphire, silica) has been showed;

- the optimal substrate temperature was around 600°C, and, in all the reported literature sources, no nanorod/nanowire growth has been observed for substrate temperatures under 500°C;
- the help of a pre-deposited catalyst on the substrate was not essential to allow the growth of these structures;
- papers showing nanorod growth in both low (~ 1 Pa) or high (~ 100 Pa or more) oxygen background pressure have been reported; moreover some reports with the use of Ar background atmosphere have been presented;
- target-to-substrate distances from ~ 20 to 60 mm have been used, although also shorter or longer distances have been reported.

For the research activity of this Ph.D. Thesis, a study of catalyst-free depositions by using two different excimer laser wavelengths (KrF mixture and ArF mixture) for the target ablation, by varying the substrate temperature and by performing the depositions at low and relatively high oxygen background pressure has been conducted, while all the other deposition parameters have been kept constant. On the base of the observations above and of the results reported in literature (par. 2.1.b), the deposition parameters adopted for this research activity can be summarized here:

Fixed parameters

- Target = sintered ZnO target (99.999% purity, bought from M.C.S.E.)
- Repetition rate of the laser pulses = 10 Hz
- Laser spot dimensions on the target: ~ 4.2 mm^2 with KrF, ~ 4.5 mm^2 with ArF
- Laser fluence on the target: ~ 4.3 J/cm^2 with KrF, ~ 1.6 J/cm^2 with ArF
- Substrate = Si (100)
- Target-to-substrate distance = 45 mm
- Number of pulses for each deposition = 25000
- No catalyst used

Varied parameters

- Laser wavelength = 248 nm (KrF), 193 nm (ArF)
- Substrate temperature = 500-700°C
- Oxygen background pressure = 1, 5, 50, 100 Pa

It should be noticed that the low fluence value used for the ArF depositions, in comparison with values reported in literature, has been dictated by limitations in the experimental set-up: indeed the output energy obtained with the ArF mixture was lower than that one obtained with KrF, and the spot has been chosen in order to get the minimum spot dimensions obtainable having a regular (rectangular) shape and without evident non-homogeneous zones in the ablated region. In these conditions the minimum spot dimension was around 4.5 mm^2, resulting in a fluence of about 1.6 J/cm^2.

Before the deposition the silicon substrate was cleaned by ultrasonic baths of 10 minutes in acetone and 10 minutes in isopropyl alcohol.

The vacuum chamber was evacuated to a base pressure of ~ 4×10^{-5} Pa, which rose up to ~ 4×10^{-4} Pa when the substrate was heated, due to desorption inside the vacuum chamber.

Before starting each deposition, the substrate was shut by a steel mask and a preliminary ablation was performed spanning the target surface for two cycles. This preliminary ablation had to purposes. First, the target surface was cleaned of possible environmental contaminants. Second, it has been reported [132] that the target surface was Zn-enriched after just a few laser shots, due to backscattered zinc from the plume onto the target surface; therefore a preliminary target ablation ensured that the composition of the ablated species and the deposition rate were almost constant throughout the deposition [122].

After the film deposition, the substrate cooled down to room temperature with a rate of about 14°C/min at the same oxygen pressure used during the deposition.

In order to simplify the discussion about the deposited samples, **Tab. 2.2** reports the notation used to label each sample: the first letter (*K* or *A*) refers to the laser wavelength used for the target ablation (*K* for KrF, *A* for ArF), then the substrate temperature and the background oxygen pressure are reported in the label.

Sample name	Laser mixture	Substrate temperature (°C)	O_2 background pressure (Pa)
K500_1	KrF	500	1
K600_1	KrF	600	1
K700_1	KrF	700	1
K600_5	KrF	600	5
K600_50	KrF	600	50
K600_100	KrF	600	100
A500_1	ArF	500	1
A550_1	ArF	550	1
A600_1	ArF	600	1
A600_50	ArF	600	50
A600_100	ArF	600	100

Tab. 2.2. Sample labeling according to the used deposition parameters.

2.3 Morphology of the deposited samples

The morphology of the deposited samples was investigated by Scanning Electron Microscopy. A JEM JEOL 6500F instrument equipped with a Schottky Field Emission Gun (SEM-FEG) was used in the secondary electron detection mode. The nominal image resolution of the instrument is 1.5 nm at 15 kV and 5 nm at 1 kV. The observations were performed by setting the following experimental parameters:

- accelerating voltage: 5 kV. This allowed to observe the topographic details with a suitable resolution (nominally not worse than 5 nm) and with a good signal to noise ratio
- working distance: 10 mm. This value allowed to obtain a good compromise between field of view, depth of field and resolution.
- objective lens aperture: 30 µm. This was the smallest aperture, guaranteeing the highest achievable resolution

- probe current: 20 pA. This value was compatible with the high resolution operation mode and due to the high brightness of the electron source allowed to obtain a good signal from the sample.

The microscope is located at the Institute for Microelectronics and Microsystems of the National Research Council (IMM-CNR) – Department of Lecce.

2.3.a KrF-deposited samples (λ = 248 nm, E = 5 eV)

Fig. 2.4 reports the SEM images of three samples deposited at substrate temperatures of 500°C, 600°C and 700°C in 1 Pa of oxygen background atmosphere.

The sample deposited at 500°C (**Fig. 2.4(a)**) appears as a smooth film with a "jigsaw"-like morphology. This morphology is similar to that one reported for metal films grown by physical vapor deposition techniques in a growth regime of transition from islands to percolation [146]. It has been reported that metal films deposited by this kind of techniques on substrates such as silicon, glass or graphite, in certain ranges of temperature have an initial growth consisting in droplets forming small islands which touch and coalesce to create larger islands; when the growth proceeds these islands may further coalesce forming elongated structures with gaps between the different structures (this process is called percolation). The coalescence stops when the islands reach a certain critical size, and the resulting film morphology depends on the competition between island coalescence due to surface diffusion and island growth due to deposition. Of course some differences may be observed in sample K500_1 with respect to the metal films mentioned above: it can be observed that the "pieces" forming the jigsaw morphology are smaller (sizes of the order of ~ 10-100 nm) than the ones observed in metal films (more than 1 μm); moreover no gaps among them are observed. These observations suggest that zinc and zinc sub-oxide (Zn_xO_y with $y<x$) species, created in high amount in the plasma plume [147], form small droplets on the substrate since their melting temperature is very low (about 419°C [148] like the zinc melting point); these

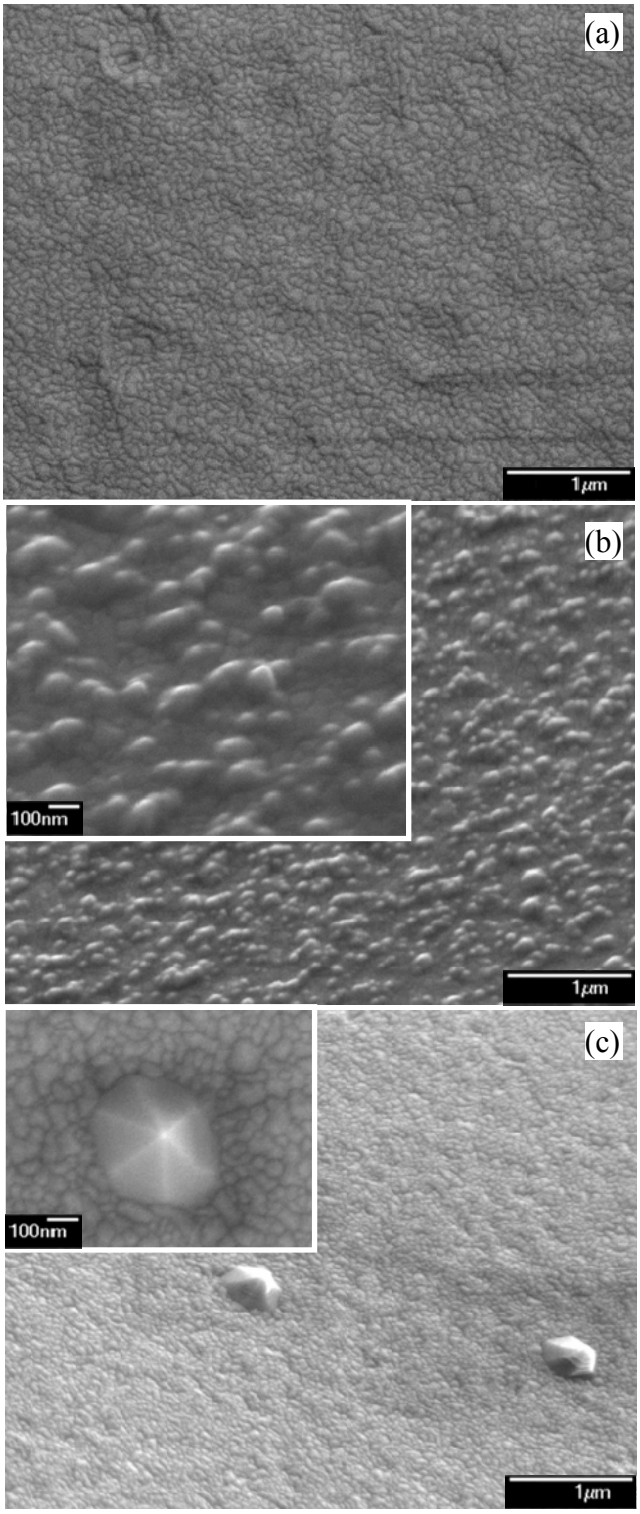

Fig. 2.4. SEM images of KrF-deposited ZnO films in 1 Pa of oxygen at substrate temperature of **(a)** 500°C, **(b)** 600°C and **(c)** 700°C. Image (b) and main panel of (c) are 45°–tilted views. Insets of (b) and (c) are at higher magnifications with respect to the corresponding main panels.

droplets coalesce in the very early stages of the growth and form the islands acting as nucleation sites for the subsequent film growth. As a consequence the final morphology resembles these islands formed in the early stage of the growth.

At substrate temperature of 600°C the same jigsaw-morphology is still present (see inset of **Fig. 2.4(b)**), but some structures, with dimensions ranging from few tens of nm to ~ 100 nm, emerge from the surface. This behavior is compatible with observations in literature reporting that the depositing species need higher energies to allow the growth of nanostructured samples; this energy is provided by the higher substrate temperature. In addition, for ablation of oxide materials in oxygen background atmosphere, it has been recently reported [149] that the substrate heating also influences the plume propagation: at higher temperatures the background gas resistance to plume propagation is reduced, leading to an increased velocity, and hence kinetic energy, of the species impacting the substrate during film growth. As a consequence, at higher substrate temperature these two reasons contribute to provide higher energy to the depositing species.

When the substrate temperature is further increased to 700°C, again the same jigsaw morphology is observed, but some sparse pyramids, with a nearly perfect hexagonal base of ~ 400 nm, are present (**Fig. 2.4(c)** and inset). By carefully observing these structures it seems they are not grown on the sample surface, while they seem to emerge from the bottom of the sample; it is reasonable that hexagonal columns starts directly from the substrate surface or just after some few layers of material, and that the observed hexagonal pyramids are their tops, like a sort of pencils with a diameter of ~ 400 nm. It can be thought that in the early stage of the growth some bigger clusters are formed due to coalescence of the depositing species and, due the high substrate temperature, as previously stated, these bigger clusters receive enough energy to be arranged in nearly perfect hexagonal crystals, resembling the ZnO wurtzite structure. As a consequence, it can be reasonably thought that the observed structures are grown along the ZnO wurtzite c-axis, perpendicular to the substrate surface.

Fig. 2.5 shows the SEM images of three samples deposited by setting the substrate temperature to 600°C and increasing the oxygen background pressure to 5, 50 and 100 Pa.

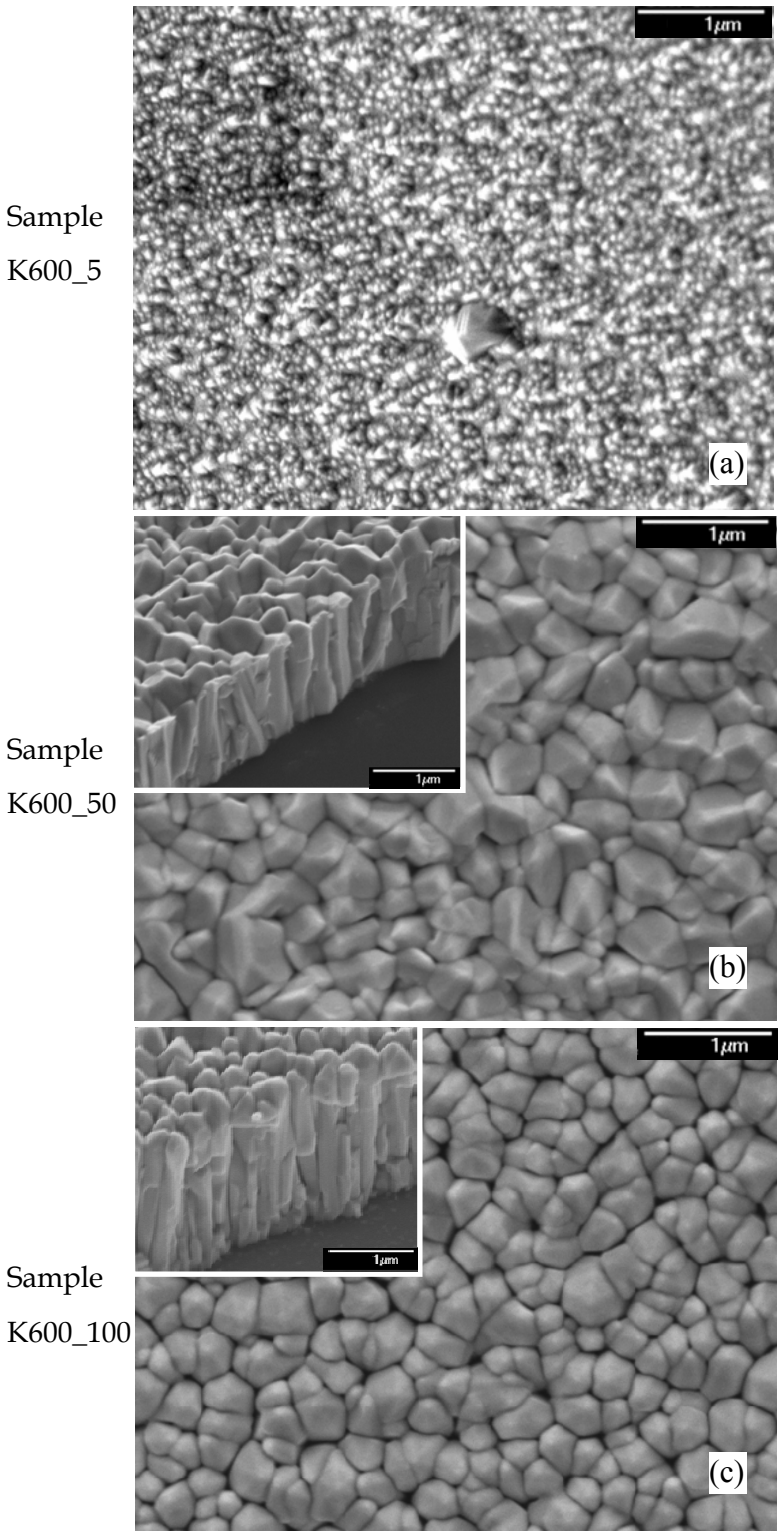

Fig. 2.5. SEM images of KrF-deposited ZnO films at substrate temperature of 600°C at oxygen background pressures of **(a)** 5 Pa, **(b)** 50 Pa and **(c)** 100 Pa. Image (a) is a 45°-tilted view. Insets of (b) and (c) are 40°-tilted view in proximity of intentionally-made scratches on the sample surface.

Comparing the morphology of the sample deposited at 600°C in 5 Pa of oxygen (**Fig. 2.5(a)**) with that one deposited in 1 Pa (**Fig. 2.4(b)**) it can been observed that the surface of the sample K600_5 is rougher than the sample K600_1 as expected due to the higher presence of particulates in a higher background pressure.

By further increasing the oxygen pressure to 50 Pa (**Fig. 2.5(b)**), the film shows a columnar structure with big grains with a wide dispersion in their dimensions. The columnar structure is evident from the 40°-tilted view got on a scratch intentionally made on the film surface (see inset in **Fig. 2.5(b)**). Moreover from the same image it appears there is no layer grown between the silicon substrate and the columnar film, unlike observed in some reports of literature. Therefore it seems that the columnar growth started directly from the substrate surface.

When the oxygen pressure is set to 100 Pa (**Fig. 2.5(c)**), the columnar growth is further marked and the well-distinguishable columns have a better uniformity in dimensions with respect to sample K600_50. The sample appears as a rod-array and, from the SEM images, it can be observed that the tops of the rods have a nearly hexagonal shape; in the top-view (main panel of **Fig. 2.5(c)**) this hexagonal shape is very evident for most of the columns. This observation, as made for sample K700_1, suggests that the columns grew along the c-axis of the ZnO wurtzite crystal structure. The morphology of sample K600_100 is very similar to that one reported in literature for depositions in high oxygen pressure (see groups *A* and *E* in par. 2.1.b and e.g. **Fig. 2.2(a)**). Moreover, as observed in those references, here can be noticed also the same behavior (attributed to the nanorod growth assisted by nanoparticle formation at high pressures) showing no growth of nanorod-arrays at oxygen pressure lower than ~ 100 Pa. The columns of this sample have diameters in the range ~ 100-400 nm and again, as already observed for sample K600_50, they seem to start directly from the substrate, without any layer grown between; this feature can be clearly observed by cross-sectional SEM images taken at higher magnifications (**Fig. 2.6**): the cross-sections were obtained by cutting the sample in a way to obtain a section approximately crossing the middle of the sample. Note that the bright line visible at the substrate-film interface on the right side of **Fig. 2.6(b)** is only due to an

edge effect of the silicon substrate in the region where a small portion of the column-array fell down during the cutting of the sample.

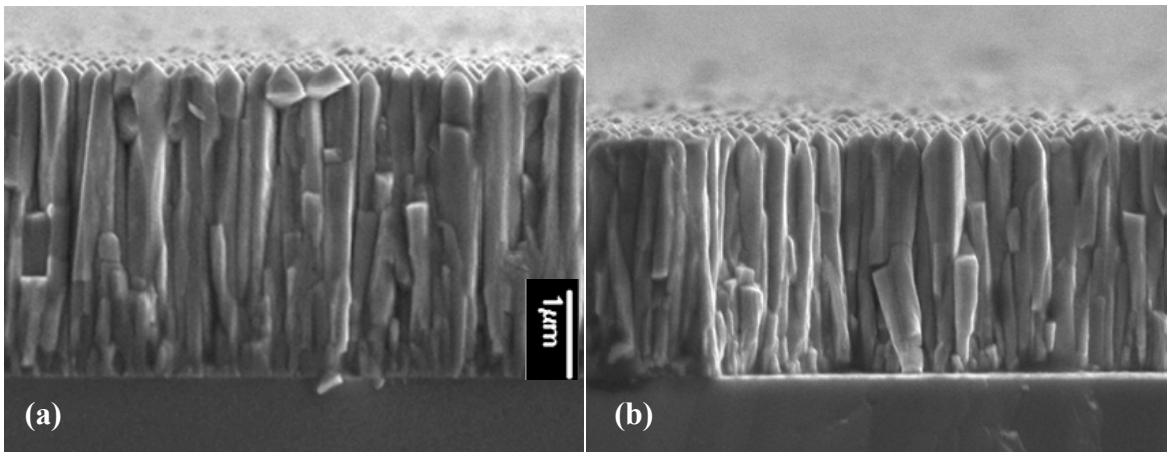

Fig. 2.6. SEM cross-section views of sample K600_100 near the center **(a)** and near the border **(b)**.

From these cross-sectional images it is possible to get an average thickness value of the film or, in other words, the average height of the rods; **Fig. 2.6(a)** is taken approximately at the center of the sample, while **Fig. 2.6(b)** is relative to a region far from the center, approaching the sample border: it can be measured that the column height near the center of the sample is about 3.5 μm while the sample thickness decreases to about 2.7 μm in proximity of the border. This non-uniformity of the thickness is attributable to the absence of substrate movement during the depositions, thus leading to a decreasing thickness when going away from the axis of propagation of the plasma plume. Another interesting feature can be observed in **Fig. 2.7**, where a comparison is shown among three images taken near the center and on the two opposite extreme regions of the sample: these images, taken at lower magnifications than the previous ones in order to better observe this feature, show that at the center of the sample the columns are well oriented perpendicularly to the substrate surface, while, going to the sample borders, they tend to slightly tilt toward the center. Supposing that the substrate is well centered with the axis of the plasma plume, this observation suggests that, although the columns grew along the wurtzite c-axis, their orientation is mainly affected by the axis of

the plume of the incoming material, while it is less influenced by the mismatch with the silicon substrate.

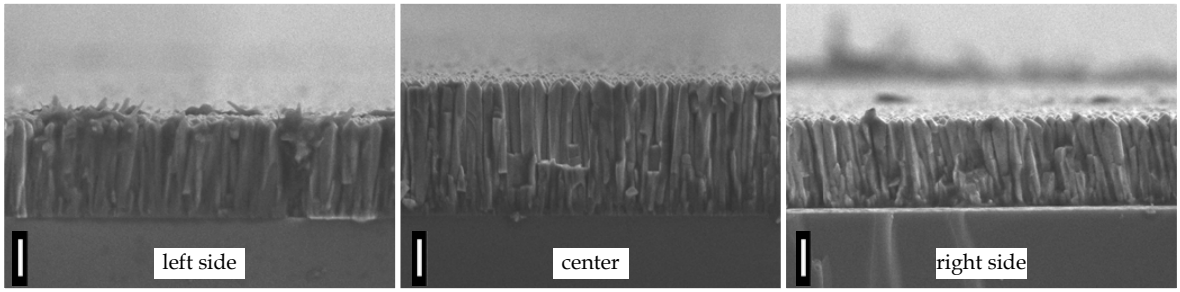

Fig. 2.7. SEM cross-section views near the extreme opposite borders and near the center of sample K600_100. The white markers are 1 μm.

2.3.b ArF-deposited samples (λ = 193 nm, E = 6.42 eV)

Fig. 2.8 shows the SEM images of three samples deposited by ablating the target with the ArF laser beam at substrate temperatures of 500°C, 550°C and 600°C in 1 Pa of oxygen background atmosphere. For all the three samples, nanostructures constituted by hexagonal terraces ("hexagonal hierarchical nanostructures") are visible; these structures are particularly evident in the inset of **Fig. 2.8(b)** and in **Fig. 2.8(c)**. It can be noticed that the nanostructure diameter increases with increasing the growth temperature; in sample A600_1 these structures have a base diameter of ~ 200 nm and a tip of ~ 30-40 nm.

Observing a higher magnification of sample A600_1 (**Fig. 2.9(a)**) the perfect hexagonal base and the hexagonal terraces can be clearly seen, thus suggesting, like other samples shown above, that the structures grew in the wurtzite structure with the c-axis perpendicular to the substrate; moreover it can be seen that these hierarchical structures sprout from a jigsaw-like film (see also the tilted-view in **Fig. 2.9(b)**) similar to that one observed for the KrF-deposited samples, thus suggesting a similar growth mechanism for both the ablating wavelengths.

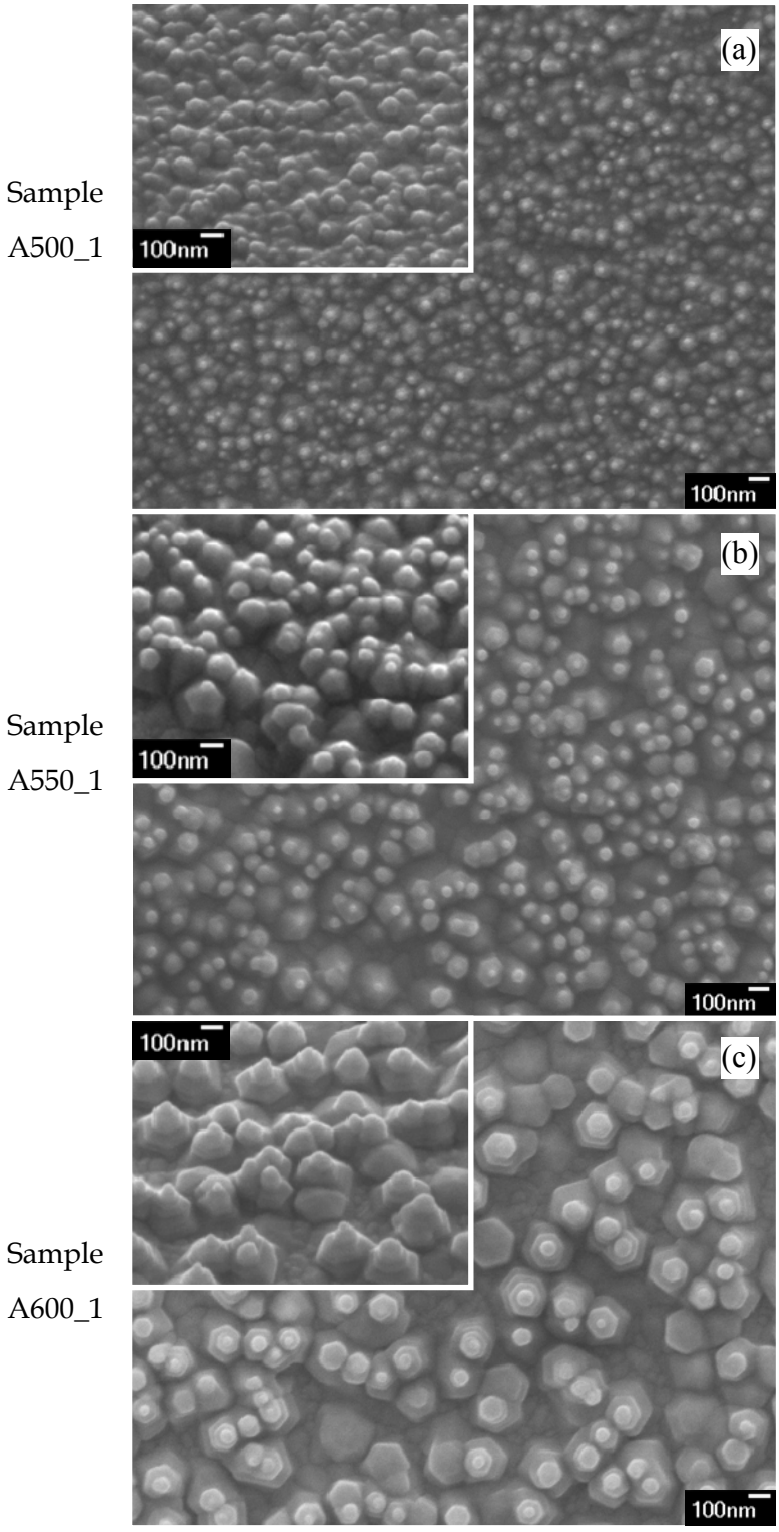

Fig. 2.8. SEM images of ArF-deposited ZnO films in 1 Pa of oxygen at substrate temperature of **(a)** 500°C, **(b)** 550°C and **(c)** 600°C. Insets of (a), (b) and (c) are 40°, 30° and 45° -tilted views, respectively.

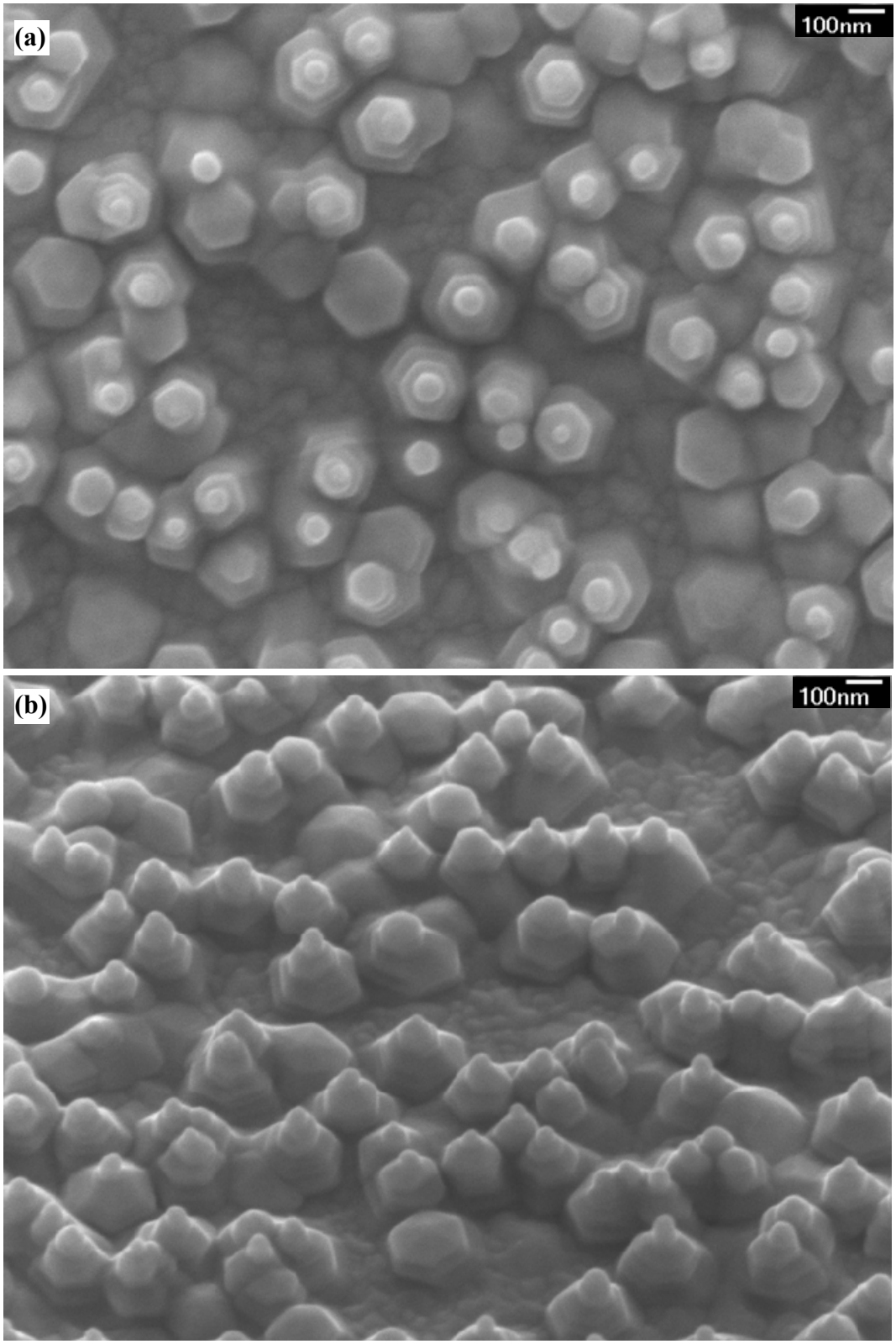

Fig. 2.9. SEM images of sample A600_1: **(a)** top-view; **(b)** 45°-tilted view.

As suggested for the KrF-grown samples, the possible growth mechanism can be presumed supposing that the species arriving onto the substrate coalesce forming the islands acting as nucleation sites for the subsequent film growth. But, since the ArF photon energy is higher than the KrF one (6.42 eV versus 5 eV), during depositions with ArF the target material is ablated by higher-energy photons and, in addition, the ablated species absorb higher-energy photons from the subsequent laser pulses. Additionally it should be observed that the zinc oxide absorption coefficient is higher at 6.42 eV than it is at 5 eV, thus the lower ArF laser fluence can be partially balanced by a higher absorption of the ArF laser beam per unit volume of the ZnO target, with respect to KrF. In a further addition, the higher energy of the ArF photons can also cause the production of more ionized species and more electronically excited species (Rydberg atoms or ions) in the ablated material; this feature can lead to a higher Coulombic repulsion and thus probably to higher plume velocities (at least for the charged components). As a consequence of all these factors, it may be supposed that during the depositions with the ArF beam, despite the lower laser fluence and the lower substrate temperature, the species depositing onto the substrate have a higher energy with respect to KrF; therefore it is possible to form bigger clusters having enough energy to arrange in hexagonal wurtzite crystals. Besides, it can be also underlined that the higher degree of plume ionization and a better dissociation of the oxygen molecules (as better explained in par. 3.2.c) lead to a greater reactivity between the ablated species and the background atmosphere, therefore the depositing species can be also different when the ArF or KrF lasers are used to ablate the target. All the features discussed above are possible reasons explaining the formation of nanostructures when the ArF wavelength is used, in comparison with the presence of only few structures when KrF is used.

About the terrace growth observed for the hierarchical structures, a possible explanation can be found in the competition between two processes, suggested to explain the growth of some hierarchical structures by vapor phase technique: *ledge-flow mode* and *nucleation on the terrace* [150]. When a terrace is formed, the other incoming species can diffuse from the terrace to its edge (ledge-flow mode) or can coalesce starting to form a new terrace (nucleation on the terrace); the competition between this two processes

depends on the ratio of the diffusion time of an adatom from the terrace to the edge and the interval time between adatoms arriving at the terrace. This mechanism may also explain the increasing nanostructure size with the substrate temperature observed in **Fig. 2.8**: indeed increasing the substrate temperature the surface mobility of the depositing species increases, thus increasing the rate of the diffusion process of adatoms to the edge of the ledge and consequently increasing the nanostructure diameter.

An interesting feature is the observation of a behavior similar to what noticed for sample K600_100: going near the border of the sample, the structures tend to be slightly tilted toward the center of the sample. This is evident in **Fig. 2.10** where a portion of the sample near the border is explored: the structures are clearly inclined toward the center of the sample and in addition, taking a higher magnification in the extreme border (**Fig. 2.10(b)**), it can be seen that the structures partially lose the well-defined hierarchical structure observed in the center of the sample.

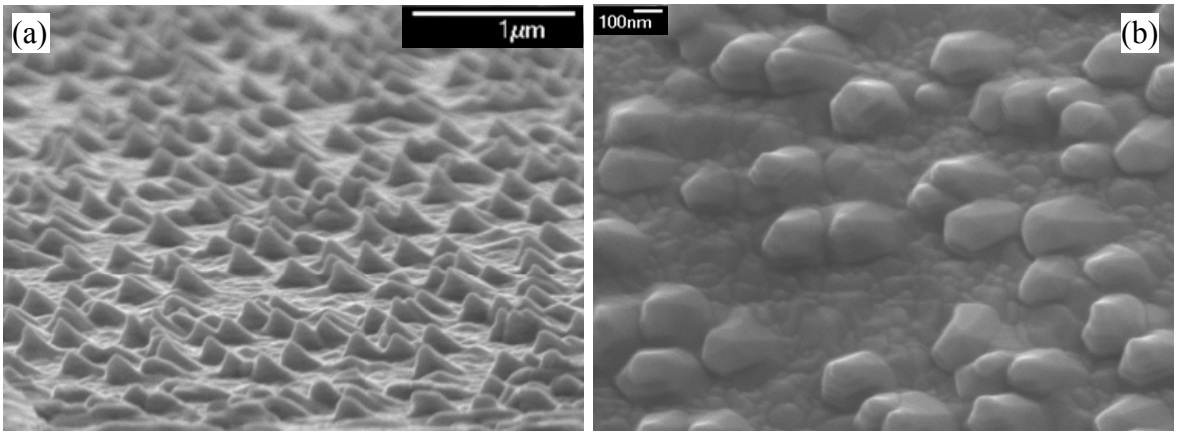

Fig. 2.10. SEM images of sample A600_1, **(a)** near the sample border, **(b)** higher magnification very near to the sample border.

When the substrate temperature is further increased to 650°C (**Fig. 2.11**), the sample appears as a smooth film presenting the same jigsaw-like morphology, and only few pyramidal nanostructures emerge from it. From the higher magnification image (see inset of **Fig. 2.11**) it can be observed that some of these structures still show the hierarchical construction as in the lower-temperature deposited samples. It can be supposed that, at

this higher temperature, the lateral mobility of the depositing species is so high that the lateral growth is highly overcoming the vertical terrace formation, thus resulting in a smooth film where only few hierarchical structures are allowed to grow.

Sample A650_1

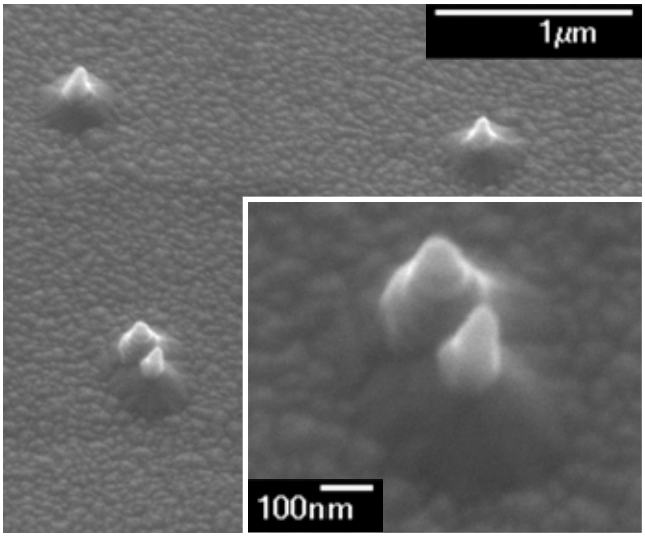

Fig. 2.11. 45°-tilted view of ArF-deposited sample at substrate temperature of 650°C and 1Pa of oxygen background pressure. Inset: higher magnification.

Fig. 2.12 shows the SEM images of samples deposited at substrate temperature of 600°C in 50 and 100 Pa of oxygen pressure. As observed for the KrF-deposited samples at the same temperature and pressures, these samples show the same tendency to grow forming a pencil-array. The columns are somewhat non-uniform in shape and size, with column diameters in the range from ~ 80 to ~ 500 nm, and rather randomly tilted from the substrate normal. However a clear evidence of a hexagonal-like shape can be observed from the images, thus showing that the pencil axis is the c-axis of the wurtzite structure. Comparing the samples grown in 50 and 100 Pa, it can be noticed that sample A600_100 has a better uniformity in shape and size and a more evident tendency to grow in a nearly perfect hexagonal structure (see also inset in **Fig. 2.12(b)**). This behavior is similar to what observed also in samples K600_50 and K600_100, and it is consistent with the growth mechanism assuming, at higher background pressures, the formation of a larger amount of nanoparticles in the gas-phase forming the nucleation sites for the growth of the columns.

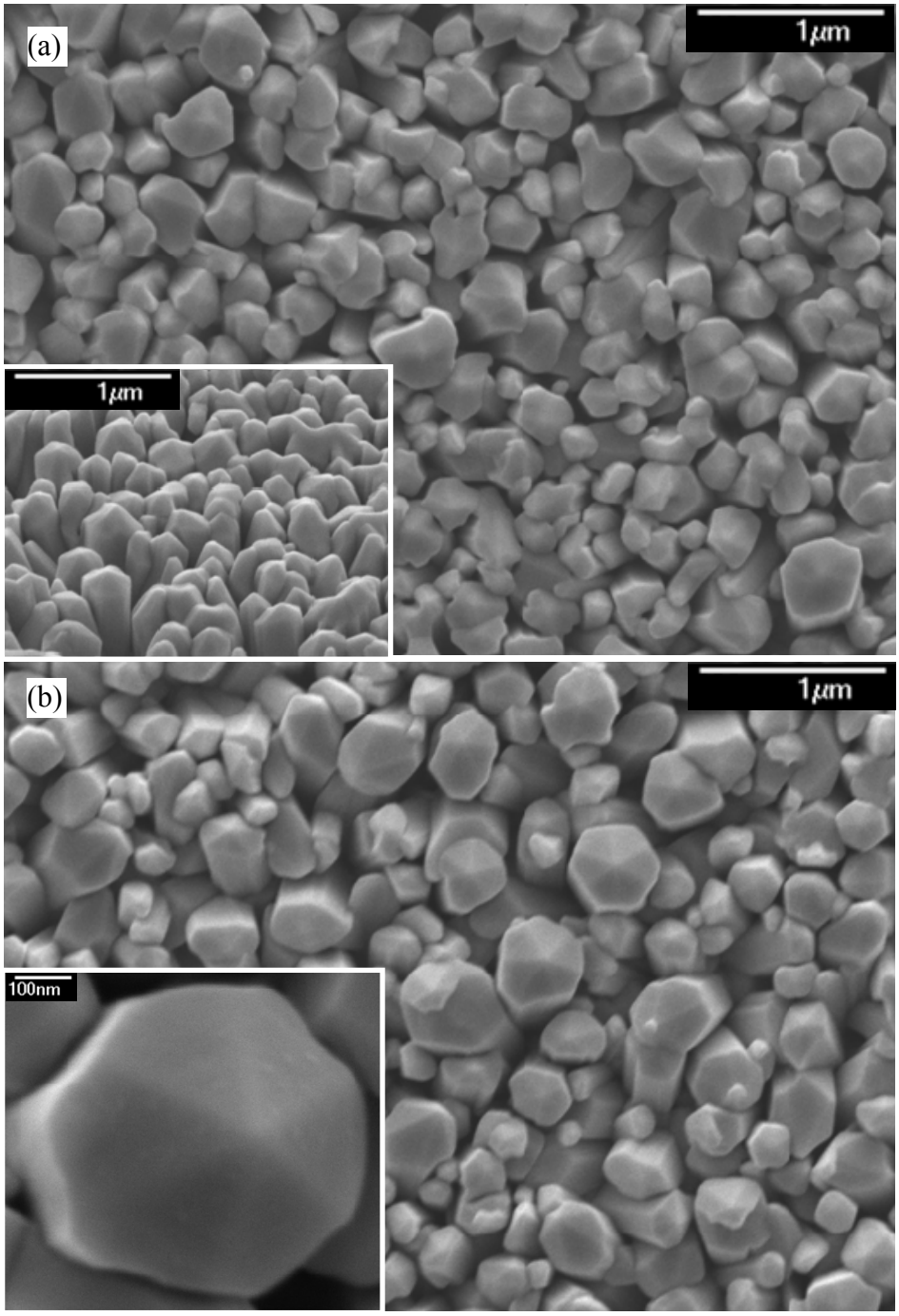

Fig. 2.12. SEM images of ArF-deposited samples at substrate temperature of 600°C and oxygen background pressure of **(a)** 50 Pa and **(b)** 100 Pa. Inset of (a) is a 45°-tilted view, inset of (b) is a higher magnification on the top of a pencil.

Even if the samples deposited at a substrate temperature of 600°C in 100 Pa of oxygen by the KrF and ArF wavelength show the same trend to grow in a pencil-like way, the differences between samples K600_100 and A600_100 are very evident: in the former, the columns are almost perfectly aligned, oriented perpendicularly to the substrate surface and very close-packed, while in the latter the columns are misaligned, not perpendicular to substrate surface and more separated one each other. Moreover the hexagonal shape is much more evident in the ArF-deposited sample. All these differences are compatible with the previously-made hypothesis supposing more energetic depositing species when the 193 nm laser beam is used instead of the 248 nm for the target ablation. Indeed it can be assumed that, due to the higher energy of the species depositing on the substrate, there is a more favorable tendency to arrange in hexagonal wurtzite big crystals but, at the same time, there is also a higher tendency to grow with less ordered alignment and orientation.

As already made for sample K600_100, also for sample A600_100 a look has been taken in proximity of the film border. **Fig. 2.13** shows the cross-section SEM pictures taken near the center and near the border of the sample.

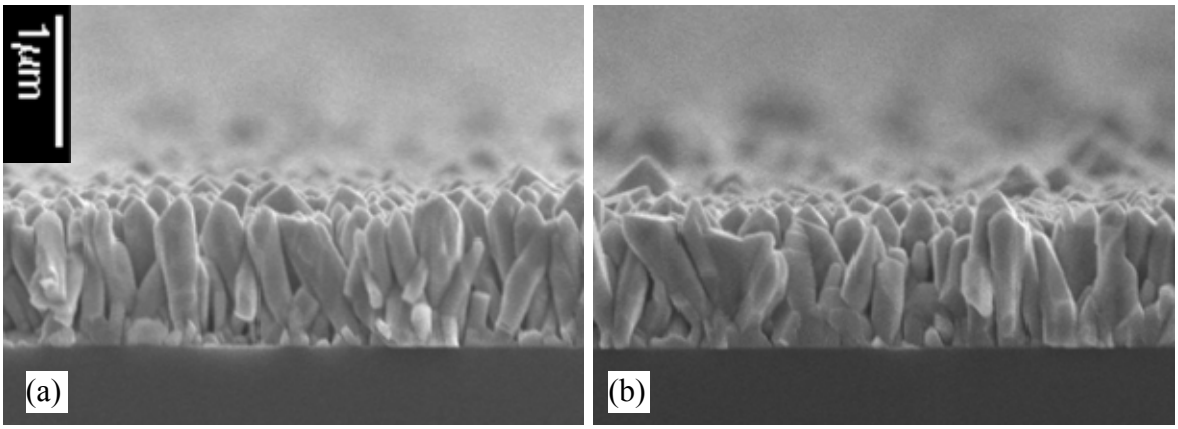

Fig. 2.13. Cross-section SEM views near the center **(a)** and near the border **(b)** of sample A600_100.

First of all, as for sample K600_100, also in this case no evident layer between the rods and the silicon substrate is visible in the images. Near the border of sample A600_100 the rods do not show any tendency to grow inclined toward the center of the sample, while they are still somewhat randomly oriented as in the center of the sample. In

addition it can be seen that the difference in thickness is almost imperceptible in this case: a thickness of ~ 1.2-1.3 μm and ~ 1.15 μm is measured near the center and near the border respectively, corresponding to a difference of about 6-10% from the thickness measured at the center, while it was around 23% in sample K600_100. Again, this observation may be attributed to the possible higher energy of the ablated material, implying a lower confinement of the ablated species in the plasma plume thus allowing that a higher amount of material can reach the more distant regions of the substrate. Anyway it must be taken into account that sample K600_100 is thicker than A600_100 (~ 3.5 μm versus ~ 1.25 μm, measured at the center of the samples) so it cannot be excluded that the per-cent difference in thickness between the center and the border was higher if the growth of the ArF-deposited sample was continued in order to obtain a thicker film.

2.3.c Comparison between KrF and ArF -deposited samples

As a consequence of the results obtained and discussed for samples deposited by using the two different laser wavelengths, some observations can be drawn. These observations, extensively discussed in the different sections of the previous paragraph, are briefly summarized all together here, in order to give a more clear and comprehensive view and to underline the important results.

By KrF laser ablation, a weak tendency to the growth of nanostructures has been observed at low oxygen background pressures, while at high pressure (~ 100 Pa) the samples grew forming rod arrays. This behavior is similar to results reported by other research groups. On the contrary, in ArF depositions the tendency to the growth of nanostructures is stronger, also at low oxygen pressures and low substrate temperatures. A possible explanation for this behavior has been discussed in the previous paragraph and attributed to the ArF higher photon energy.

However, for deposition at low oxygen pressure, a common feature has been observed for both KrF and ArF ablation. A similar jigsaw-like film has been observed as

background in these samples, suggesting a similar growth mechanism, but leading anyway to very different final morphologies.

In high oxygen pressure, for both laser wavelengths, the films showed the formation of a rod-array but, while with KrF the columns were well oriented perpendicularly to the substrate surface, with ArF the structures were tilted in a more disordered way. Moreover the hexagonal shape is more evident in the ArF-deposited films. As discussed in the previous paragraph, also for these behaviors a possible explanation has been suggested in the higher photon energy of the ArF laser beam.

To our knowledge, at present no report in literature exists showing such comparison between these kinds of structures grown by ablation with the two wavelengths and explaining the possible reasons giving rise to the different behaviors. Moreover, in the next chapter, this comparison will be further extended: in particular, important differences will be shown and discussed about the photoluminescence properties of the two sets of samples (KrF and ArF -deposited samples); the reasons of such further differences will be suggested recalling again the higher ArF photon energy.

Chapter 3
Compositional and structural analyses and photoluminescence measurements

Chapter 3 - Overview

In this chapter the results of some compositional, structural and optical analyses performed on the deposited samples are presented, in order to gain information about the quality and properties of the samples.

The first paragraph reports the Energy Dispersive X-ray Spectroscopy (EDS), Rutherford Backscattering Spectroscopy (RBS) and X-Ray Diffraction (XRD) measurements performed on some samples, giving some indications about the good quality of the deposited samples.

In the second paragraph the photoluminescence (PL) spectra of some samples are shown and discussed, confirming their high quality. Additionally, a comparison of the PL properties of samples deposited by using the two different laser wavelengths (248 nm or 193 nm) for the target ablation is presented and the reasons of the observed differences are proposed, referring also to the discussion previously made about the differences in the sample morphology.

Finally, the temperature dependence of the photoluminescence properties is examined for a significant sample, with temperature ranging from 7 K to room temperature. This study allowed to obtain useful information about some PL peak assignments and about the fundamental processes giving rise to the observed photoluminescence at the different sample temperatures.

3.1 Compositional and structural analyses

Energy Dispersive X-ray Spectroscopy (EDS or EDX) standard-less measurements have been performed by using a Philips XL-20 SEM equipped with an eDXi EDAX DX-4 microanalysis system, with an accelerating voltage of 10 keV. The instrument is located at the Department of Physics of the University of Salento.

Rutherford Backscattering Spectroscopy (RBS) has been carried out by a Van de Graaff accelerator using ^{4}He ions with energy of 2 MeV. The accelerator (AN2000) is placed at the INFN *Laboratori Nazionali di Legnaro* (*Padova*). The RBS spectra have been simulated by RUMP (Rutherford Universal Manipulation Program) [151].

X-Ray Diffraction (XRD) measurements have been performed by a Rigaku diffractometer using the $Cu_{K\alpha 1}$ radiation (λ = 1.5405 Å) over a 2θ range from 30° to 80° with steps of 0.05° and integration time of 1 s. The instrument is located at the Dipartimento di Ingegneria dell'Innovazione of the University of Salento.

Fig. 3.1 shows the EDS measurements taken on two samples.

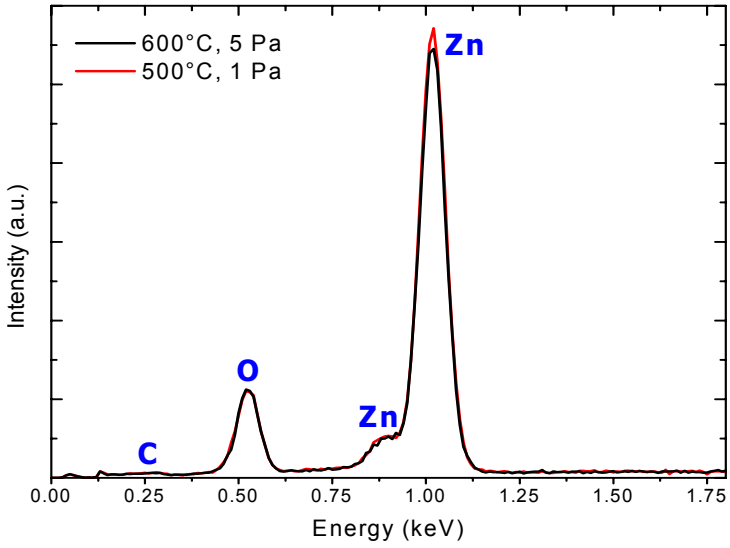

Fig. 3.1. Standard-less EDS analyses for two deposited samples.

The EDS measurements have been performed by a standard-less analysis, thus allowing to get only a qualitative view about elements present in the sample in order to

detect high amounts of possible impurities in the samples, but no quantitative information can be deduced from these EDS analyses. From the spectra it can be observed that zinc and oxygen are the only detected elements, together with a small peak of carbon coming from environment pollutants, while no other contaminant is observed. No other peak is present in the EDS spectra from 1.75 keV up to 10 keV. It must be evidenced that the relative intensities of Zn and O peaks are not associated to the stoichiometry of the sample, since the standard-less analysis does not allow to obtain such information.

On other samples RBS measurements allowed to gain a more quantitative compositional analysis. In **Fig. 3.2** the RBS spectra of four samples are reported.

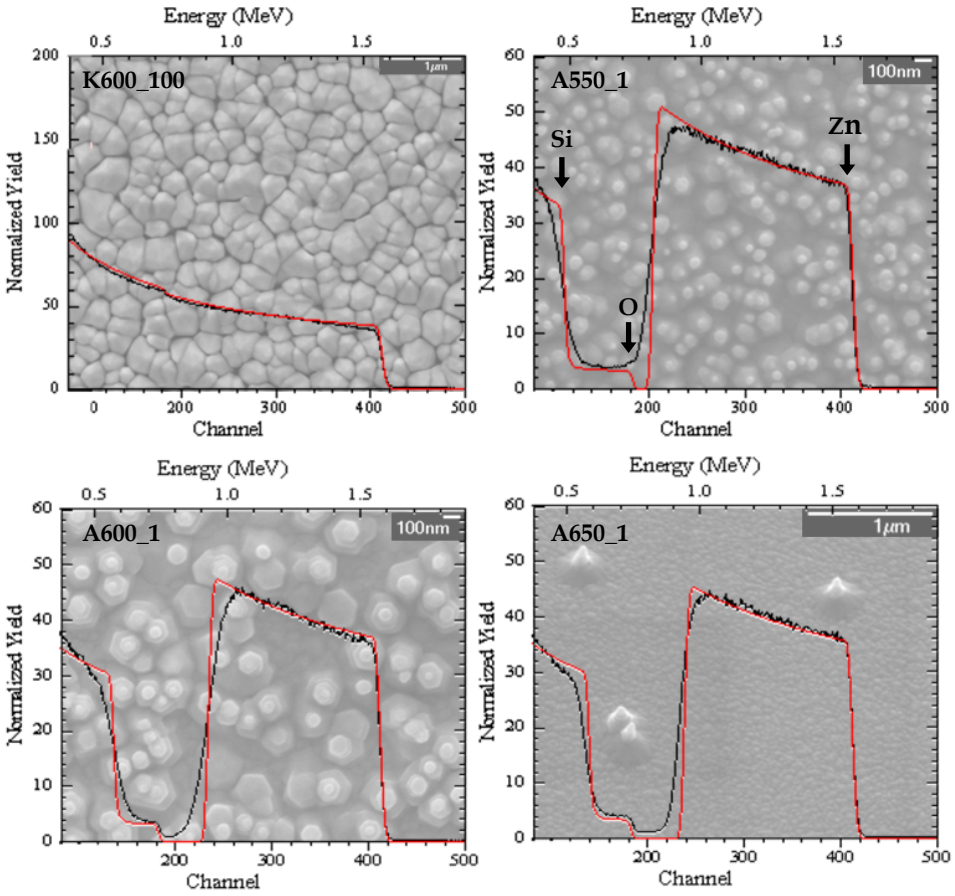

Fig. 3.2. RBS spectra (black lines) of four samples and RUMP simulations (red lines). As background of each spectrum, the SEM image of the relative sample is shown. In the second graph the onset positions corresponding to Zn, O and to the Si substrate are indicated by the arrows.

The RUMP simulations (red curves) well simulate the experimental spectra by setting a Zn:O ratio approximately equal to 1:1, with a maximum discrepancy of about 10%, thus indicating the good composition and stoichiometry of the samples. The slight differences between the simulations and the experimental data around 0.9 MeV can be attributed to a probable slight Zn/Si interdiffusion at the film/substrate interface. The widths of the Zn and O boxes are related to the sample thickness: ~ 1.4 µm for A550_1 and ~ 1.2 µm for A600_1 and A650_1. For sample K600_100 is not possible to estimate a thickness value since it is so thick that the Si box is not visible. However, performing different simulations setting different thicknesses, it can be observed that for thickness values lower than 2.6 µm the Si box is visible, so it can be deduced that sample K600_100 is thicker than 2.6 µm; this result is in agreement with the SEM observations (see par. 2.3.a), showing a thickness value ranging from ~ 2.7 µm near the sample border to ~ 3.5 µm near the center.

In **Fig. 3.3** the XRD spectra of three samples are reported.

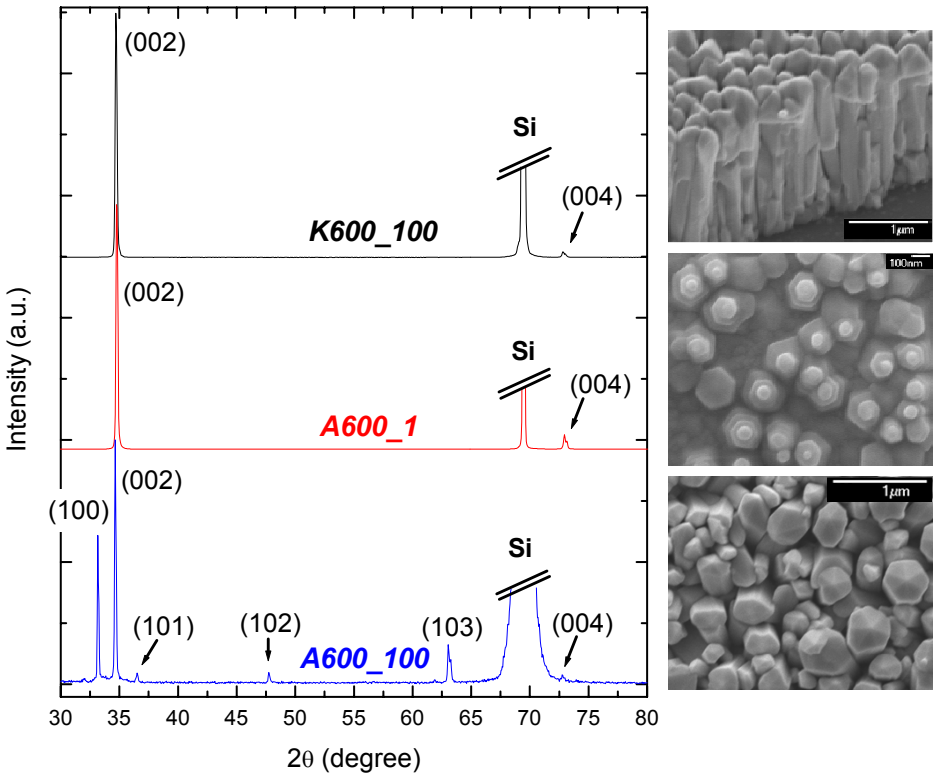

Fig. 3.3. XRD spectra of samples K600_100, A600_1 and A600_100. The spectra are normalized and vertically translated for clarity. Beside each spectrum a SEM image of the corresponding sample is shown for an easy comparison with the morphology.

Apart the peak at ~ 69.2° coming from the silicon substrate, for samples K600_100 and A600_1 only the zinc oxide peaks of the wurtzite planes (002) at ~ 34.7° and (004) at ~ 72.8° are observed, clearly indicating that these samples are grown along the c-axis of the ZnO wurtzite structure. This observation is in good agreement with the discussion made in the previous chapter when the sample morphology was discussed. About sample K600_100 (see par. 2.3.a), from the SEM images the well alignment of the rods was observed, and their growth along the wurtzite c-axis was deduced, thus in accordance with the XRD measurement. About sample A600_1 (see par. 2.3.b), the hexagonal terracing seen in the SEM images clearly indicated the growth of the hierarchical structures along the c-axis; in addition the XRD spectrum allows to suggest that also the jigsaw-like film under the structures is c-axis oriented since it is expected that this film provides a significant contribute to the XRD spectrum and no other peaks, besides the (002) and (004), are visible in the spectrum.

Looking to the XRD spectrum of sample A600_100, other peaks appear besides the (002) and (004). All these peaks can be ascribed to the wurtzite planes (100), (101), (102) and (103). Again, this result indicates that the pencils observed in the SEM images are wurtzite crystals, and the presence of other diffraction peaks is in agreement with the slightly disordered tilting of the structures. It can be noticed that the (100) and equivalent planes, that are the $\{10\bar{1}0\}$ equivalent planes in the 4-index notation*, correspond to the lateral faces of the hexagonal prism (see **Fig. 3.4**), and planes (101), (102) and (103) (the $\{10\bar{1}1\}$ planes in the 4-index notation) correspond to the faces of the hexagonal pyramid on the top of the pencils.

For all the samples, the absence of peaks not-assignable to the ZnO wurtzite structure and the absence of broad peaks or of a background signal in the spectrum indicate the good crystalline quality of the considered samples, demonstrating the presence of only the zinc oxide wurtzite structure without any significant presence of other crystal phases or amorphous phases.

* For the wurtzite structure, sometimes the four Bravais-Miller indices (*h k i l*) are used instead of the three Miller indices (*h k l*). In the 4-index notation the *i* index is related to the *h* and *k* indices by the relation $h + k + i = 0$.

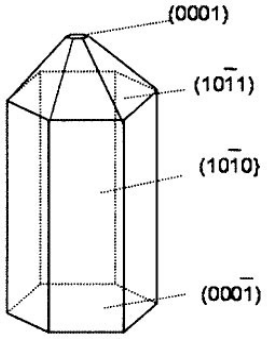

Fig. 3.4. Schematization of the hexagonal pencils with the corresponding crystal faces of the wurtzite crystal structure in the 4-index notation. (Image from ref. [152]).

3.2 Photoluminescence properties

In order to get further information on the quality of the deposited samples, their photoluminescence spectra at room temperature (RT) and low temperature (~ 7 K) have been acquired and examined. In particular, these measurements show (see par. 3.2.b) that the sample quality increase when increasing the oxygen background pressure used during the depositions and that the quality of the ArF-deposited samples are better than the KrF-deposited ones. Additionally, for sample A600_1, representing one of the samples with the finest PL properties, also a study of the dependence of the PL emission on the temperature has been conducted varying the sample temperature from 7 K to room temperature.

3.2.a Experimental set-up

The excitation source was the 325 nm line delivered by a continuous wave He-Cd laser (Kimmon IK Series). The laser beam was focused onto the sample by a f = 5 cm lens, resulting in a spot dimension of ~ 130 μm and a power of ~ 6 mW. The sample was fixed

on the cold finger of a cryostat by silver-paste to ensure a good thermal conduction, and the cryostat chamber was evacuated by a rotary pump down to less than 10^{-5} Pa. The pressure was monitored by a Varian Eyesys ConvecTorr vacuum gauge operating in the range from atmospheric pressure to ~ 10^{-5} Pa. The cryostat allowed to reach a minimum temperature of ~ 7 K through a Sumitomo CKW-21 Helium Compressor Unit, and an electrical resistance was controlled by a LakeShore temperature controller measuring the cold finger temperature by a thermocouple and changing the applied voltage to the resistance in order to keep constant the set temperature. The sample PL was collected by the same lens focusing the laser beam and sent to a second lens (f = 10 cm) focusing the collected sample emission into the entrance slit of a Jobin Yvon SPEX TRIAX320 monochromator. The TRIAX320 is a Czerny-Turner monochromator with 32 cm focal length and a 1200 lines/mm grating; the instrument has a nominal spectral dispersion and a resolution of 2.64 nm/mm and 0.06 nm respectively, at 500 nm and for a slit aperture of 10 µm. Since for the all the measurements presented in this thesis the slit aperture was set to 100 µm, the nominal resolution of the instrument at 500 nm was 0.6 nm. The output at the monochromator exit was detected by a Hamamatsu GaAs photomultiplier tube, cooled down to -30°C by a Hamamatsu Peltier cooler, and operating in single photon counting mode.

All the recorded PL spectra were corrected with the spectral efficiency curve of the grating inside the monochromator.

3.2.b Photoluminescence measurements

In the main panel of **Fig. 3.5(a)** the photoluminescence spectrum of sample K600_1 at temperature of 7 K is reported with the intensity axis in linear scale. It can be seen that the main emission is at ~ 3.372 eV (~ 367.7 nm), coming mainly from donor bound exciton recombination (see par. 1.2.a) while the visible band is hardly detectable in this view. In order to observe further details the spectrum is reported in the inset of **Fig. 3.5(a)**, together with the spectrum at room temperature, with the intensity axis in logarithmic scale.

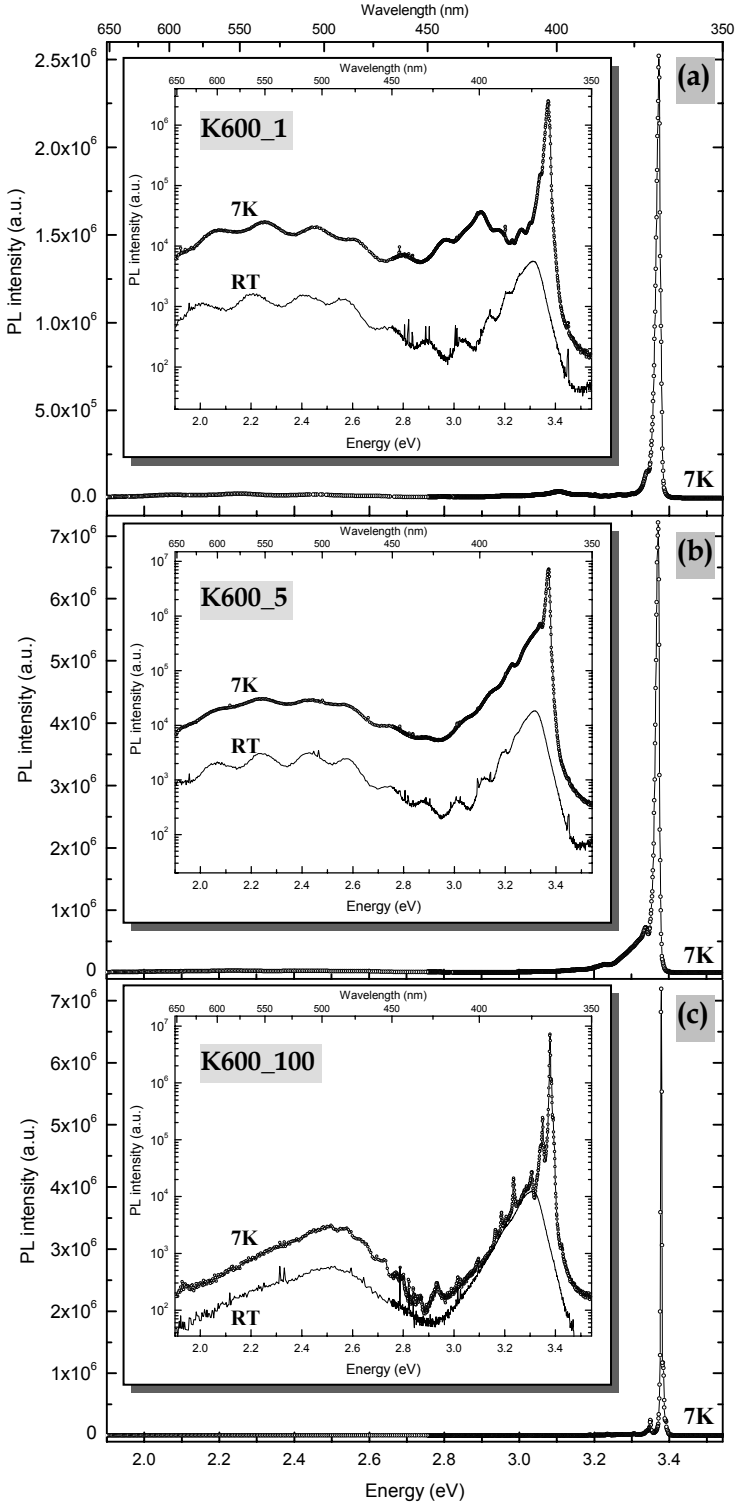

Fig. 3.5. Main panels: PL spectra of samples **(a)** K600_1, **(b)** K600_5 and **(c)** K600_100 at temperature of 7 K, with intensity axis in linear scale. Insets: PL spectra at 7 K and room temperature, with intensity axis in logarithmic scale.

The excitonic peak at 7 K is narrow, with a full width at half maximum (FWHM) of 13 meV, and the intensity of the excitonic peak emission is about 100 times higher than the intensity of the visible band centered at about 2.3 eV (~ 540 nm), thus indicating a fair, but not excellent, quality of the sample. Inside the visible (green) band, probably related to oxygen vacancies as discussed in par. 1.2.a, several peaks are visible; these peaks may be due to multiphonon emission but also to different transitions involving deep levels inside the band-gap since, as seen in par 1.2.a and in **Fig. 1.4**, many different energy levels can be introduced inside the gap by several defects. Also a band in the range ~ 2.9-3.2 eV (~ 385-430 nm) is visible in the low-temperature spectrum: as told in par. 1.2.a, emission in this range has usually been attributed to emission from zinc-related defects, like zinc interstitials.

Looking to the RT PL spectrum, it can be observed that the overall luminescence intensity is lower with respect to the low-temperature emission due to the increasing effect of non-radiative relaxations. The excitonic emission (now coming mainly from free exciton emission, as described in par. 1.2.a) is shifted to lower energy as expected due to band-gap shrinkage (see next paragraph), it is broader and some phonon replicas are visible. At room temperature the ratio between the intensity of excitonic emission and visible band is lower than the ratio in low-temperature spectrum, indeed it is only about 3, versus about 100 at 7 K.

The observations discussed above show the nearly good quality of sample K600_1, but some evidences of the presence of defects have been evidenced by the PL spectra.

About the PL of the KrF-deposited sample at 5 Pa of oxygen background pressure (**Fig. 3.5(b)**) it can be observed that the emission probably coming from zinc-related defects is less evident compared to sample K600_1, but a clear tail in the range 2.9-3.2 eV is still visible thus indicating the presence of emission coming from defects also in this sample. The FWHM of the excitonic peak of sample K600_5 is ~ 12 meV, almost the same as sample K600_1, but the intensity of the excitonic peak emission is ~ 240 times higher than the intensity of the visible band at low temperature, and ~ 6 times at room temperature; these ratios are about twice the ratios measured for sample K600_1. Assuming that the green band originates from oxygen vacancies, then this last result is

expected since a higher oxygen pressure has been used for the deposition of K600_5 and thus probably there is a lower content of oxygen vacancies than in sample K600_1. As a consequence, sample K600_5 seems to be slightly better than K600_1, but its PL spectrum still evidences the presence of some defects.

Very significant differences can be noticed in the PL spectra of the KrF-deposited sample in high oxygen pressure of 100 Pa. **Fig. 3.5(c)** reports the PL spectra of sample K600_100 at 7 K and RT. The spectra are very similar to the typical high-quality ZnO PL spectra (see e.g. Fig. 1.2(a)). The excitonic peak is very narrow, with a FWHM of ~ 3.7 meV, and the ratio between the intensities of the excitonic emission and the visible band is about 2300 at low temperature and about 22 at RT. This last result is again expected due to the high oxygen pressure used for the deposition of the sample. Moreover at 7 K in the excitonic range several peaks are clearly visible. In order to attempt an attribution of the different peaks to the various transitions discussed in par. 1.2.a, in **Fig. 3.6** a magnification of this region is shown.

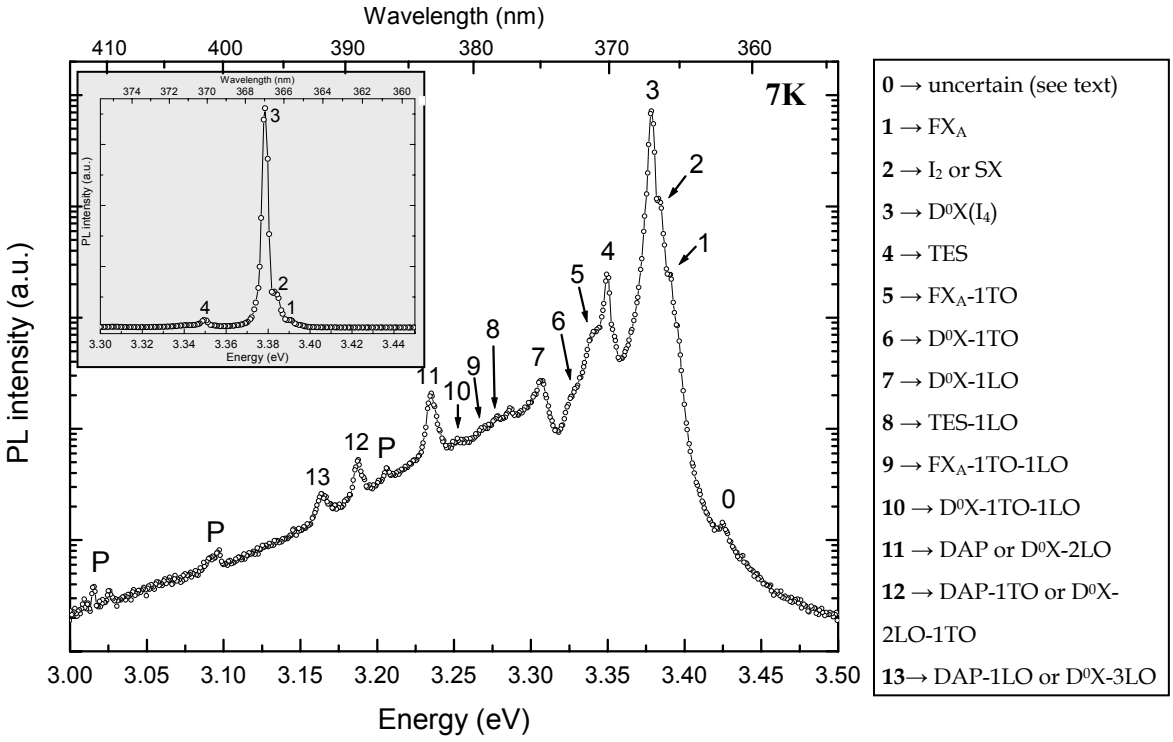

Fig. 3.6. Magnification of the excitonic emission of sample K600_100 at 7 K in semi-Log scale. Inset (gray background): magnification in linear scale. See text for peak assignments.

Apart the He-Cd laser plasma lines, labeled with *P* in the figure, at least thirteen peaks, labeled with numbers from *1* to *13*, are notable, while for peak labeled with *0* there is some uncertainty (see below). The prominent peak, labeled with number *3*, is placed at 3.379 eV and, according to the literature (see par. 1.2.a), it is usually attributed to a neutral donor bound exciton and maybe to transition I_4, thus here it is indicated as $D^0X(I_4)$. On its right side, two shoulders (peaks *1* and *2*) are evident. Peak *1* has an energy distance of 13 meV from peak *3*, matching the localization energy of line I_4 from FX_A (see **Tab. 1.3**) therefore this peak can be attributed to the FX_A transition. For peak *2*, two reasonable assignments are possible: basing on its energy distance from the FX_A (~ 8 meV), close to the I_2 localization energy, this peak can be attributed to the I_2 transition (ionized donor bound exciton); however in literature this shoulder has been often related to surface exciton emission (*SX*) [92-95] basing on the observation that it is present in nanostructured samples but not in bulk samples. The assignment of peak *2* to *SX* emission is plausible also for sample K600_100 since from the observation of its morphology (see par. 2.3.a) it is deducible a high surface-to-volume ratio, therefore it is plausible that surface states can give a significant contribution to the sample photoluminescence.

The attribution of peak *0* is somewhat uncertain since it cannot be totally excluded that this small peak comes from the laser. All the other plasma lines are observed also in the RT spectrum, but this peak seems to be absent in the RT spectrum, thus suggesting that it is related to the sample emission. Its distance from the FX_A peak is ~ 36 meV thus, if it comes from sample emission, then it could be the excited state of the free exciton, reported with a separation of ~ 40-45 meV from the ground state [75, 76]; it seems less probable that it is the emission of the FX_C (*A*-*C* splitting ~ 48.6 meV at 1.6 K) since this transition is forbidden for some light polarizations [75, 67].

Basing on literature observations and on its separation from peak *3*, peak *4* is attributed to the *TES* transition of the donor bound exciton; indeed its separation is ~ 30 meV, comparable with the separation between line I_4 and its *TES* line (~ 34 meV in **Tab. 1.3**). Since peaks *5* and *6* are placed at energies of ~ 51 meV lower than peaks *1* and *3* respectively, they are assigned to *TO* phonon replicas of the *FX* and D^0X transitions respectively. Peaks *7* and *8* are at an energy distance of ~ 72 meV from peaks *3* and *4*

respectively, hence they are attributed to *LO* phonon replicas of D^0X and *TES*. Peak *9* is at energy ~ 72 meV lower than peak *5*, thus it can be the phonon replica of FX_A resulting from the interaction of one *TO* phonon and one *LO* phonon. Similarly, peak *10* is at energy distance of ~ 72 meV from peak *6* and ~ 51 meV from peak *7*, thus suggesting that this peak is a phonon replica of the D^0X transition due to the interaction with one *TO* phonon and one *LO* phonon. On the base of observations from literature, peak *11* is ascribed to the *DAP transition*; however, since its energy position is ~ 72 meV lower than peak *7*, it can be also the 2*LO* phonon replica of the D^0X. Peaks *12* and *13* can be attributed respectively to the *TO* and *LO* phonon replicas of peak *11*, on the base of their respective separations. A summary of the peak attribution is reported beside the PL spectrum in **Fig. 3.6**. The first four peaks are also clearly visible when the PL spectrum is plotted in linear scale (see inset of **Fig. 3.6**).

It should be noticed that the very narrow FWHM, the high ratio between excitonic and defect emission intensities and the distinctness of several peaks in the low temperature PL spectrum of sample K600_100 point out its excellent crystalline quality, also suggested from the XRD spectrum (see par. 3.1). This feature indicates a high improvement of the sample quality when high oxygen pressure is used for depositions by KrF laser ablation.

From the study of the sample morphology presented in the previous chapter, it was evidenced that ArF-deposited samples showed very different morphology in comparison with the KrF-deposited ones. It can be expected that notable differences should be observed in the PL spectra too.

The low-temperature PL spectra of samples A550_1 and A600_1 are reported in **Fig. 3.7**. The excitonic peak is very narrow for both samples: the FWHM is ~ 7.5 meV for sample A550_1 and ~ 5 meV for sample A600_1. The ratio between excitonic emission and visible band intensities at 7 K is about 1700 and 11000 for sample A550_1 and A600_1 respectively, and about 24 and 63 at room temperature. Moreover in the excitonic region it is possible to distinguish several peaks; in the inset of **Fig. 3.7** these peaks are labeled from *1* to *11* (a visible plasma line is labeled with P) and, as explained for the peak assignment

for sample K600_100, they have been attributed to the different transitions: the results are reported beside the PL spectrum.

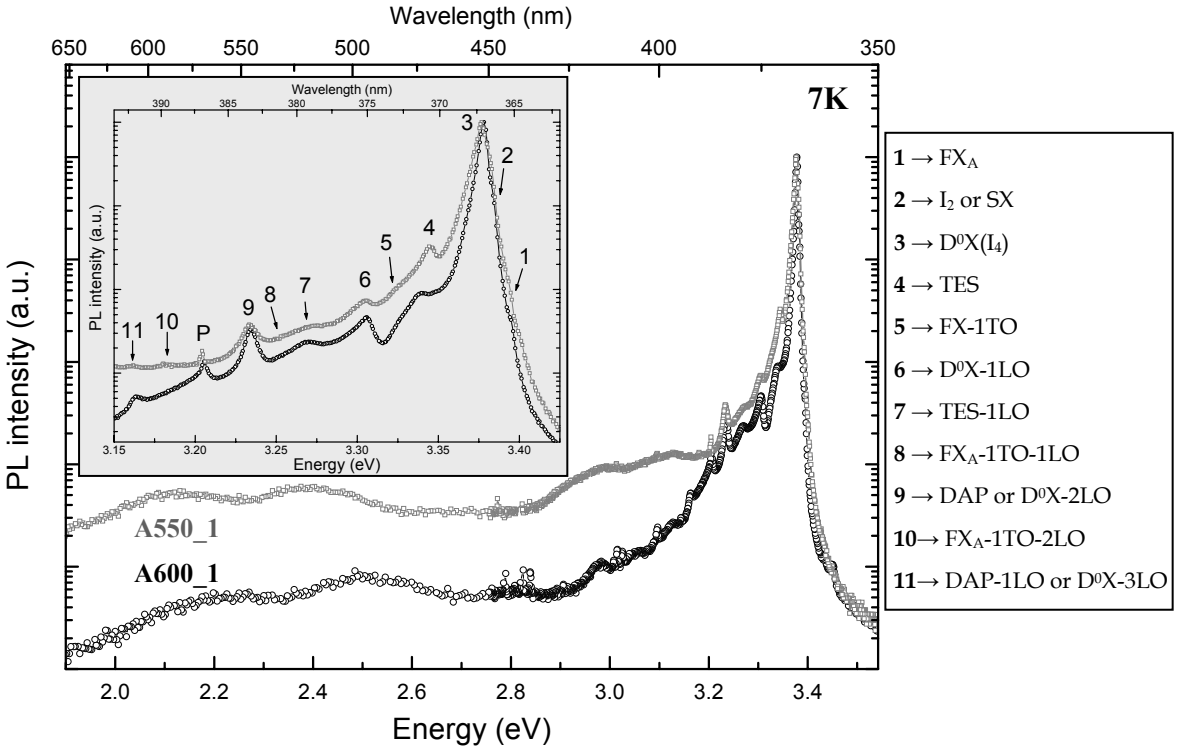

Fig. 3.7. PL spectrum of samples A550_1 and A600_1 at 7 K. Inset (gray background): magnification of the excitonic region. The spectra are normalized on the main peak for a better comparison. See text for peak assignments.

Again, as observed before, the very high ratios between exciton and visible emission, the narrow FWHM and the evidence of several well-distinguishable peaks in the exciton region are indication of the excellent quality of the samples. Comparing the spectra of the two samples it can be seen that a slight band in the range ~ 2.9-3.2 eV is visible in sample A550_1, while it is absent in sample A600_1. Moreover, as observable in the inset of **Fig. 3.7**, the peaks related to the different transitions in the excitonic range are sharper in the spectrum of sample A600_1. These observations, together with the narrower FWHM and lower visible emission, indicate the better quality of sample A600_1 with respect to A550_1. The goodness of this sample was also suggested by the XRD analysis shown in

par. 3.1. Due to the very good quality of the PL spectrum of sample A600_1, for this sample a more detailed study of the temperature dependence of the photoluminescence is reported in par. 3.2.d.

In **Fig. 3.8** the low temperature PL spectra of samples A600_50 and A600_100 are reported.

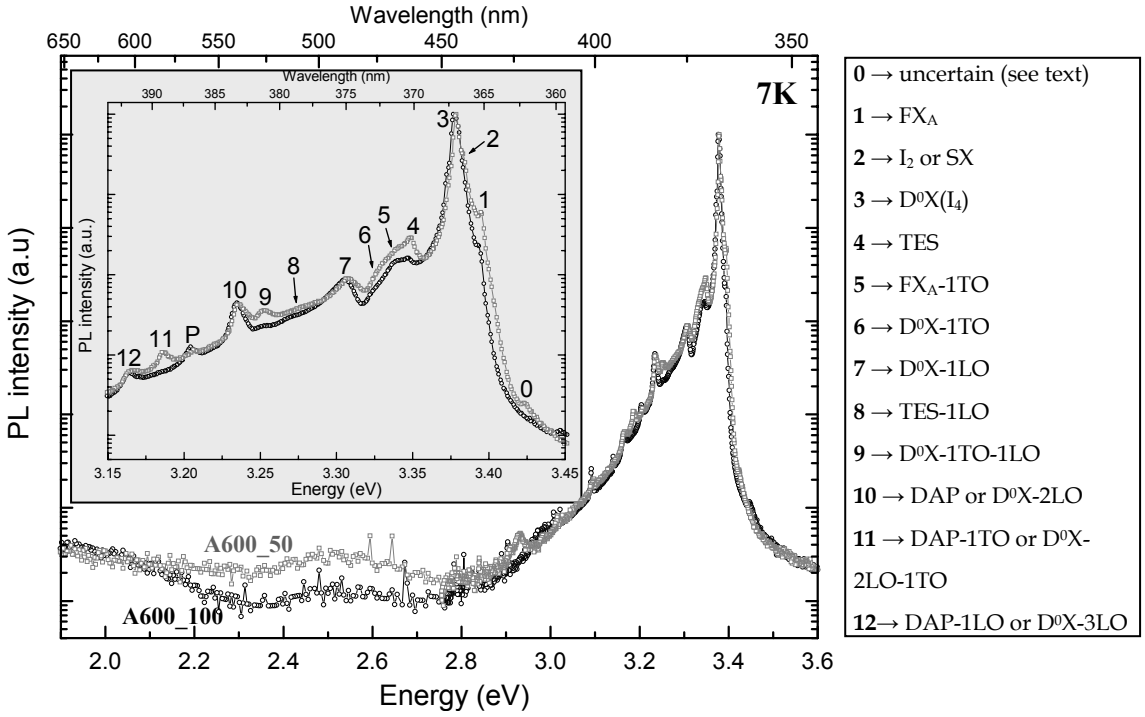

Fig. 3.8. PL spectrum of samples A600_50 and A600_100 at 7 K. Inset (gray background): magnification of the excitonic region. The spectra are normalized on the main peak for a better comparison. See text for peak assignments.

Again the PL spectra show the excellent quality of the deposited samples. Indeed the FWHM of the excitonic peak is very low for both samples (~ 4 meV for sample A600_50 and ~ 6 meV for sample A600_100), several peaks, assigned to the different transitions as made for the previous samples, are clearly visible in the excitonic range and the green band is almost totally absent as expected due to the high oxygen pressure used in the depositions. At 7 K the ratio between exciton and green emission is ~ 29000 for sample A600_50 and ~ 57000 for sample A600_100, while at room temperature the intensity of the

green band is so low that it is almost indistinguishable from the background noise of the measurement; as expected, the sample deposited at higher oxygen pressure has a lower green band since it would have a lower content of oxygen vacancies.

An interesting feature observable in the PL spectra of both A600_50 and A600_100 samples is the appearing of a modest yellow-orange band at energies lower than 2.2 eV. As reported in par. 1.2.a, in literature the emission in this spectral range has been attributed to oxygen interstitials. Also this observation is attributable to the high oxygen pressure used in the depositions. Therefore it can be deduced that high oxygen background pressure contributed to almost eliminate the oxygen vacancies in the sample, since the green band is almost totally absent, and to cause a slight incorporation of oxygen interstitial as deduced from the slight yellow-orange band.

Comparing the PL spectra of samples A600_50 and A600_100 with the sample deposited by ArF ablation at the same substrate temperature and lower oxygen pressure (A600_1), it can be inferred that samples deposited in high pressure have a slightly better quality since they show a lower green band and the different transitions in the excitonic range are slightly better distinguishable. The same improvement of the sample quality deposited in high oxygen background pressure was observed also for the KrF-deposited samples.

3.2.c Comparison between KrF and ArF -deposited samples

From the results reported above in the discussion of the photoluminescence properties of the deposited samples, it can be easily observed that the PL properties of samples deposited by ArF laser ablation are better than those of the KrF-deposited samples. The ArF-deposited samples show PL spectra which are typical of good-quality zinc oxide: the excitonic peak has a very narrow width and a well-resolved separation of many different transitions, and the emission coming from defects is very low (nearly totally absent in some samples). Among KrF-deposited samples, only sample K600_100 shows features, like narrow width of the excitonic peak and several well-distinguishable

peaks, which can be compared with the ArF-deposited samples, but anyway its PL spectrum still evidences the presence of some emission coming from oxygen vacancies. A possible explanation for this observation can be found, as already suggested in the discussion about the sample morphology, in the higher photon energy of the ArF laser beam. Indeed this higher energy may results in two effects:

1. As proposed in par. 2.3, the higher ArF photon energy may cause a more energetic plasma plume with respect to KrF ablation. As a consequence the depositing species may have a higher energy, thus allowing the growth of samples with a better crystalline quality. This quality is then evidenced in the PL spectra.
2. In addition it should be noticed that the O_2 molecule has dissociation energy of 5.1 eV [153]. Hence ArF laser photons, having an energy of 6.42 eV, are able to produce a higher dissociation of oxygen molecules than KrF laser photons, having an energy of 5 eV. Moreover, as stated in par. 2.3, it is likely that higher-energy photons of the ArF laser beam produce more ionized and electronically excited, and thus more reactive, ablated species. These two effects imply that during ablation and deposition by the ArF laser beam, the ablated species may react better with the surrounding background oxygen molecules, thus allowing the formation of more stoichiometric samples (that is with less oxygen vacancies). As a consequence this observation may explain why for KrF depositions the PL green band is still present even in the spectrum of sample deposited in high oxygen pressure (~ 100 Pa): the oxygen dissociation and the presence of ionized and electronically excited species in the KrF-generated plume are lower than with ArF; thus even at high oxygen pressure the KrF-deposited samples present oxygen deficiency, while the ArF-deposited ones are more stoichiometric even at low oxygen pressure.

All the discussion made above, reporting the comparison of the PL properties of KrF and ArF -deposited samples together with the possible reasons giving rise to the observed differences, enriches the comparisons illustrated in the previous chapter for the sample morphology. The comparisons between the two ablating wavelengths for both sample

morphology and PL properties and the possible suggested explanations represent an important result in understanding the processes causing the growth of different nanostructured samples when different ablating wavelengths are used.

3.2.d Temperature dependence of the PL properties

- *General features*

Temperature-dependent PL measurements are a very useful tool in order to obtain information about the quality of the studied material. Moreover the temperature dependence of the different ZnO PL peaks may help in the assignment of the various transitions observed above, since they can show some differences in their temperature behaviors.

A known observation about temperature-dependent PL measurements is that when the temperature decreases the PL efficiency increases. Indeed, when the temperature increases there is an increase in the number of charge-carriers which undergo non-radiative relaxations due to trapping in thermally activated non-radiative centers or to scattering with phonons. As a consequence of the increasing of the PL efficiency at low temperature, both the near band-edge emission (UV emission) and the defect emission rise, but, as seen in the PL measurements reported above, it can be observed that the ratio between the UV PL intensity and the defect PL intensity increases when the temperature decreases. Moreover, due to reduced scattering between charge-carriers and phonons when decreasing the temperature, the different peaks are narrower at lower temperatures, allowing a better possibility to distinguish them; also this feature was clearly evident in the previously shown PL spectra.

As stated in par. 1.2.a, ZnO low-temperature spectrum is dominated by emission from bound-excitons *BX* (generally considered bound to neutral donors). Free-exciton *FX* emission can also be observed, but is much less intense than *BX* emission. Other peaks, such as *TES*, *DAP* and phonon replicas are also usually observed in good-quality samples.

As the temperature increases the whole emission becomes less intense, but the *FX* starts to be more evident since the *BX* begins to dissociate into *FX* [154]. Meanwhile all the peaks become broader and their overlap increases. Another typical observation is that the *FX* phonon replicas stand at high temperatures, while the *BX* ones tend to disappear together with the main *BX* emission; this behavior can be attributed to two different reasons: the first one is the reduction of the *BX* emission itself due to *BX* dissociation into FX, thus its phonon replicas decrease too; the second reason has been ascribed to the fact that the coupling between *FX* and phonons is stronger than the coupling between BX and phonons [155]. As a consequence of all this behaviors, at room temperature the PL results in a broad spectrum made by the convolution of the *FX* emission with its residual phonon replicas (see RT PL spectra reported above).

- *Energy gap (Varshni equation)*

Semiconductor band-gap varies with temperature due to lattice expansion/shrinkage and to interaction with phonons. In particular, for most semiconductors, the band-gap shrinks when temperature increases. As a consequence, for transitions involving the bottom of the conduction band or the top of the valence band (like the *FX* and *BX* transitions), a shift of the peak position towards lower energies (*red-shift*) is observed when temperature increases.

As usual for most semiconductors, also for zinc oxide this temperature-induced shift can be well described by the semi-empirical Varshni equation [156-158]:

$$E(T) = E(0) - \frac{\alpha T^2}{T + \beta} \qquad \textbf{Eq. 3.1}$$

where *E(T)* and *E(0)* are the energies of the considered peak at temperature *T* and *0 K* respectively, and α and β are characteristic parameters of the material. Generally, for bulk semiconductors, α is close to the *temperature coefficient* of the material and β is close to the *Debye temperature* of the material. Typical α and β values for bulk ZnO are reported in **Tab. 1.2** extracted from ref. [159].

- *Peak area (Arrhenius formula)*

The increasing temperature causes a decrease (quenching) of the photoluminescence intensity. As a consequence, the integrated area of a PL peak decreases with the increasing temperature. A typical way to describe this behavior is given by the Arrhenius formula:

$$I(T) = \frac{I(0)}{1 + A\exp[-E_a / kT]} \qquad \textbf{Eq. 3.2}$$

where $I(T)$ and $I(0)$ are the integrated areas at temperature T and 0 K respectively, E_a is the thermal activation energy of the mechanism causing the PL quenching, A is a parameter related to the probability of the thermally activated process, and k is the Boltzmann constant.

Sometimes more than one thermally activated process contribute to the PL quenching with the increasing temperature. For example, if two processes are considered, then the Arrhenius formula can be written as:

$$I(T) = \frac{I(0)}{1 + A_1\exp[-E_{a1} / kT] + A_2\exp[-E_{a2} / kT]} \qquad \textbf{Eq. 3.3}$$

where E_{a1} and E_{a2} are the thermal activation energies of the two mechanisms, and A_1 and A_2 are related to the respective probabilities.

- *Temperature dependence of the photoluminescence of sample A600_1*

For sample A600_1, which is one of the samples with the best PL spectra, a study of the photoluminescence properties was conducted varying the sample temperature from ~ 7 K to room temperature, for a total number of 17 different set temperatures. Before acquiring each spectrum, the laser output power was measured in order to exclude variations in the sample emission produced by variations in the power of the excitation source.

As shown later, this study allows to support the peak assignments made before (par. 3.2.b), to better understand the mechanisms influencing the PL emission when the sample

temperature is varied and to extract some fundamental parameters related to such mechanisms.

Fig. 3.9 shows the PL spectra of sample A600_1 for all the investigated temperatures; for more clarity the spectra are vertically translated. Since the exciton region is highly structured, presenting several different peaks close one to each other, the measurements were acquired with steps of 0.1 nm† in the spectral range 340-430 nm (~ 2.88-3.65 eV); for the less-structured region of the spectrum, in the range 430-650 nm (~ 1.9-2.88 eV), a step of 0.5 nm was used.

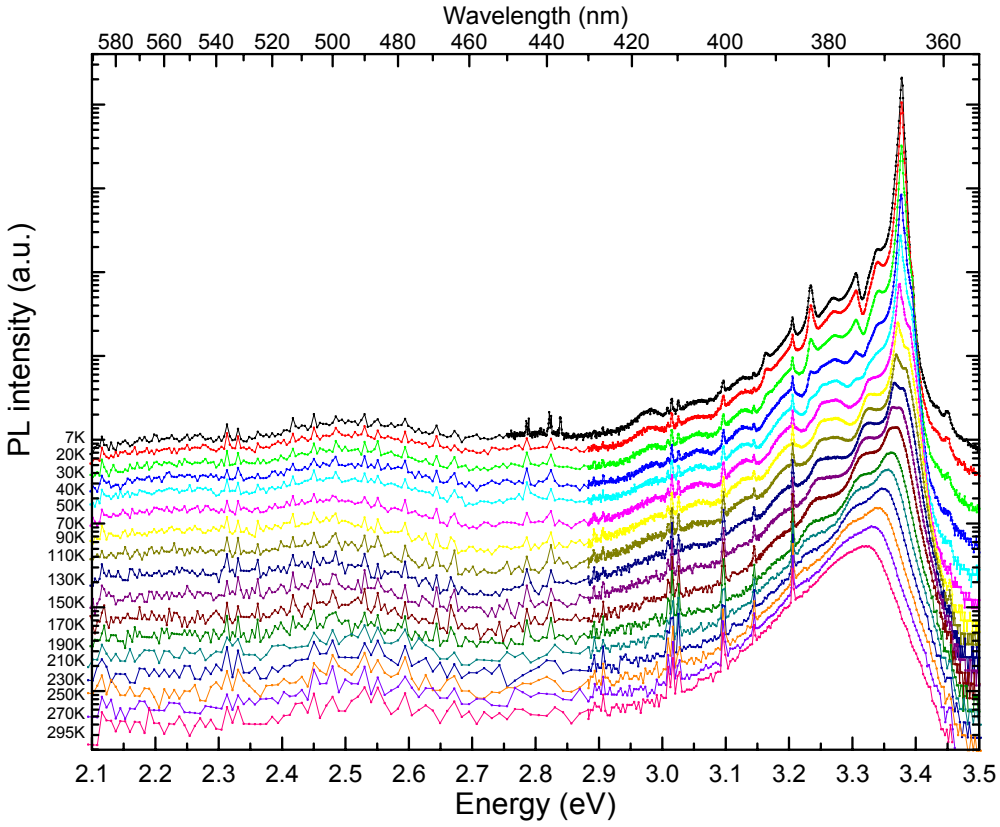

Fig. 3.9. PL spectra of sample A600_1 at temperatures from 7 K to room temperature. The spectra are vertically translated for clarity.

† The measurement step was intentionally chosen lower than the instrument resolution, in order to be sure that the instrument resolution is the limiting factor for the measurement resolution.

From the figure some behaviors are evident when the temperature increases: the excitonic emission shifts to lower energies, broadens and becomes less structured. At low temperature in the excitonic range‡ several transitions are clearly visible while at room temperature the excitonic emission is a broad peak constituted by the *FX* emission and some phonon replicas.

In the visible region, no evident shift of the emission bands is seen. However it must be underlined that, due to the very low emission intensity in this range, it is hard to deduce definite behaviors. Anyway it can be commented that if the visible band does not shift with temperature, then it is likely that the observed emission is not due to the direct transition between electrons in the conduction band and the deep level introduced by the defect, but that it is due to transitions from shallow defect levels to the deep levels [160].

Fig. 3.10(a) and **Fig. 3.10(b)** show two subsequent enlargements of the excitonic region, in order to better illustrate the behavior of the various transitions in this spectral range when the sample temperature changes. The attribution of peaks labeled from *1* to *11* to the different transitions was reported in **Fig. 3.7**. Peaks *12* and *13* were not reported in the inset of **Fig. 3.7** since a slightly shorter range was displayed there; basing on their energy separations from the previous peaks, *12* and *13* can be assigned to the FX_A phonon replicas FX_A*-1TO-3LO* and FX_A*-1TO-4LO* respectively. **Fig. 3.10(a)** and **Fig. 3.10(b)** allow to better see the red-shift of the different peaks and the broadening of the PL spectrum when the sample temperature increases. Moreover it can be seen that at higher temperature the different peaks become less distinguishable and some of them tend to disappear while others tend to become more evident. For example, in the figures it is well observable that the *FX* emission (peak *1*) is slightly evident at low temperature, while it becomes predominant as the temperature increases. At the same time the D^0X emission (peak *3*) is the main peak at low temperature, while it is almost undetectable above 150 K. As previously stated, this behavior can be ascribed to dissociation of D^0X into *FX*, therefore it represents a support of the assignment, made in par. 3.2.b, of peaks *1* and *3* to *FX* and D^0X emissions respectively.

‡ Here the excitonic range is intended as the range from ~ 3 eV to ~ 3.5 eV.

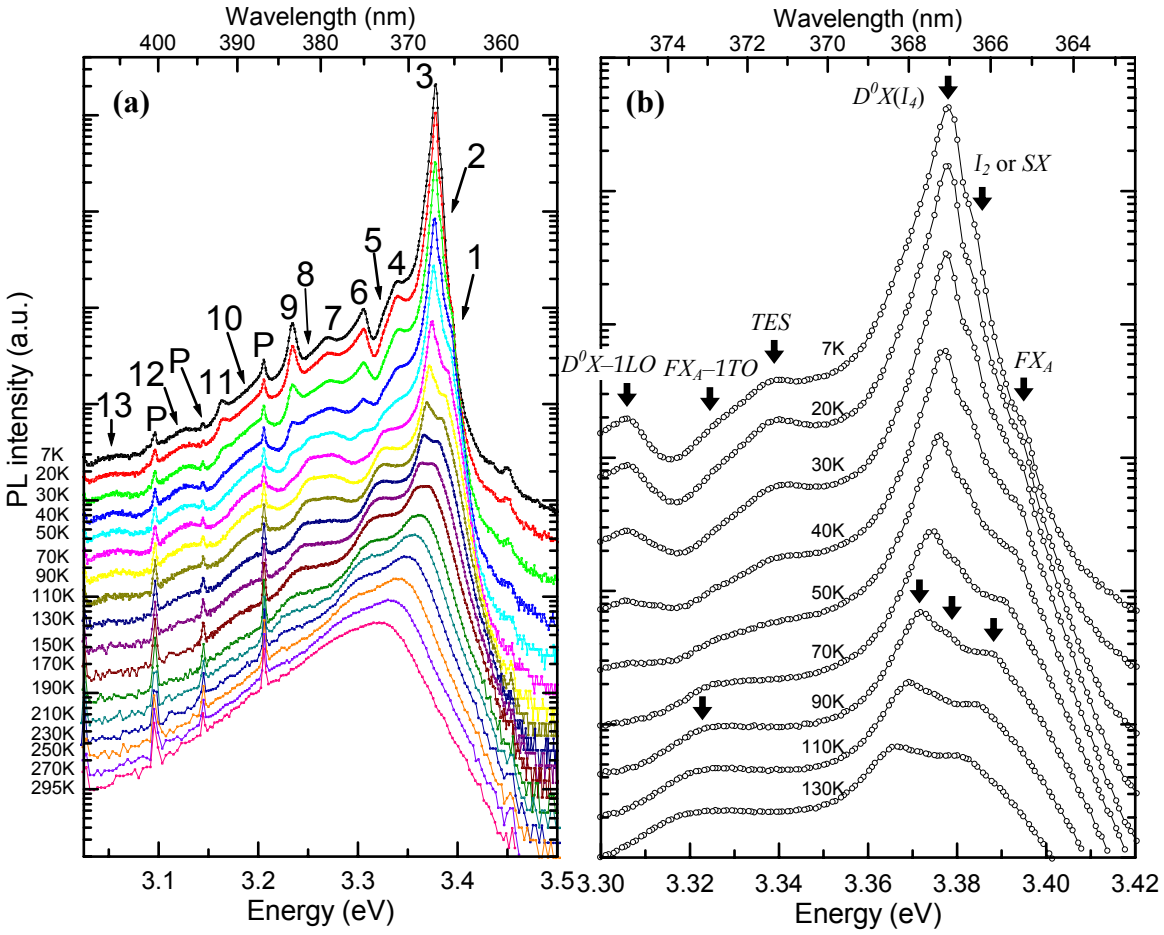

Fig. 3.10. (a) Excitonic region of the PL spectra of sample A600_1 with temperature from 7 K to room temperature; see text for peak labeling. **(b)** Further enlargement of the excitonic region, for sample temperature from 7 K to 130 K; the arrows indicate the position of the peaks previously labeled from *1* to *6*.

Also the other assignments made in par. 3.2.b are supported by observations of the temperature dependence of the different peaks in **Fig. 3.10(a)**. Indeed, when the sample temperature increases, the peaks attributed to emission related to bound excitons, like D^0X, *TES* and their phonon replicas, rapidly quench, while the peaks attributed to *FX* phonon replicas become more evident. This is what is expected, as previously discussed, due to the decomposition of D^0X into *FX* and to the *FX*-phonon coupling stronger than D^0X. As a consequence, at high temperatures the spectra are mainly composed by *FX* emission and its phonon replicas, as evident in the PL spectra in the range 130K-230K.

Further increasing the temperature, the peak broadening increases so that the emission results in a very broad and unstructured spectrum made by the overlapping of the different peaks.

The further enlargement of the excitonic range in **Fig. 3.10(b)** clearly shows how the relative weights of the first transitions change upon increasing the temperature: the FX_A emission (peak *1*) tends to overcome the other two emission peaks on its left side (peaks *2* and *3*), the *TES* and D^0X-*1LO* transitions (peaks *4* and *6* respectively) quickly quench while the *FX-1TO* emission (peak *5*) becomes more evident. Moreover the red-shift of the peaks is well evident in the figure.

All the discussion above permitted to deduce significant information about the deposited samples from a qualitative point of view. In order to gain some quantitative results, a further analysis on the excitonic region was conducted by a multi-gaussian fit for each spectrum of the investigated temperatures.

Due to the high complexity of the excitonic emission, since many different transitions contribute to the PL spectrum and overlap one each other, a limited range around the main emission peak was selected for this analysis: from 3.30 eV (~ 375.7 nm) to 3.42 eV (~ 362.5 nm). As seen in **Fig. 3.10(b)**, six transitions are clearly visible in this range, but in addition it must be taken into account that also other transitions contribute to the emission in this range: indeed, as seen in par. 1.2.a, up to 12 transitions were observed for the bound exciton recombinations; these transitions are not individually resolvable in the spectra presented here since they are far closer than the minimum spectral resolution of the experimental set-up used for these measurements. As a consequence, six gaussians were used to fit the PL spectrum in this range, numbered from *1* to *6* from the right (higher energy) to the left (lower energy) side of the spectrum: in a first approximation, the first three gaussians may be considered as related to the FX_A , I_2 (or *SX*) and D^0X(I_4) transitions respectively, while the other three gaussians may account for emission coming from other bound exciton transitions, *TES*, FX_A–*1TO*, D^0X–*1LO* and tails of other phonon replicas centered at slightly higher energies. However it must be underlined that, due the high complexity of this spectral range, other transitions may also influence the first three gaussians.

As qualitatively discussed above, it is expected that not all the six gaussians stand from low temperature to room temperature, since many transitions rapidly quench with the increasing temperature. Indeed only the first and the last gaussians survive until room temperature, as expected since they are mainly related to free exciton emission and phonon replicas. The areas of gaussians *2* and *5* go to zero for sample temperature higher than 190 K, the gaussian *4* stands till 210 K, and the third one (related to the $D^0X(I_4)$ emission) completely vanishes above 230 K. In order to give a more clear idea, in **Fig. 3.11** some of the performed fits are shown as examples.

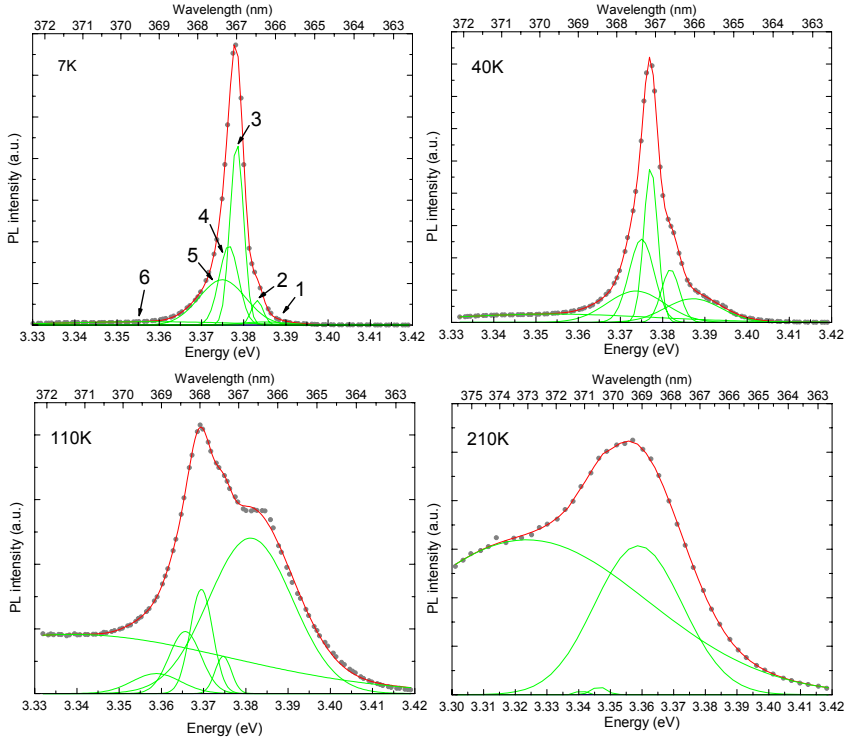

Fig. 3.11. Multi-gaussian fit with six gaussians (green lines) on four PL spectra (gray dots) of sample A600_1 at different temperatures. The red lines are the resulting fits.

At 7 K the main emission is given by the gaussian *3* ($D^0X(I_4)$) while the first (FX_A) and last (related mainly to phonon replicas and other underlying transitions not considered by the other gaussians) are very weak. At 40 K it can be seen that the gaussian *1* has a greater influence on the overall spectrum in comparison with the 7K spectrum, thus indicating

that dissociation from bound to free exciton has taken place. Further increasing the temperature (110 K) this effect becomes more important so that the FX_A emission (gaussian *1*) overcomes the other transitions; also the last gaussian, being related to phonon replicas, becomes more evident. At further higher temperatures (210 K) the emission in the considered range is given almost completely by the first and last gaussians, while the others disappear.

By investigating the temperature-dependent shift of the central energies of the gaussians obtained by the fitting procedure, it can be seen that all the six peaks show the same Varshni-like behavior. For clarity in **Fig. 3.12** the central energies and the fitting curves by the Varshni equation (**Eq. 3.1**) are reported only for the most significant transitions, which are the first three gaussians, related to the FX_A , I_2 (or SX) and $D^0X(I_4)$ emissions respectively.

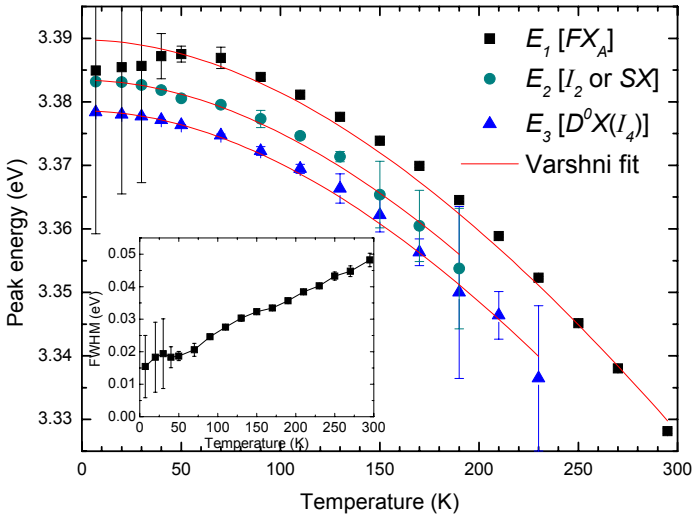

Fig. 3.12. Varshni fit of the central energy peaks of the first three gaussian obtained from the multi-gaussian fit; the red lines are the fitting curves. Inset: FWHM of the first gaussian obtained from the multi-gaussian fit.

It should be noticed that the quite high uncertainties on the first data points of gaussian *1* are due to the fact that at those temperatures the main contribution to the fit is given by the other gaussians, while gaussian *1* has a low influence in the fit, thus resulting

in high fitting uncertainties; for the same reason, high error bars are observable in the last data points of gaussians *2* and *3*, since they are going to vanish at such temperatures. Due to the rather high error bars on the first three data points of the first central energy, it is not certain that the slight descent under 40 K is a real feature related to the sample emission, since it can be related just to the high fitting uncertainties on those data. By fitting the data with the Varshni equation the values of α=0.8±0.2 meV/K and β=860±300 K are obtained. Though the uncertainties obtained from the Varshni fit on the α and β values are quite high, it can be observed that these values are in good agreement with values reported in literature for ZnO nanostructures, films and bulk material (α usually in the range ~ 0.4 – 1 meV/K, β usually in the range 700-1000 K) [87, 93, 161 – 165]. It should be observed that, as already previously stated, no quantization effects or significant differences with the ZnO bulk behavior are expected due to the very small Bohr radius of the exciton in ZnO. Using the values of the central energies at T=0 K obtained for the three considered transitions by the Varshi fit and assuming that the first transition is related to the FX_A recombination, it is possible to get the localization energies of transitions *2* and *3*, defined as the difference between the energy of the FX_A emission and the energy of the considered gaussian:

$$E_{loc}^{G2} = E_1(T=0K) - E_2(T=0K) = [(3.3897 \pm 0.0007) - (3.3834 \pm 0.0007)]\,\text{eV} = 6 \pm 1\,\text{meV}$$

$$E_{loc}^{G3} = E_1(T=0K) - E_3(T=0K) = [(3.3897 \pm 0.0007) - (3.3786 \pm 0.0008)]\,\text{eV} = 11 \pm 2\,\text{meV}.$$

The localization energy of the third transition is very close to the value ~ 13 meV reported in literature (see e.g. **Tab. 1.3**) for the localization energy of the transition I_4, attributed to a neutral donor bound exciton emission. This observation supports the assignment of peak *3* to the $D^0X(I_4)$ emission. About transition *2*, uncertainty remains: indeed the localization energy ~ 6 meV extracted from the values obtained by the Varshni fit places between the localization energies reported for lines I_1 (~ 4 meV, attributed to a neutral donor bound exciton recombination) and I_2 (~ 8.5 meV, attributed to a ionized donor bound exciton) (see **Tab. 1.3**). However the assignation of transition *2* to I_1 line is unlikely since this transition is rarely observed in literature. On the other hand, also assignment to line I_2 is not certain and the possibility that such transition comes from

surface exciton emission still remains, since, as told before, in literature *SX* emission was reported approximately at this energy position for many nanostructured samples.

The inset of **Fig. 3.12** reports the full width at half maximum (FWHM) obtained for the first gaussian in the multi-gaussian fit; the other gaussians are not shown for more clarity of the graph. It can be seen that, as previously stated, the gaussian broadens continuously when increasing the sample temperature, as expected due to the increasing exciton-phonon scattering.

By investigating the temperature dependence of the gaussian areas obtained from the multi-gaussian fit, it can be observed that for none of the six transitions it is possible to describe the temperature behavior by an Arrhenius fit using only one thermally activated process. For all the gaussians from *2* to *6*, at least two thermally activated processes are required to fit the data-sets; about the first gaussian, a specific discussion is needed (see below). In **Fig. 3.13** the gaussian areas obtained from the multi-gaussian fit are plotted in a semi-Log scale versus the inverse of the sample temperature.

As observable from the figure, the area of the first transition has a different behavior compared with the other peaks: increasing the temperature a slight increase in the gaussian area appears around 20-30 K, then the area starts to decrease and from around 70 K to room temperature the usual quenching of the PL emission is observed. This rise in the FX_A emission area has been observed in several studies of the ZnO PL properties. For example in ref. [76] the FX_A emission has been observed to increase up to 40 K and then to decrease as the temperature was further increased; in ref. [154] this increase has been observed up to 25 K before the decrease started, and the authors ascribed this observation to the decomposition of bound excitons to free excitons due to the increased thermal energy. The same increase, up to 30 K, observed in **Fig. 3.13** induces to strongly strengthen the previously-made assignment of the first observed PL peak to the FX_A emission. It should be underlined that dissociation to free excitons may happen from different bound excitons, since several transitions related to different bound excitons are present in the excitonic range, and possibly also from surface excitons.

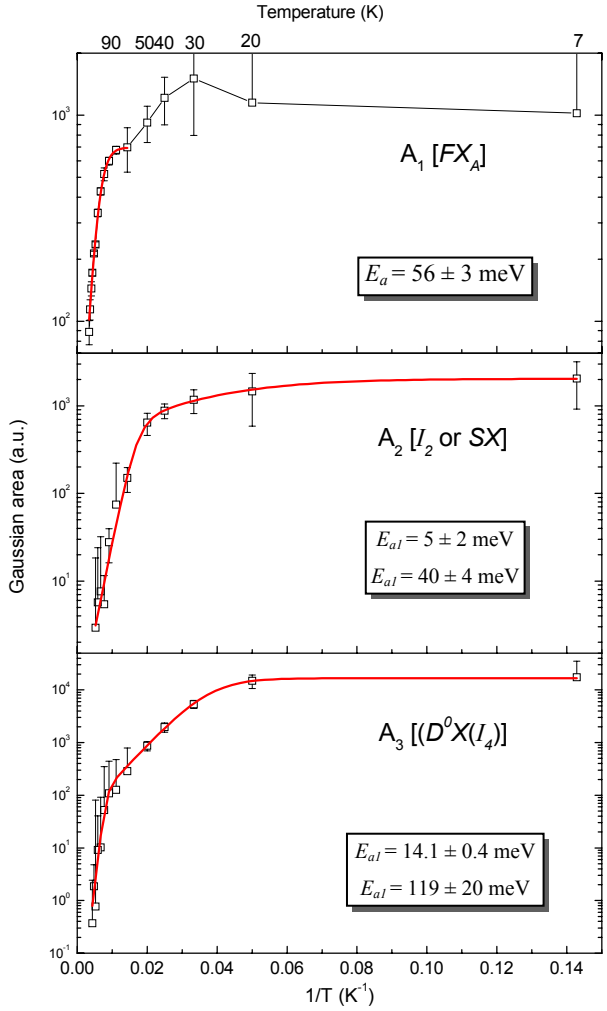

Fig. 3.13. Areas of the first three gaussians obtained by the multi-gaussian fit plotted in semi-Log scale versus the inverse of temperature. The red lines are the fitting curves as described in the text; the values of the activation energies obtained from the fit are reported inside each graph.

In order to gain more information on the temperature decreasing of the area of the first peak, for this gaussian an Arrhenius fit with a single thermally activated process (**Eq. 3.2**) has been performed in the range where the usual PL decreasing is observed: from 70 K to RT. The fitting curve is the red line in the first graph of **Fig. 3.13**. An activation energy of 56±3 meV is obtained from the fit. This activation energy is very close to the ZnO exciton binding energy (59 meV), thus suggesting that the process leading to the PL quenching for the considered transition is the thermal dissociation of the exciton into a

free electron and a free hole. The very closeness of the obtained activation energy to the exciton binding energy is another further indication to assign the first observed transition to the free exciton FX_A emission.

Dealing with the other two considered transitions, as stated before, a single thermally activated process is not adequate to well describe their temperature behavior, while the use of two activation processes can well describe the PL emission decrease of these transitions. A possible explanation for these two thermally activated mechanisms is that one of them is the dissociation of the considered bound exciton to free exciton, while the other can be the usual PL decreasing when temperature increases due, for example, to charge-carrier trapping in non-radiative centers or to scattering with phonons. As a consequence an Arrhenius fit with two processes (**Eq. 3.3**) has been used for these transitions (second and third graphs in **Fig. 3.13**). By this fitting procedure the two obtained activation energies are $E_{a1}^{A2} = 5 \pm 2\,\text{meV}$ and $E_{a2}^{A2} = 40 \pm 4\,\text{meV}$ for transition *2*, and $E_{a1}^{A3} = 14.1 \pm 0.4\,\text{meV}$ and $E_{a2}^{A3} = 119 \pm 20\,\text{meV}$ for transition *3*. It can be noticed that the activation energy of the first process for both transitions is very close to their localization energy: as estimated from the values obtained by the Varshni fit, the localization energies of transitions *2* and *3* were 6±1 meV and 11±2 meV respectively. This observation is in great agreement with the hypothesis that one of the activated processes is the dissociation of the considered bound exciton to free exciton. Discussing about the activation energy of the second thermally activated process of transition *3*, if it is supposed that this second mechanism is due only to scattering with phonons causing the separation of the exciton in a free electron and a free hole, then it is expected that its activation energy is close to the binding energy of the considered exciton. As seen in **Tab. 1.3**, the binding energy of line I_4 is ~ 46 meV, while the second activation energy obtained from the Arrhenius fit on transition *3* is higher; moreover this activation energy is higher than the reported binding energies of all the transitions reported in **Tab. 1.3**. This difference may be attributed to different possible reasons:

- first of all, apart of exciton separation due to phonon scattering, other non-radiative mechanisms, such e.g. trapping of charge-carriers in defect states, can

contribute to the quenching of the emission, thus leading to the high activation energy obtained from the fit.

- as already mentioned, the excitonic region is very complex, since many transitions can happen and overlap in this range, therefore all these transitions may influence the values obtained from the fit. Even more, the higher activation energy is related to a mechanism happening at higher temperatures, where the overlap among different transitions is more important since they are broader; thus it is possible that this activation energy is more influenced by this factor, while the lower activation energy is less influenced since related to a mechanism happening at lower temperatures where the different transitions are more separated one each other.
- finally, it should be observed that at higher temperatures the higher overlapping of the different transitions and the lower emission intensities lead to higher uncertainties on the data points obtained from the multi-gaussian fit at these temperatures, as clearly observable in the last graph of **Fig. 3.13**. As a consequence, the activation energy value obtained from the fitting procedure for the mechanism happening at higher temperatures can be influenced by these higher fitting uncertainties.

The activation energy of the second process of transition *2* (~ 40 meV) is lower than the binding energies reported in **Tab. 1.3**. In literature [93, 95] it has been reported that transitions attributed to surface excitons have a lower activation energy and vanish faster with respect to the other bound exciton transitions. As previously told, in the multi-gaussian fit the gaussian of transition *2* is the first one whose area goes to zero. This observation, together with the lower activation energy obtained by the fit, may lead to assign transition *2* to emission coming from recombination of excitons bound to surface states. However the uncertainty about this assignment still stands, since no binding energy value is reported for line I_2 in **Tab. 1.3**, thus it cannot be completely excluded that transition *2* is related to the I_2 donor bound transition.

Chapter 4
Optical sensing

Chapter 4 - Overview

This chapter presents the preliminary gas sensing investigations based on photoluminescence measurements performed on some deposited samples.

The first paragraph is an introduction about gas and biological sensing and about some different transduction mechanisms usable for such application. In addition some examples of chemical and biological sensing by using zinc oxide as bulk material or film are shown.

In the second paragraph the attention is focused on ZnO nanostructures and several examples of different tested species and different used transduction mechanisms, exploiting ZnO nanostructures, are listed.

In the last paragraph the measurements for the optical sensing investigations performed on some deposited samples are presented for the detection of nitrogen dioxide (NO_2), employing an experimental set-up arranged during this research activity . These measurements are based on the quenching of the photoluminescence intensity due to adsorption of nitrogen dioxide on the sample surface. Concentrations down to 3 ppm of NO_2 in dry air are detected by using a nanostructured sample with a high surface-to-volume ratio and high total available surface for gas molecule adsorption. However some observations about a probable incomplete reversibility of NO_2 adsorption are noticed. Some comparisons when using two different gas flows (50 ml/min or 100 ml/min) are also shown.

4.1 Zinc oxide for gas and biological sensing applications

In the introduction of this Thesis and in the first chapter the great interest of zinc oxide for chemical and biological sensing applications has been mentioned.

Metal oxide semiconductors are very promising materials for chemical and biological sensors due to their chemical stability, low cost, low power consumption and high compatibility with microelectronic processing [50]. In addition, ZnO biocompatibility is a very appealing property for biological sensing in biomedical applications.

When gas molecules or biological species interact with the surface complexes (O^-, O_2^-, H^+, OH^-) of the active material* of the sensor, they induce a change in some physical properties of the material, such as the charge-carrier density which thus causes variations in the electrical conductance or optical emission. By measuring these variations it is possible to detect the presence and the amount of the species to be revealed. Moreover the chemisorption of reactive gases on the surface of metal oxide materials is usually reversible, allowing long lifetimes of the sensor.

Because of the changes induced in different physical properties of the active material, several different transduction mechanisms can be exploited in order to reveal the presence of chemical or biological species in the environment surrounding the material. As a consequence, different kinds of sensors can be realized. Some examples of transduction mechanisms usable for sensing applications are reported below.

* The active material is intended as the material whose changes in some physical properties are measured in order to reveal the presence of the species to be detected.

4.1.a Resistive sensors

One of the most used kind of sensors is based on an electrical transduction mechanism, that is the measure of the changes of the electrical conductivity of the sensing material when the detectable species interact with its surface: when the molecules bind to the surface of the active material, they can cause a rise or a fall in its resistance whether they take or release a charge-carrier in the active material respectively.

For example, when a molecule of an oxidizing gas (like NO or NO_2) binds to the surface of an n-type semiconductor, it acts as an electron trapper thus reducing the conductivity of the sensor; typical reactions are:

$$O_{2\,(gas)} + e^- \rightarrow O^-_{2\,(adsorbed)} \qquad \textbf{Eq. 4.1}$$

$$NO_{(gas)} + e^- \rightarrow NO^-_{(adsorbed)} \qquad \textbf{Eq. 4.2}$$

Oxygen can be adsorbed on the surface as O_2^- (like in **Eq. 4.1**), O^- or O^{2-} ions.

On the contrary, when a molecule of a reducing gas (like CH_4, CO or H_2) binds to the surface the n-type active material, it causes an increase of the sensor conductivity due to the addition of an electron into the conduction band. For example, for adsorption of a CO molecule:

$$CO_{(gas)} \rightarrow CO^+_{(adsorbed)} + e^- \qquad \textbf{Eq. 4.3}$$

Anyway it must be taken into account that the mechanisms taking place on the surface of the active material are not so simple, since a lot of different adsorption and desorption processes may happen during the sensing measurements. Indeed a gaseous molecule can react also with a molecule of another gas previously adsorbed on the surface of the active material and not with the surface states of the material itself. Thus, when a reducing molecule interacts with the surface of the active material, the increase of the electrical conductivity can be caused by another possible mechanism, different from that

one illustrated in the example of **Eq. 4.3**: the incoming molecule may react with an adsorbed oxygen ion, causing its desorption and the consequent release of an electron. For example an incoming CO molecule can react with an adsorbed oxygen ion to form a CO_2 molecule which can be desorbed from the surface [166]. Other similar reactions may happen between reducing gases and adsorbed oxygen; for example, at 150°C the following reaction with hydrogen can happen [167]:

$$2H_{2(gas)} + O^-_{2(adsorbed)} \rightarrow 2H_2O_{(gas)} + e^- \qquad \textbf{Eq. 4.4}$$

Furthermore, another possible process is the desorption of previously adsorbed molecules, caused by other incoming molecules onto the surface as a consequence only of the flux, without any chemical reaction happening.

Sensors based on this electrical transduction mechanism, exploiting the changes in conductance of the active material, are generally called resistive sensors. For these sensors the measurements are usually conducted by applying a given voltage to the active material and measuring the changes of the current (and thus resistance) flowing through it when it is exposed to air or to the detectable species. In this case the *response* (or *sensitivity*) S of the sensor for a given concentration of the species of interest can be defined as the variation of the sensor resistance with respect to its resistance in air:

$$S = \frac{\Delta R}{R_a} = \frac{\left|R_a - R_g\right|}{R_a} \qquad \textbf{Eq. 4.5}$$

where R_a is the sensor resistance in air and R_g is the sensor resistance in the presence of the species to be revealed. Sometimes the variation of the resistance is normalized to the sensor resistance in the species to be detected instead of that one in air (R_g instead of R_a in the denominator of **Eq. 4.5**). Other times the sensor response is simply defined as the ratio between the sensor resistance in air and in the presence of the species of interest, that is:

$$S = \frac{R_g}{R_a} \quad \text{or} \quad S = \frac{R_a}{R_g} \qquad \textbf{Eq. 4.6}$$

whether the active material is an n-type semiconductor in an oxidizing or reducing ambient respectively (in the first situation $R_g > R_a$, while in the latter $R_g < R_a$). As clearly observable from the definitions above, the sensitivity value is not an absolute parameter describing the quality of the sensor, since it depends on the concentration at which it is measured; thus the sensitivity values are relative to the used concentrations.

Two additional useful parameters for sensor characterization, other than sensitivity, are *response time*, defined as the time needed to reach a given response percentage (usually about 90%) of the saturation response when the sensor is exposed to a given concentration of the species to be revealed, and *recovery time*, defined as the time to reach the same percentage of the recovered response when the sensor is exposed to air again. So these parameters show how the sensor is fast in the detection of the gas and recovery in air. Also these parameters, like the sensitivity, are relative to the concentration at which they are measured.

Often the resistive sensors are heated (up to ~ 350-400°C or even more) during the measurements because usually higher temperatures promote chemisorption processes and desorption dynamics, thus improving the sensor performances. Thanks to its wide band-gap, ZnO-based resistive sensors can operate at higher temperature than other conventional semiconductors like silicon, hence allowing the enhancement of the sensor performances.

4.1.b Photoluminescence-based sensors

Another possible transduction mechanism is based on the changes in the luminescence intensity of the active material when it is exposed to the detectable species. As described above, when a molecule binds to the surface of the material, there is an exchange of charges between the adsorbed molecule and the active material, thus possibly

changing the number of electrons and holes radiatively recombining and consequently changing the luminescence intensity. For example, since an oxidizing gas acts as an electron trapper, usually it causes a reduction of the number of charge-carriers radiatively recombining, with a consequent decrease (*quenching*) of the luminescence intensity.

For this kind of sensors the measurements can be performed by exciting the active material through a light source (like a lamp, a LED or a LASER) and collecting the optical radiation emitted by the material. By measuring the changes of the photoluminescence (PL) intensity at a given wavelength or the integral of the luminescence in a range of wavelengths when the sensor is exposed to the detectable species or in air, it is possible to detect the presence of the species. PL-based sensors may have some advantages over electrical sensors, since they can show high responses without requiring high working temperatures (thus also being suitable for sensing of explosive gases) and they have been demonstrated to be stable, reproducible, reversible, with rapid response and good sensitivity [168, 169]. But, on the other hand, usually this kind of sensors are considered hardly realizable in a cheap way and in a compact structure, since they require, apart of the sensing material, at least a light source exciting the material and a photodetector measuring the luminescence intensity; moreover often optical excitation sources are bulky or require intricate integration procedures [168]. Despite these drawbacks, recently compact and simple PL-based sensors, employing organic LEDs (OLEDs) as excitation sources, have been realized for gas [170, 169] and biological sensing [171]. The typical compact structure (see **Fig. 4.1**) of these sensors is composed by an OLED, constituted by an organic layer sandwiched between a cathode and an anode (e.g. an Indium Tin Oxide transparent anode), whose electroluminescence (EL) is used to photo-excite the sensing material placed on the OLED; the photoluminescence emitted by the active layer is collected and measured by a photodetector.

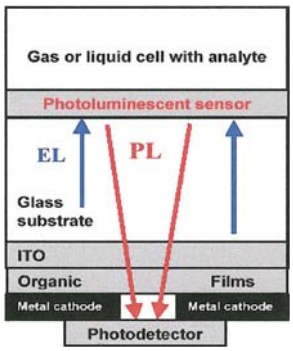

Fig. 4.1. Schematic representation of a PL-based sensor. (Image from ref. [171]).

The same parameters describing the sensor performances used for the resistive sensors (*sensitivity*, *response time* and *recovery time*) can also be used for the PL-based ones. In this case the *sensitivity*, in analogy with **Eq. 4.5**, can be defined as:

$$S = \frac{\Delta I}{I_a} = \frac{|I_a - I_g|}{I_a} \qquad \textbf{Eq. 4.7}$$

where I_a and I_g are the PL intensities at a given wavelength (or the PL integrals in a range of wavelengths) when the sensor is exposed to air or to a given concentration of the species to be detected respectively.

4.1.c Photocurrent-based sensors

A mechanism appearing as a combination of the two previous ones is based on the measurement of the photocurrent changes when the active material is exposed to air or to the detectable species. Here a light source (usually an UV lamp or LASER for ZnO-based sensors) excites the active material and the changes in the generated photocurrent are measured through the electrodes placed on the material.

4.1.d Sensors based on Schottky rectifiers or FETs

Other kinds of sensors based on electrical transduction, and very similar to the resistive ones, are sensors using Schottky rectifiers or field effect transistors (FETs).

For example, very similarly to the resistive sensors, molecule adsorption on Schottky rectifier can be revealed by detecting the variations of the current-voltage characteristics of the Schottky diode. As in resistive sensors, the molecule adsorption can be also detected by measuring the changes of the current intensity for a fixed voltage or the variations of the voltage for a fixed current flowing through the device [172].

Also sensors based on FETs with a sensitive material can be realized. In this category of sensors the changes in the conductance of the active material induce changes in the electrical response of the FET. Therefore the species of interest can be detected by measuring the changes of the source-drain current for a fixed gate voltage or the changes of the threshold voltage. Such sensors can also be used for biological applications, like pH sensing [173].

4.1.e Surface Plasmon Resonance

Another type of sensors, based on optical transduction, makes use of surface plasmon resonance (SPR) measurements [174]. Since this method can be applied for measurements with liquids, it is very interesting for biological sensing applications.

Surface plasmons are electromagnetic waves propagating along a metal/dielectric or metal/vacuum interface, whose frequency is a characteristic of the system. Adsorption of molecules on the metal (e.g. gold or silver) surface induces small changes in the dielectric constant of the metal, thus changing the plasmon frequency. This frequency can be monitored by reflectance measurements: the reflectance of the metal surface is measured in a range of frequencies close to the plasmon frequency and, when the incident beam is resonant with this frequency, a minimum in the reflectance is detected. Therefore it is possible to reveal the presence of gas molecules or biological species adsorbed on the

metal surface by measuring the shift and change in the width of the reflectance minimum with respect to that one in absence of the species of interest. To enhance the sensing response, a layer of a highly sensitive and chemical stable material, like ZnO, can be deposited on the metal surface: the proper frequency to this system is measured and the variations when molecules are adsorbed on the active material are monitored.

4.1.f Quartz Crystal Microbalance

For sensing measurements a quartz crystal microbalance (QCM) can also be used. A QCM is based on the piezoelectric properties of a quartz crystal: an alternating current applied to a properly cut crystal induces the generation of shear horizontal surface acoustic waves (SH-SAW), whose frequency is proper to the system. When a small mass is added to the crystal surface, the frequency of the resonator changes; QCM may be sensitive to mass changes ~ ng/cm^2 [175]. For sensing measurements a highly sensitive and chemically stable active layer, like ZnO, can be deposited onto the quartz microbalance and the proper frequency of this device can be measured; in this way, when gas or biological species bind on the active layer, the frequency of the device changes due to variations of both mass and conductivity of the device.

4.1.g Cyclic Voltammetry

Another mechanism, based on electrical transduction, but suitable for biological sensing since it works in solution, operates by cyclic voltammetry measurements. Here an electrode (e.g. a gold electrode) with the sensing material is in contact with the solution containing the species of interest. The current flowing through the electrode is plotted versus the applied voltage, thus giving the so called cyclic voltammogram. By comparison with the voltammogram of a reference electrode in a solution without the species of interest, it is possible to reveal the presence of the species.

4.1.h Other information and some examples

Often, in order to improve the sensor performances, active materials are used together with other materials, usually metals, acting as catalysts for adsorption. It is well known that adding catalysts (such as Au, Pt, Pd, Sn, etc.) promotes chemical reactions on the surface of the active material by reducing the activation energies for adsorption of molecules without consuming of the catalyst itself. This allows having reactions at faster rates and lower concentration of the detectable species [176].

ZnO sensing properties have been tested, as bulk and thick or thin films, on several gases and biological species. In **Tab. 4.1** few examples of species detected by using bulk ZnO or films as active material are listed, together with the relative transduction mechanism used, the form of ZnO (bulk or film), catalysts (if used), and minimum tested concentration.

Gas or biological species	Transduction mechanism	ZnO form	Catalyst	Minimum concentration	Ref.
CO	resistive	bulk single crystal	/	20 ppm	[177]
NH_3	resistive	thin film(0.3µm)	without and with Al, In, Ga	2 ppm	[178]
H_2	resistive	thin film(20-350nm)	Pt-coated	500 ppm	[179]
H_2	resistive	thin film(0.3-1µm)	/	2000 ppm	[180]
H_2	resistive	thin film(0.5-5µm)	/	30000 ppm	[167]
LPG (*)	resistive	thin film(0.5-5µm)	/	4000 ppm	[167]
CO	Schottky contact	bulk	Pt-contact	10000 ppm	[172]
pH	FET	thick film(32µm)	/	2-12 (**)	[173]

Tab. 4.1. Some examples of sensing tests by using ZnO as active material. (*) LPG = liquid petroleum gas. (**) Range of pH values for which the sensor has been tested.

Additionally, it must be taken into account that an ideal sensor, besides having high sensitivity, fast response and high stability, must also be able to discriminate between different gases. For this purpose arrays containing different metal oxides (like SnO_2, ZnO, WO_3, CuO, In_2O_3) on the same device can be used [181].

4.2 Zinc oxide nanostructures for gas and biological sensing applications

As seen in the previous paragraph zinc oxide is very interesting for applications in chemical and biological sensing. Moreover, for the reasons explained in par. 1.1, this interest is highly increased when dealing with ZnO nanostructures.

Indeed a large number of different gases, vapors and biomolecules have been tested by using ZnO nanostructures as sensing elements and by means of several transduction mechanisms. Some transduction mechanisms employed for sensing applications, together with a brief explanation of the working principle for each mechanism, have been reported in the previous paragraph.

To give an idea of the great number of species tested for sensing applications with ZnO nanostructures, **Tab. 4.2** shows a list of several different substances tested in literature, grouped by the employed measurement method. In the table the minimum concentration used for the sensing measurements is reported. It should be noticed that it is hard to make a comparison of the sensitivity values among the different literature sources, since different sensitivity definitions are used (some sensitivity definitions are reported in par. 4.1.a) and the sensitivity is measured at different concentrations.

Gas or biological species	Nanostructures	Catalyst	Minimum concentration	Ref.
		Resistive		
Hydrogen (H_2)	rods	/	10 ppm	[182]
	rods	/	50 ppm	[183]
	nanostructures	1% Pt	10 ppm	[184]
	nanoparticle film	3%Co, 1%Pt, 1%Pt+3%Co	10 ppm	[185]
	wires	Pd	< 10 ppm	[186]
	wires	Pt, Pd, Au, Ag, Ti, Ni	100 ppm	[187]
	rods	/	20 ppm	[188]
	rods/belts	/	250 ppm	[189]
Ammonia (NH_3)	rods	/	100 ppm	[183]
	rods	/	200 ppm	[188]
	nanoparticles, rods	/	1 ppm	[190]
	rods	PdO	50 ppm	[191]
Carbon monoxide (CO)	rods	/	200 ppm	[188]
	wires	/	100 ppm	[192]
	rods	PdO	500 ppm	[191]
Nitrogen dioxide (NO_2)	wires	/	5 ppm	[192]
Hydrogen sulfide (H_2S)	rods	PdO	2 ppm	[191]
	rods	/	0.05 ppm	[193]
	rods	/	0.01 ppm	[194]
Ozone (O_3)	wires	/	0.05 ppm	[195]
Ethanol (C_2H_6O)	rods	/	10 ppm	[182]
	rods	/	1 ppm	[183]
	nanostructures	1% Pt	1000 ppm	[184]
	wires	/	100 ppm	[192]
	rods	PdO	10 ppm	[191]
	nanoparticles	Pd	100 ppm	[196]
	flower-like	/	10 ppm	[197]
	multipods	/	1000 ppm	[198]
	wires	/	50 ppm	[199]
	rods	/	1 ppm	[200]
	wires	/	1 ppm	[201]
	rods	/	1 ppm	[193]
	tetrapods	/	50 ppm	[202]
	nanostructures	/	12.5 ppm	[203]
	nanotubes	/	1 ppm	[204]
Acetone (C_3H_6O)	wires	/	10 ppm	[192]

Benzene (C_6H_6)	rods	/	0.01 ppm	[200]
Liquid Petroleum Gas (LPG)	rods	PdO	500 ppm	[191]
	nanoparticles	Pd	100 ppm	[196]
	rods	/	2000 ppm	[205]
Gasoline	rods	PdO	50 ppm	[191]
pH	single nanorod	/	2-12 (*)	[206]
FET				
Nitrogen dioxide (NO_2)	wires	/	0.2 ppm	[207]
Ammonia (NH_3)	wires	/	0.5%	[207]
Oxygen (O_2)	wires	/	10 ppm	[208]
Photoluminescence				
Nitrogen dioxide (NO_2)	belts	/	5 ppm	[209]
	wires	/	12 ppm	[195]
Photocurrent				
Oxygen (O_2)	wires	/	~ 80 Pa (**)	[210]
Water vapor (H_2O)	wires	/	~ 390 Pa (**)	[210]
Surface Plasmon Resonance				
Ethanol (C_2H_6O)	nanostructured film	/	1560 ppm	[211]
Isopropanol (C_3H_8O)	nanostructured film	/	1782 ppm	[211]
Quartz Crystal Microbalance				
Ammonia (NH_3)	wires	/	40 ppm	[212]
Humidity (H_2O)	rods, wires	/	5-97%	[175]
Cyclic Voltammetry				
Glucose oxidase (GOx)	combs	/	0.02 mM	[213]
	rods	/	0.01 mM	[214]
Uric acid	rods	/	0.002 mM	[215]

Tab. 4.2. Different species tested for sensing measurements by using ZnO nanostructures. (*) Range of pH values for which the sensor has been tested. (**) Partial pressure of the gas of interest inside the measurement chamber.

4.3 Optical sensing with the deposited samples

In this paragraph the optical sensing tests performed during the research activity presented in this Thesis are shown. These sensing measurements are based on the variation of the photoluminescence emission due to gas adsorption (as explained in par. 4.1.b) on the deposited samples. Since in literature [195, 209] zinc oxide nanostructures have been reported to be able to detect nitrogen dioxide (NO_2) by measurements of the photoluminescence quenching, this gas has been chosen to test our samples for the optical sensing. As told in pars. 4.1.a and 4.1.b, molecules of oxidizing gases, like NO or NO_2, act as electron trappers, thus causing the decrease of charge-carriers which recombine radiatively, and consequently quenching the PL intensity. In particular it is believed that the mechanism responsible for the PL quenching with NO_2 is that on the nanostructure surface NO_2 molecules dissociate into NO, which acts as en electron trapper following the reaction reported in **Eq. 4.2** [209].

4.3.a Experimental set-up

The light source used for the optical excitation of the samples was the same He-Cd laser used for the photoluminescence measurements reported in par. 3.2. The laser beam was collected by an UV optical fiber (400 µm, Avantes FC-UV400-2) equipped with a collimating lens on its head and with an optical fiber splitter, in order to split the laser beam in two paths: a branch of the split fiber was sent to a silicon photodiode (properly shielded from the light of the outside environment) connected with a pico-ammeter interfaced with a personal computer, in order to measure the fluctuations of the laser power during the sensing measurements; the second branch was used to direct the laser onto the sample. The sample was placed inside an aluminum sealed chamber where it was exposed to the detectable gas or to dry air. The chamber was provided with four

apertures: two apertures were used for gas inlet and outlet respectively, the others were connected with the excitation optical fiber and with the collection optical fiber (**Fig. 4.2**).

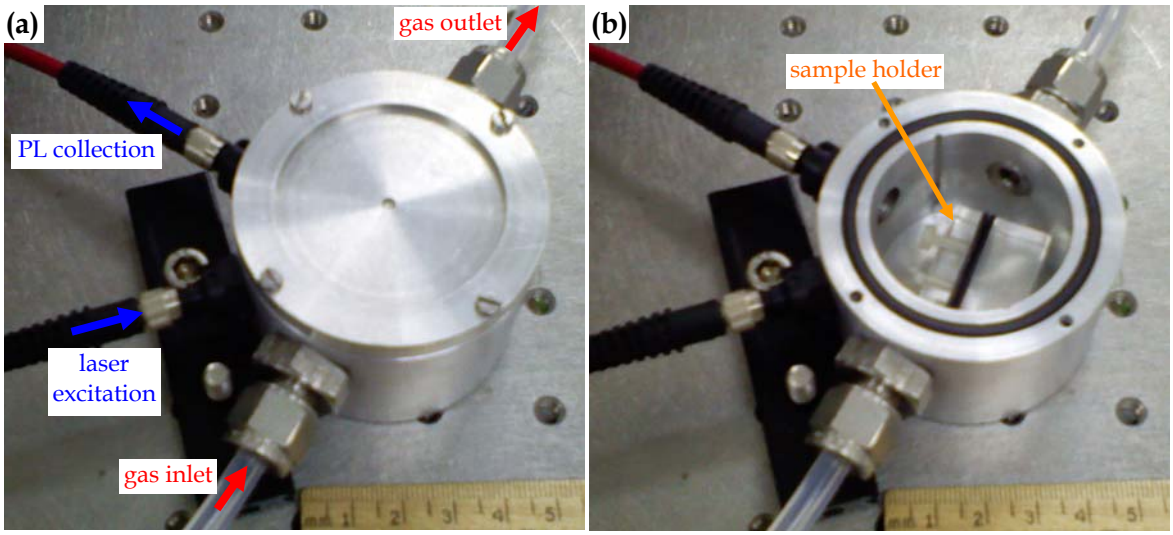

Fig. 4.2. Photo of the **(a)** closed and **(b)** open chamber containing the sample for the optical gas sensing measurements.

The PL emission of the sample collected through the optical fiber was sent to a spectrometer (Avantes MC2000) with: Czerny-Turner configuration, 75 mm focal length, 600 lines/mm grating, 200 µm slit, CCD linear array detector with 2048 pixels. The spectrometer operated in the range 200-850 nm, with a spectral resolution of 4.1 nm. It should be noticed that a high spectral resolution was not required in this kind of measurements, since the integrated luminescence in a wide spectral range was used for the optical sensing measurements. The software (Avantes SpectraWin 5) used to analyze the sample luminescence during the sensing measurements allowed to periodically acquire the integral under the PL spectrum in a fixed wavelength range at fixed time intervals.

The gas inlet was controlled by a bank of three mass flow controllers (Brooks Instrument 5850S). Each controller could operate in the flow range of ~2.5-50 ml/min with an accuracy of ±0.2%. The desired gas concentration in the chamber could be obtained by mixing different flows of dry air and of the gas to be detected (NO_2) through suitable

combinations of the flows of two or three controllers (see later). The bank was controlled through a personal computer allowing to automatically set the flux flowing from each controller for fixed time intervals.

The gas used for the sensing tests was a mixture of 114.2 ppm of NO_2 in dry air. In order to obtain lower NO_2 concentrations in the chamber, this mixture was mixed with dry air by setting the proper flows giving the chosen concentration: for example, by mixing 10 ml/min of the mixture from a controller with 40 ml/min of dry air from another controller, a concentration of ~ 23 ppm of NO_2 in dry air was obtained.

4.3.b Sensing measurements

For simplicity, in the following discussion it will be written in brief that the sample is exposed to NO_2 , meaning that it is exposed to a mixture of NO_2 and dry air. Moreover, a single step made by one exposure to a given NO_2 concentration followed by one recovery in dry air will be called as a single "ON/OFF cycle", while the complete measurement made by a sequence of ON/OFF cycles at different NO_2 concentrations will be named as a "complete cycle" or "complete measurement".

By the observation of the PL spectra of the deposited samples reported in the previous chapter, it can be seen that the suitable wavelength range to study the quenching of the luminescence is the range of the excitonic emission; the visible emission is too weak (or almost totally absent in some samples) so it is not suitable for such measurements. As a consequence, during the alternating cycles of exposure in NO_2 or in dry air, the integral of the sample emission was measured in the range 360-420 nm (~ 2.95-3.44 eV); the value of the PL integral was measured each 3 seconds. By the observation of the PL spectra before and after the sample exposure to NO_2 , it can be noticed that the only effect of this exposure is a quenching of the PL intensity, while no shift of the emission peak or change in the shape of the PL spectra are observed. As an example, **Fig. 4.3** shows the PL quenching of sample K600_100 after an exposure of 15 minutes in 114.2 ppm of NO_2.

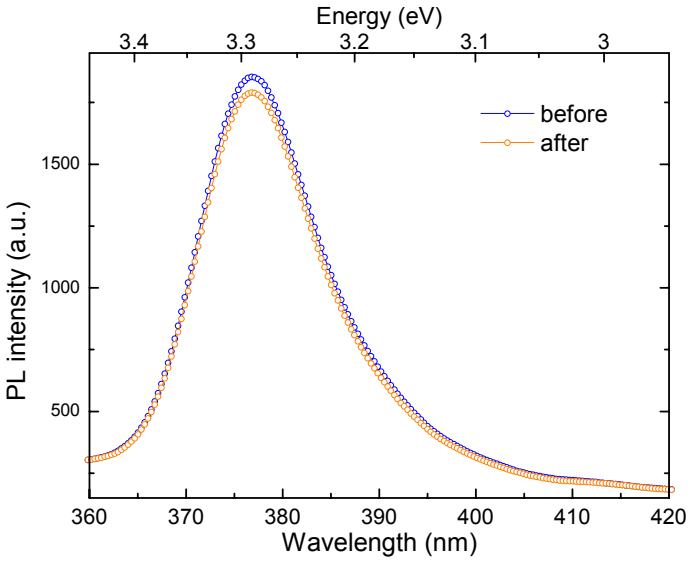

Fig. 4.3. PL spectrum in the range 360-420 nm of sample K600_100 before (blue spectrum) and after (orange spectrum) exposure for 15 minutes in 114.2 ppm of NO_2.

Since the laser power was measured during each sensing cycle, all the spectra showing the PL integral variation were normalized by the corresponding spectra of the laser power, so that the main laser fluctuations are eliminated from the sensing measurements.

For the complete sensing cycles, an interval of 5 minutes of NO_2 exposure followed by 5 minutes of recovery in dry air were chosen for each NO_2 concentration, since for the examined samples it has been seen that these times are long enough to get detectable response and recovery. In other words, each ON/OFF cycle was made by 5 minutes of exposure in NO_2 and subsequent 5 minutes of recovery in dry air.

The sensor response (sensitivity) here used is measured by the definition given in **Eq. 4.7**. The I_a and I_g here used are measured as the average values of the PL integral reached after the stabilization in air or in NO_2 respectively.

Before starting the actual complete sensing measurement, the tested sample was exposed for 15 minutes in dry air flux and two ON/OFF cycles were conducted in the lowest NO_2 concentration chosen for the test, in order to get a sample stabilization.

In **Fig. 4.4** the sensing measurements performed on five of the deposited samples are reported; the fixed total flow was of 50 ml/min and the NO_2 concentration for each ON/OFF cycle is reported above the graph. The 50 ml/min flux allows to get a good gas exchange in the chamber, but it is low enough to avoid turbulent flux and vortex formation [209]. From the figure it can be seen that each time NO_2 is introduced into the chamber (the moments at which the gas starts to flow through the mass flow controller are indicated by the dashed orange lines) the PL integral sharply decreases and, after about 2 minutes, it reaches a rather stable value; when dry air is flowed again (dashed blue lines) the integral recovers a part of the initial value.

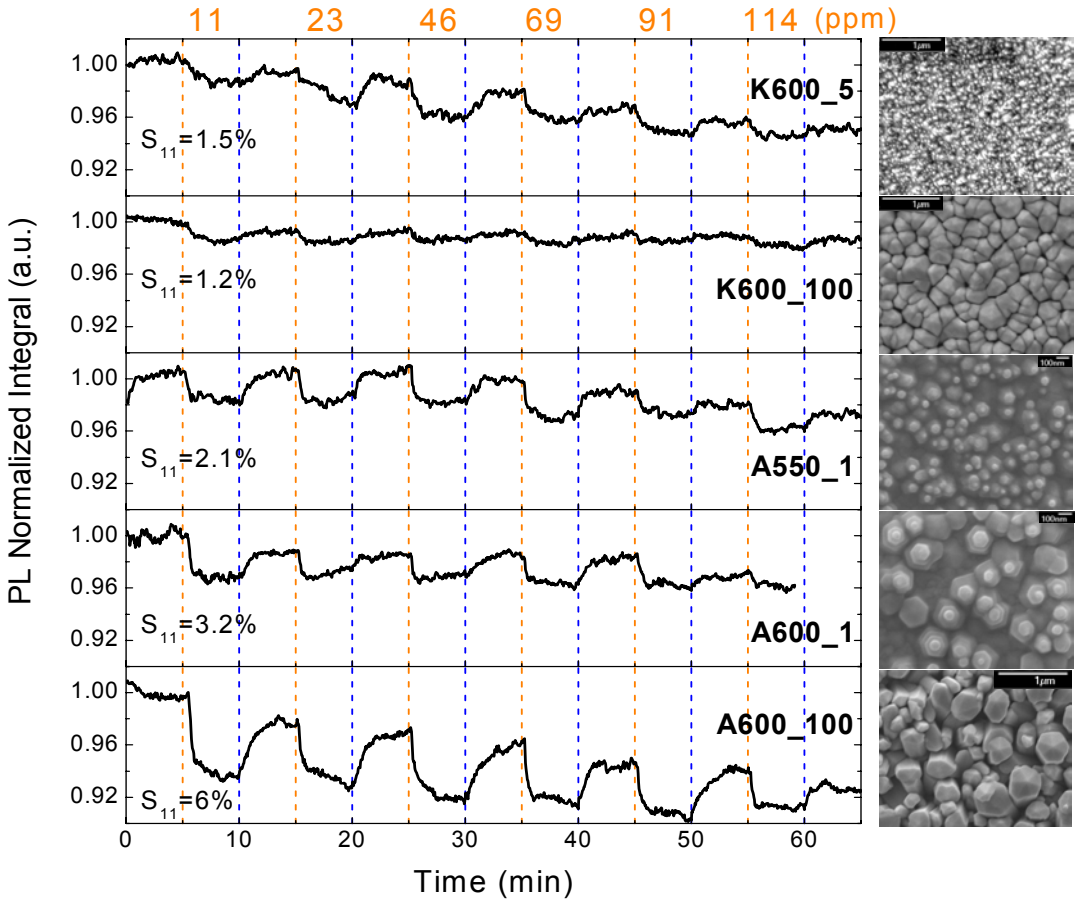

Fig. 4.4. Optical sensing measurements for some deposited samples. Dashed orange and blue lines indicate when NO_2 or dry air respectively flow through the mass flow controllers. The NO_2 concentrations for each ON/OFF cycle are reported on the top of the graph. The values S_{11} of the sensitivity measured at the lowest NO_2 concentration (11ppm) are reported inside each graph. An excerpt of the SEM image of each sample is reported beside the corresponding graph.

Several observations may be deduced from the graphs reported in **Fig. 4.4**. First of all, obviously the samples do not respond to the gas in the same manner. For example, sample K600_100 shows a very low response in comparison with the other samples (all the graphs are reported with the same vertical scale to have a comparison). The values of the sensitivity measured with **Eq. 4.7** for the first tested NO_2 concentration (11 ppm) are reported inside each graph for each sample. Looking to the SEM images reported next to the graphs, it can be noticed that the higher responses are measured for samples presenting nanostructures and a higher surface-to-volume ratio. Despite sample K600_100 is constituted by a rod array, thus having a high surface-to-volume ratio and a high total surface, its response is very low; this can be explained observing that the rods are very close one each other, thus allowing only a small fraction of the incoming molecules to bind to the surface. Also sample K600_5 has a very low sensitivity compared to the other samples, and, as observable in the graph, the measurement does not show very sharp variations of the PL integral when switching between dry air and NO_2; indeed this sample is a film with a rough surface, but no nanostructures are present. Samples A550_1 and A600_1 have a higher response, maybe thanks to the presence of the nanostructures. Among the tested samples, sample A600_100 has the highest sensitivity; observing its morphology, this occurrence is expected since the sample is made of an array of pencils well separate one each other, thus causing a very high surface-to-volume ratio and a very wide total surface available for gas molecule adsorption. Anyway it must be highlighted that the differences in sample sensitivity cannot be explained by simply referring to the morphology, since this is not the only factor heavily influencing the sensing response. Indeed the sample sensitivity may be affected by many other factors:

- the different crystal faces exposed to the external environment, and so to gas adsorption, may play an important role. Indeed, as clearly seen from the SEM images, for samples A550_1 and A600_1 the (001) crystal faces constitute the main surface where gas molecules can bind; on the contrary, for sample A600_100 almost no (001) planes are exposed to the gas, while the main exposed surfaces are the lateral faces of the hexagonal prism, corresponding to the {100} planes (or $\{10\bar{1}0\}$ in the 4-index notation, see par. 3.1), and the faces of the

hexagonal pyramid on the top of the prism, corresponding to the {101} planes ($\{10\bar{1}1\}$ in the 4-index notation). It is expected that different crystal orientations of the exposed faces may have different behaviors for adsorption of gas molecules.

- in addition to the previous point, it should be considered that also the termination of the exposed faces is a very fundamental issue in influencing gas adsorption; indeed it is expected that Zn-terminated faces act very differently from O-terminated faces in gas adsorption.
- other factors influencing the gas adsorption may be also some differences in the sample composition and stoichiometry (particularly in proximity of the surfaces), differences in crystal defects, and so on.

Another feature observable from **Fig. 4.4** is that the drop of the PL integral at the lowest used NO_2 concentration (11 ppm) is deeper than those ones at higher concentrations. It could be expected that, increasing the NO_2 concentration, the PL decreasing is higher due to the increasing number of molecules binding on the sample surface; however an opposite behavior is observed from the graphs. A possible explanation is that the 11 ppm NO_2 concentration is high enough to almost saturate the available sites for molecule adsorption and that the process of NO_2 adsorption is not fully reversible when dry air is sent again in the sample chamber to get the sample recovery. As a consequence, when the sample is exposed to higher NO_2 concentrations, the incoming molecules find fewer available adsorption sites, and thus the PL quenching is weaker.

The not full reversibility of NO_2 adsorption is also suggested by another common feature observable in **Fig. 4.4**: the overall spectrum of the sensing measurements goes down throughout all the measurement, thus indicating that maybe not all the adsorbed molecules are released during the recovery in dry air and consequently a complete recovery of the PL integral to the previous value is not allowed.

As seen from the graphs of the sensing measurements in **Fig. 4.4**, where relatively high NO_2 concentrations were tested, sample A600_100 seems to have the better response. As a consequence this sample was tested also for lower NO_2 concentrations, in order to examine the possibility to detect lower concentrations and to check whether the effects of incomplete reversibility of NO_2 adsorption are less important for lower concentrations.

Since the minimum usable flux with the employed mass flow controllers is ~ 2.5 ml/min, then the minimum NO_2 concentration reachable with the 114.2 ppm mixture keeping a total flow in the chamber of 50 ml/min is around 5 ppm. In order to further reduce the minimum NO_2 concentration, the total flow must be increased to 100 ml/min, using three mass flow controllers; in this way a minimum concentration of about 3 ppm can be obtained. The 100 ml/min flux is still very low, thus avoiding vortex formations in the measurement chamber. **Fig. 4.5** shows the sensing measurement with a total flow of 50 ml/min and NO_2 concentrations in the range 5-20 ppm, and with a total flow of 100 ml/min and NO_2 concentrations in the range 3-20 ppm. Before the measurements, the sample was heated to 50°C for 15 minutes in order to favor some desorption of previously adsorbed gas.

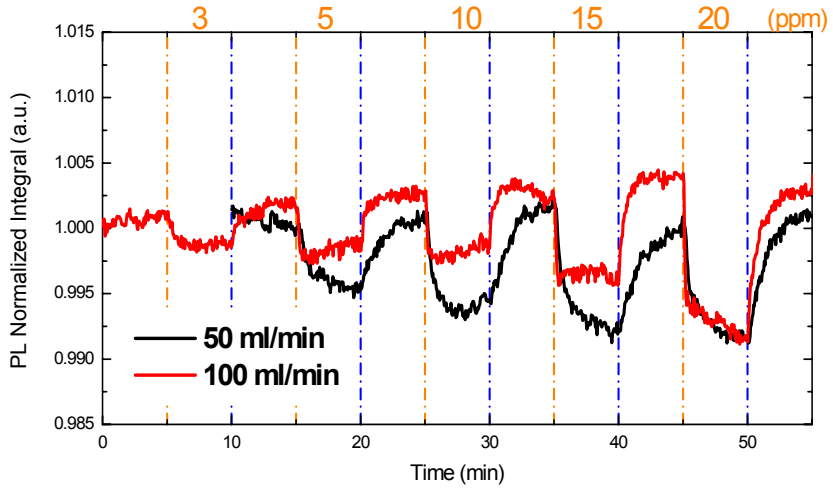

Fig. 4.5. Optical sensing measurements for sample A600_100 at total flow of 50 ml/min (black line) and 100 ml/min (red line). The tested NO_2 concentrations for each ON/OFF cycle are reported on the top of the graph

The first observation is that the sensitivity for the measurement with a total flow of 50 ml/min at 10 ppm and 15 ppm is about 0.7% and 0.9% respectively, far lower than the value of about 6% obtained at 11 ppm in the previous measurement showed in **Fig. 4.4**. In order to exclude possible evident deterioration of the sample morphology (like e.g. corrosion caused by the exposure to NO_2) causing this remarkable worsening of the

sensitivity, the sample was investigated again by SEM inspections and no differences in the morphology were observed by comparison with the previous SEM investigations. Therefore a possible hypothesis for this worsening of the sample sensitivity may be the previously suggested incomplete reversibility of the NO_2 adsorption, despite the sample heating at 50°C, thus occupying the available adsorption sites.

The sensitivity values range from ~ 0.4% at 5 ppm to ~ 0.85% at 20 ppm when a total flow of 50 ml/min is used, and from ~ 0.25% at 3 ppm to ~ 1% at 20 ppm for a total flow of 100 ml/min (see **Fig. 4.6**). Anyway, in spite of these low responses, it can be observed that the drops and rises of the PL integral when switching between NO_2 and dry air are visible and sharp also at the lowest tested NO_2 concentrations. In addition, from **Fig. 4.5** it can be noticed that for a total flow of 100 ml/min the slopes of the curve when the sample responds to NO_2 and when it recovers in air are higher than those for a total flow of 50 ml/min, indicating faster response and recovery when 100 ml/min flow is used. This behavior is expected since a higher velocity of the incoming NO_2 molecules allows a faster occupation of the available adsorption sites and thus a faster PL quenching; analogously a higher velocity of the dry air flux permits a faster unbinding of the adsorbed molecules and thus a faster recovery of the PL integral.

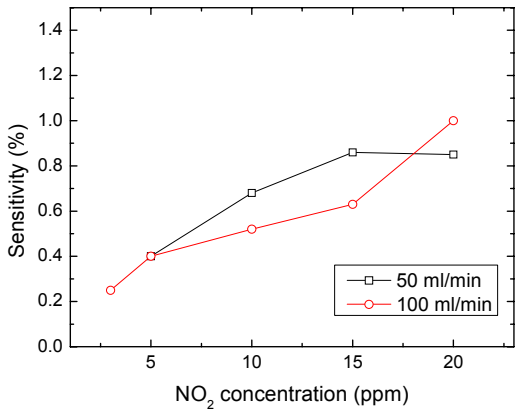

Fig. 4.6. Sensitivity values measured from Fig. 4.5 at the different tested concentrations for a total flow of 50 ml/min (black data) and 100 ml/min (red data).

It should be noticed that from **Fig. 4.6** it is hard to compare the sensitivity values for the two used total flows because these values are very close and because the measured values can be influenced by residual gas adsorbed in the previous measurements and not fully desorbed despite the sample heating. However some other noteworthy information can be deduced. First of all, it can be observed that in the previous measurement at higher NO_2 concentration (last graph in **Fig. 4.4**) the response drastically decreased after the first ON/OFF cycle, while in the last measurement with lower NO_2 concentrations (**Fig. 4.5** and **Fig. 4.6**) the response increases when increasing the NO_2 concentration; hence it can be deduced that, as expected, the effect of the incomplete reversibility of NO_2 adsorption is weaker in measurement with lower NO_2 concentrations than that one with higher concentrations. For the measurement with a total flow of 50 ml/min the sample response increases up to an NO_2 concentration of 15 ppm, then it seems to reach a plateau, or also a very slight decrease, thus suggesting that at this NO_2 concentration the effects of incomplete desorption start to become significant. On the contrary, when a total flux of 100 ml/min is used, the sensitivity continues to increase up to the higher tested NO_2 concentration (20 ppm). This observation suggests that the higher flow promotes a better desorption of the NO_2 molecules thus allowing a better recovery of the PL integral in comparison with the lower flow. This is also in agreement with the observation previously discussed about higher recovery slopes (that means faster recovery times) when a higher total flux is used.

It should be noticed that it is hard to make a comparison with other reports about NO_2 sensing by measurement of the PL quenching of ZnO nanostructures [195, 209]. Indeed in the cited references the visible green band was inspected for such measurements while, due to high crystal quality (as discussed in the previous chapters) of the samples deposited during the research activity presented in this thesis, the PL visible band is too weak in the investigated samples, or totally absent as in sample A600_100, to be used for these measurements. However as stated before, despite the low measured sensitivity values, the observed jumps of the PL integral of sample A600_100 in the switches between NO_2 and dry air, are sharp enough to be detected down to an NO_2 concentration of 3 ppm; lower concentrations are not testable due to limitations in the

employed experimental set-up. By a quick look to **Tab. 4.2**, it can be observed that the 3 ppm value detected with sample A600_100 represents a good value since it is comparable, or even lower, with other tested gas concentrations.

Conclusions and future progress

This Ph.D. Thesis reported the possibility to grow zinc oxide smooth and rough films and different nanostructures by using the Pulsed Laser Deposition technique without the aid of any catalyst. The study of some properties and preliminary gas sensing tests on some of the deposited samples has been reported.

After an introductory chapter presenting an overview on some interesting properties (with some more details about the photoluminescence properties) and on the growth techniques of ZnO nanostructures, the attention has been focused on the PLD of ZnO nanostructures in literature and on the depositions performed during this research activity. The study of the sample morphology by SEM inspection has been presented together with the possible growth mechanisms. In particular, an important result came from the observation of the very different morphologies obtained using two different laser wavelengths (KrF 248 nm or ArF 193 nm) to ablate the target A stronger tendency toward nanostructure growth has been observed when using the 193 nm wavelength, also at low substrate temperatures and low oxygen background pressures. A possible reason for this difference has been suggested as a consequence of the higher ArF photon energy, probably generating more energetic species depositing on the substrate. In addition, SEM investigations allowed to indicate the preferential sample growth along the c-axis of the ZnO wurtzite crystal structure.

Due to their morphology and very good crystal quality, some of these structures, like hexagonal hierarchical structures and well-aligned rod array, could be very interesting for technological applications like field emitters. Indeed their tip terminations, thus possibly enhancing the field emission efficiency thanks to local field enhancement on the tips, and their well alignment, at least in the central part of the samples, are very interesting

features for such application. In order to improve the structure alignment and thickness uniformity, suitable substrate movement can be used during the depositions.

Other samples, like well-separated hexagonal pencils, are potentially useful for chemical and biological sensing applications, due to their high surface-to-volume ratio and wide overall available surface for adsorption of gas or biological species.

Some compositional (EDS and RBS) and structural (XRD) analyses showed the good quality of the deposited samples. In particular, XRD analysis pointed out the well-alignment along the wurtzite c-axis perpendicular to the substrate surface and the presence of peaks all attributable to the ZnO wurtzite structure only. This measurement confirmed also the conclusions previously made from the morphological study about the sample growth direction.

The photoluminescence measurements at room and low (7 K) temperature confirmed the good quality of the deposited samples and in particular excellent quality, with almost totally absent defect emission bands, for some samples. The narrow excitonic peak width, the possibility to distinguish several peaks in the excitonic range and the high ratio between excitonic and defect emission intensities, were indication of this good sample quality. In addition, the origin of the peaks observed in the excitonic range (up to 13 features) has been discussed from the low temperature PL spectra and from the whole temperature dependence of the PL emission from 7 K to room temperature. The PL measurements indicated the better quality of samples deposited by ablation with the ArF excimer laser in comparison with the KrF one. Also this feature has been reasonably attributed to the higher ArF photon energy, allowing probable more energetic species depositing on the substrate (thus permitting the samples to grow with a better crystal quality), more ionized and electronically excited ablated species and a better dissociation of oxygen molecules (thus improving the reactions between the ablated species and the background gas). The study and discussion about the differences in both sample morphology and photoluminescence properties allowed to obtain a significant result about the comparison of depositions conducted by using the two considered ablating laser wavelengths.

The temperature dependence of the PL spectrum from 7 K to room temperature performed on one sample permitted to extract the Varshni parameters and to support the previously made peak assignments. In particular, by the study of the decreasing of the peak areas when increasing the sample temperature, it was possible to strengthen the assignment of the PL peaks coming from free exciton and bound exciton emission; the assignment of another peak seemed to propend toward surface exciton emission, but it could not be totally excluded also another bound exciton transition.

Finally, for some samples a preliminary study of sensing measurements based on the quenching of the PL intensity has been conducted. Some reports in literature about the study of bulk ZnO, films and nanostructures for sensing applications have been shown. Then some samples have been tested for sensing of nitrogen dioxide. Measurements at relatively high concentrations (11-114 ppm) showed a better response for nanostructured samples, with higher surface-to-volume ratio and higher overall available surface for gas molecule adsorption. However, at these concentrations, some features maybe attributable to incomplete reversibility of NO_2 adsorption have been observed. On subsequent measurements the sensing analysis revealed lower sensitivity values, maybe due to this incomplete reversibility on the NO_2 adsorption. Testing lower concentrations (down to 3 ppm) the effects of the possible partial irreversibility seemed to be less influent. Moreover, when a higher flow (100 ml/min instead of 50 ml/min) of the incoming gas in the measurement chamber has been used, faster sample response and recovery have been observed. Despite the low sensitivity values measured in the later measurements, the minimum concentration value (3 ppm) detected with one of the tested sample suggested that this sample could be promising for low-concentration detection of other gases presenting better sample responses and higher adsorption reversibility.

Thanks to the high crystal quality of the ZnO nanostructures obtained in this work by PLD, several future progresses could be explored in the field of other applications, such as field emitters etc., or in the sensing of other chemical and biological species. Additionally, further studies on the reversibility of gas adsorption or on sensing measurements based on other mechanisms (e.g. electroluminescence instead of photoluminescence) could be conducted. Furthermore, the study carried out during this work could be extended on

samples deposited by using wider ranges of the deposition parameters or by varying other parameters such as kind of substrate, use of a catalyst, and so on.

References

[1] T. Akane et al., *J. Vac. Sci. Technol. B* **18**, 1406 (2000).

[2] H. Sheng et al., *Appl. Phys. Lett.* **80**, 2132 (2002).

[3] W.Z. Xu et al., *Appl. Phys. Lett.* **88**, 173506 (2006).

[4] D.M. Bagnall et al., *Appl. Phys. Lett.* **70**, 2230 (1997).

[5] R. L. Hoffman et al., *Appl. Phys. Lett.* **82**, 733 (2003).

[6] X.G. Zheng et al., *Appl. Surf. Sci.* **253**, 2264 (2006).

[7] T. Minami et al., *Thin Solid Films* **494**, 47 (2006).

[8] Y. Li et al., *Materialstoday* **9**, 18 (2006).

[9] Y. Huang et al., *Small* **1**, 142 (2005).

[10] W.I. Park et al., *Appl. Phys. Lett.* **82**, 4358 (2003).

[11] S.H. Park, *Nanotechnology* **18**, 55608 (2007).

[12] W.I. Park and G.C. Yi, *Adv. Mater.* **16**, 87 (2004).

[13] J. Bao et al., *Nano Lett.* **6**, 1719 (2006).

[14] M.H. Huang et al., *Science* **292**, 1897 (2001).

[15] J.H. Choy et al., *Adv. Mater.* **15**, 1911 (2003).

[16] J.C. Johnson et al., *J. Phys. Chem. B* **105**, 11387 (2001).

[17] H.C. Hsu et al., *J. Appl. Phys.* **97**, 64315 (2005).

[18] H. Yan et al., *Adv. Mater.* **15**, 1907 (2003).

[19] D. Yu et al., *Appl. Phys. Lett.* **91**, 91116 (20079.

[20] E.V. Chelnokov et al., *Appl. Phys. Lett.* **89**, 171119 (2006).

[21] S.N. Cha et al., *Appl. Phys. Lett.* **89**, 263102 (2006).

[22] W.-K. Hong et al., *Appl. Phys. Lett.* **90**, 243103 (2007).

[23] M.S. Arnold et al., *J. Phys. Chem. B* **107**, 659 (2003).

[24] Z.X. Xu et al., *Appl. Phys. Lett.* **90**, 223509 (2007).

[25] C.L. Hsu et al., *Chem. Phys, Lett.* **416**, 75 (2005).

[26] H. Kind et al., *Adv. Mater.* **14**, 158 (2002).

[27] M.C. Newton et al., *Appl. Phys. Lett.* **89**, 72104 (2006).

[28] M. Law et al., *Nat. Mater.* **4**, 455 (2005).

[29] J.B. Baxter et al., *Nanotechnology* **17**, S304 (2006).

[30] W.I. Park et al., *Adv. Mater.* **17**, 1393 (2005).

[31] M. Law et al., *Science* **305**, 1269 (2004).

[32] A. Dal Corso et al., *Phys. Rev. B* **50**, 10715 (1994).

[33] S.C. Minne et al., *Appl. Phys. Lett.* **67**, 3918 (1995).

[34] S. Krishnamoorthy and A.A. Iliadis, *Solid-State Electron.* **50**, 1113 (2006).

[35] A. Kuoni et al., *J. Micromech. Microeng.* **13**, S103 (2003).

[36] N. Chong et al., *Sens. Actuators A* **96**, 231 (2002).

[37] Z.L. Wang et al., *Materialstoday* **10**, 20 (2007).

[38] Z.L Wang and J. Song, *Science* **312**, 242 (2006).

[39] X. Wang et al., *Nano Lett.* **6**, 2768 (2006).

[40] W.L. Hughes and Z.L. Wang, *Appl. Phys. Lett.* **82**, 2886 (2003).

[41] G. Wang et al., *Appl. Opt.* **40**, 5436 (2001).

[42] H. Cao et al., *Appl. Phys. Lett.* **73**, 572 (1998).

[43] M.C. Larciprete et al., *Appl. Phys. B* **82**, 431 (2006).

[44] J.C. Johnson et al., *Nano Lett.* **2**, 279 (2002).

[45] K. Ueda et al., *Appl. Phys. Lett.* **79**, 988 (2001).

[46] T. Dietl, *Semicond. Sci. Technol.* **17**, 377 (2002).

[47] D.P. Norton et al., *Thin Solid Films* **496**, 160 (2006).

[48] D. C. Look et al., *Appl. Phys. Lett.* **75** (1999).

[49] D.C. Look, *Mater. Sci. Eng. B* **80**, 383 (2001).

[50] Z.L. Wang, *Appl. Phys. A* **88**, 7 (2007).

[51] P.D. García and C. López, *J. App. Phys.* **99**, 046103 (2006).

[52] J. Cui and U. Gibson, *Nanotechnology* **18**, 155302 (2007).

[53] H. Ham et al., *Chem. Phys. Lett.* **404**, 69 (2005).

[54] R.C. Wang et al., *Appl. Phys. Lett.* **87**, 013110 (2005).

[55] Y.W. Zhu et al., *Appl. Phys. Lett.* **83**, 144 (2003).

[56] A. Wei et al., *Appl. Phys. Lett.* **88**, 213102 (2006).

[57] K. Hou et al., *Nanotechnology* **18**, 335204 (2007).

[58] H. Hu et al., *Appl. Surf. Sci.* **252**, 8410 (2006).

[59] F. Xu, *Nanotechnology* **17**, 2855 (2006).

[60] C. Li et al., *Nanotechnology* **18**, 155702 (2007).

[61] Y. Huang et al., *J. Phys.: Condens. Matter* **19**, 176001 (2007)

[62] X. Feng et al., *J. Am. Chem. Soc.* **126**, 62 (2004).

[63] X.Q. Meng et al., *Chem. Phys. Lett.* **413**, 450 (2005).

[64] F. Patolsky and C.M. Lieber, *Materialstoday* **8**, 20 (2005).

[65] X.-J. Wang and Y.-K. Choi, *Sens. Actuators B* **122**, 659 (2007).

[66] L. Schmidt-Mende and J.L. MacManus-Driscoll, *Materialstoday* **10**, 40 (2007).

[67] Ü. Özgür et al., *J. Appl. Phys.* **98**, 041301 (2005).

[68] S.J. Pearton et al., *Superlattices Microstruct.* **34**, 3 (2003).

[69] D. P. Norton et al., *Materialstoday* **7**, 34 (2004).

[70] Y. Cui et al., *Science* **293**, 1289 (2001).

[71] H.-M. Cheng et al., *Appl. Phys. Lett.* **88**, 261909 (2006).

[72] K.-F. Lin et al., *Chem. Phys. Lett.* **409**, 208 (2005).

[73] Y. Gu et al., *Appl. Phys. Lett.* **85**, 3833 (2004).

[74] B.K. Meyer et al., *Phys. Stat. Sol. (B)* **241**, 231 (2004).

[75] W. Shan et al., *Appl. Phys. Lett.* **86**, 191911 (2005).

[76] A. Teke et al., *Phys. Rev. B* **70**, 195207 (2004).

[77] K. Thonke et al., *Physica B* **308-310**, 945 (2001).

[78] A.B. Djurišić and Y.H. Leung, *Small* **2**, 944 (2006).

[79] K. Vanheusden et al., *J. Appl. Phys.* **79**, 7983 (1996).

[80] F. Leiter et al., *Physica B* **340-342**, 201 (2003).

[81] X.L. Wu et al., *Appl. Phys. Lett.* **78**, 2285 (2001).

[82] S.A. Studenikin et al., *J. Appl. Phys.* **84**, 2287 (1998).

[83] Q. Yang et al., *Appl. Phys. A* **79**, 1847 (2004).

[84] R. Dingle, *Phys. Rev. Lett.* **23**, 579 (1969).

[85] O.F. Schirmer et al., *Solid State Commun.* **8**, 1559 (1970).

[86] X. Liu et al., *J. Appl. Phys.* **95**, 3141 (95).

[87] B. Cao et al., *Appl. Phys. Lett.* **88**, 161101 (2006).

[88] D. Zhao et al., *Chem. Phys. Lett.* **399**, 522 (2004).

[89] X.Q. Wei et al., *Physica B* **388**, 145 (2007).

[90] P.S. Xu et al., *Nucl. Instrum. Methods Phys. Res. B* **199**, 286 (2003).

[91] S.A.M. Lima et al., *Int. J. Inorg. Mater.* **3**, 749 (2001).

[92] L. Wischmeier et al., *Appl. Phys. A* **84**, 111 (2006).

[93] J. Grabowska et al., *Phys. Rev. B* **71**, 115439 (2005).

[94] P.-C. Chang et al., *Appl. Phys. Lett.* **90**, 113101 (2007).

[95] M. Al-Suleiman et al., *Appl. Phys. Lett.* **89**, 231911 (2006).

[96] M.H. Huang et al., *Adv. Mater.* **13**, 113 (2001).

[97] D.C. Kim et al., *Nanotechnology* **18**, 15603 (2007).

[98] Z.L. Wang et al., *Materialstoday* **7**, 26 (2004).

[99] H. Yan et al., *Adv. Mater.* **15**, 1907 (2003).

[100] W.I Park et al., *Adv. Mater.* **14**, 1841 (2002).

[101] Y. Dai et al., *Chem. Phys. Lett.* **358**, 83 (2002).

[102] Y.H. Yang et al., *Nanotechnology* **17**, 5556 (2006).

[103] H.-M. Cheng et al., *Nanotechnology* **16**, 2882 (2005).

[104] J.-J. Wu and S.-C. Liu, *Adv. Mater.* **14**, 215 (2002).

[105] X. Liu et al., *J. Appl. Phys.* **95**, 3141 (2004).

[106] C. Liu et al., *Mater. Lett.* **60**, 1394 (2006).

[107] M.H. Wong et al., *Nanotechnology* **14**, 968 (2003).

[108] C.H. Bae et al., *Appl. Surf. Sci.* **253**, 1758 (2006).

[109] L.E. Green et al., *Inorg. Chem.* **45**, 7535 (2006).

[110] X.-L. Hu et al., *Mater. Chem. Phys.* **88**, 421 (2004).

[111] M.-T. Chen and J.-M. Ting, *Thin Solid Films* **494**, 250 (2006).

[112] T.-L. Chou and J.-M. Ting, *Thin Solid Films* **494**, 291 (2006).

[113] Y.W. Heo et al., *Appl. Phys. Lett.* **81**, 3046 (2002).

[114] M. Kawakami et al., *Jpn. J. Appl. Phys.* **42**, L33 (2003).

[115] Y. Sun et al., *Chem. Phys. Lett.* **396**, 21 (2004).

[116] L. Chen et al., *Solid State Commun.* **137**, 561 (2006).

[117] J.J. Chen et al., *Appl. Phys. Lett.* **87**, 173119 (2005).

[118] C.H. Bae et al., *Nanotechnology* **17**, 381 (2006).

[119] H.J. Fan et al., *Nanotechnology* **16**, 913 (2005).

[120] T. Hirate et al., *Superlattices Microstruct.* **42**, 409 (2007).

[121] P. Misra and L.M. Kukreja, *Thin Solid Films* **485**, 42 (2005).

[122]A. Ohtomo and A. Tsukazaki, *Semicond. Sci. Technol.* **20**, S1 (2005).

[123] M. Lorenz et al., *Appl. Phys. Lett.* **86**, 143113 (2005).

[124] J.-H. Park et al., *J. Cryst. Growth* **276**, 171 (2005).

[125] R. O'Haire et al., *Superlattices Microstruct.* **139**, 153 (2006).

[126] Y. Zhang et al., *Appl. Phys. Lett.* **87**, 133115 (2005).

[127] C. He et al., *Appl. Surf. Sci.* **254**, 2196 (2008).

[128] L. Yang et al., *Nanotechnology* **18**, 215602 (2007).

[129] Y. Ishikawa et al., *J. Colloid. Interf. Sci.* **300**, 612 (2006).

[130] A. Said et al., *Journal of Physics: Conference Series* **59**, 259 (2007).

[131] *Pulsed Laser Deposition Of Thin Films*, edited by D.B. Chrisey and G.K. Hubler (1994, John Wiley & Sons, Inc.)

[132] F. Claeyssens et al., *J. Appl. Phys.* **92**, 6886 (2002).

[133] A.B. Hartanto et al., *Appl.Phys. A* **78**, 299 (2004).

[134] T. Okada et al., *Appl. Phys. A* **79**, 1417 (2004).

[135] T. Okada et al., *Appl. Phys. A* **81**, 907 (2005).

[136] T. Okada et al., *Jpn. J. Appl. Phys.* **44**, 688 (2005).

[137] T. Okada et al., *Thin Solid Films* **506-507**, 274 (2005).

[138] Y. Sun et al., *Superlattices Microstruct.* **39**, 33 (2006).

[139] Y. Sun et al., *Chem. Phys. Lett.* **447**, 257 (2007).

[140] S. Choopun et al., *J. Cryst. Growth* **274**, 167 (2005).

[141] Z.W. Liu et al., *Appl. Phys. Lett.* **88**, 53110 (2006).

[142] V. Gupta et al., *Mat. Res. Soc. Symp. Proc.* **818**, M8.26.1 (2004).

[143] V. Gupta et al., *J.Cryst.Growth* **287**, 39 (2005).

[144] J. Zúñiga-Pérez et al., *Nanotechnology* **18**, 195303 (2007).

[145] I. Ozerov et al., *Appl. Surf. Sci.* **247**, 1 (2005).

[146] G. Jeffers et al., *J. Appl. Phys.* **75**, 5016 (1994).

[147] F. Aubriet et al., *Appl. Surf. Sci.* **186**, 282 (2002).

[148] B.D. Yao et al., *Appl. Phys. Lett.* **81**, 757 (2002).

[149] A. Sambri et al., *Appl. Phys. Lett.* **91**, 151501 (2007).

[150] Y.H. Yang et al., *Nanotechnology* **17**, 5556 (2006).

[151] L.R. Doolittle, *Nucl. Instr. Meth. B* **9**, 344 (1985).

[152] R.C. Wang et al., *Appl. Phys. Lett.* **86**, 251104 (2005).

[153] P. Brix and G. Herzberg, *J. Chem. Phys.* **21**, 2240 (1953).

[154] W.I. Park et al., *Appl. Phys. Lett.* **82**, 964 (2003).

[155] C. Li et al., *Nanotechnology* **17**, 3740 (2006).

[156] Y.P. Varshni, *Physica* **34**, 149 (1967).

[157] S.M. Sze, *Semiconductor Devices* (Wiley, New York, 1985)

[158] J.I. Pankove, *Optical Processes in Semiconductors* (Dover, New York, 1975).

[159] Landolt-Börnstein, *Numerical Data and Functional Relationships in Science and Technology*, Gp. III, Vol. 17 b.

[160] A.B. Djurišić et al., *Appl. Phys. Lett.* **88**, 103107 (2006).

[161] V.V. Ursaki et al., *Phys. Rev. B* **70**, 155204 (2004).

[162] X.H. Zhang et al., *Appl. Phys. Lett.* **90**, 13107 (2007).

[163] V.A. Fonoberov et al., *Phys. Rev. B* **73**, 165317 (2006).

[164] D.J. Sirbuly et al., *J. Phys. Chem. B* **109**, 15190 (2005).

[165] L. Wang and N.C. Giles, *J. Appl. Phys.* **94**, 973 (2003).

[166] A. Jones et al., *Sens. Actuators* **5**, 75 (1984).

[167] P. Mitra et al., *Mater Lett.* **35**, 33 (1998).

[168] E.J. Cho and F.V. Bright, *Anal. Chem.* **73**, 3289 (2001).

[169] V. Savvate'ev et al., *Appl. Phys. Lett.* **81**, 4652 (2002).

[170] J.W. Aylott et al., *US Patent* No. 6,331,438 (December 2001).

[171] B. Choudhury et al., *J. Appl. Phys.* **96**, 2949 (2004).

[172] B.S. Kang et al., *Appl. Phys. A* **80**, 259 (2005).

[173] P.D. Batista and M. Mulato, *Appl. Phys. Lett.* **87**, 143508 (2005).

[174] J. Homola et al., *Sens. Actuators B* **54**, 3 (1999).

[175] Y. Zhang et al., *Physica B* **368**, 94 (2005).

[176] K.D. Mitzner et al., *Sens. Actuators B* **93**, 92 (2003).

[177] B. Bott et al., *Sens. Actuators* **5**, 65 (1984).

[178] H. Nanto et al., *J. Appl. Phys.* **60**, 482 (1986).

[179] L.C. Tien et al., *Appl. Phys. Lett.* **87**, 222106 (2005).

[180] S. Basu and A. Dutta, *Mater. Chem. Phys.* **47**, 93 (1997).

[181] A.A. Tomchenko et al., *Sens. Actuators B* **93**, 126 (2003).

[182] L.-J. Bie et al., *Sens. Actuators B* **126**, 604 (2007).

[183] C.C. Li et al., *Appl. Phys. Lett.* **91**, 32101 82007).

[184] C.S. Rout et al., *Chem. Phys. Lett.* **418**, 586 (2006).

[185] C.S. Rout et al., *Solid State Commun.* **138**, 136 (2006).

[186] H.T Wang et al., *Appl.Phys. Lett.* **86**, 243503 (2005).

[187] H.T. Wang et al., *Appl. Phys. A* **81**, 1117 (2005).

[188] J.X. Wang et al., *Nanotechnology* **17**, 4995 (2006).

[189] J. Yang et al., *Appl. Phys. Lett.* **90**, 103109 (2007).

[190] C.S. Rout et al., *Nanotechnology* **18**, 205504 (2007).

[191] X. Jiaqiang et al., *Sens. Actuators. B* **113**, 526 (2006).

[192] E. Comini et al., *Appl. Phys. A* **88**, 45 (2007).

[193] C. Wang et al., *Sens. Actuators B* **113**, 320 (2006).

[194] D. Wang et al., *Nanotechnology* **18**, 185601 (2007).

[195] G. Sberveglieri et al., *Sens. Actuators B* **121**, 208 (2007).

[196] B. Baruwati et al., *Sens. Actuators B* **119**, 676 (2006).

[197] Y. Chen et al., *Nanotechnology* **17**, 4537 (2006).

[198] T. Gao and T.H. Wang, *Appl. Phys. A* **80**, 1451 (2005).

[199] T.-J. Hsueh et al., *Sens. Actuators B* **126**, 473 (2007).

[200] Y. Lv et al., *Physica E* **36**, 102 (2007).

[201] Q. Wan et al., *Appl. Phys. Lett.* **84**, 3654 (2004).

[202] C. Xiangfeng et al., *Chem. Phys. Lett.* **401**, 426 (2005).

[203] N.V. Hieu and N.D. Chien, *Physica B* **403**, 50 (2008).

[204] Y.J. Chen et al., *Sens. Actuators B* **129**, 639 (2008).

[205] V.R. Shinde et al., *Mat. Sci. Eng. B* **137**, 119 (2007).

[206] B.S. Kang et al., *Appl. Phys. Lett.* **86**, 112105 (2005).

[207] Z. Fan and J.G.Lu, *Appl. Phys. Lett.* **86**, 123510 (2005).

[208] Z. Fan et al., *Appl. Phys. Lett.* **85**, 5923 (2004).

[209] A. Bismuto et al., J. Opt. A: Pure Appl. Opt. **8**, S585 (2006).

[210] L. Peng et al., Appl. Surf. Sci. **254**, 2856 (2008).

[211] C. de Julián Fernández et al., *Sens. Actuators B* **130**, 531 (2008).

[212] X. Wang et al., *Appl. Surf. Sci.* **252**, 2404 (2006).

[213] J.X. Wang et al., *Appl. Phys. Lett.* **88**, 233106 (2006).

[214] A. Wei et al., *Appl. Phys. Lett.* **89**, 123902 (2006).

[215] F. Zhang et al., *Anal. Chim. Acta* **519**, 155 (2004).

List of publications

- D. Valerini, A. P. Caricato, M. Lomascolo, F. Romano, A. Taurino, T. Tunno, M. Martino, *Zinc oxide nanostructures grown by pulsed laser deposition*, accepted for publication on Applied Physics A
- M. Martino, A.P. Caricato, F. Romano, T. Tunno, D. Valerini, M. Anni, M.E. Caruso, A. Romano, T. Verri, *Pulsed laser deposition of organic and biological materials*, in press on J. Mater. Sci.: Mater. Electron. (2008)
- A.P. Caricato, S. Capone, G. Ciccarella, R. Rella, F. Romano, J. Spadavecchia, A. Taurino, T. Tunno, D. Valerini, M. Martino, *TiO_2 nanoparticle thin film deposition by matrix assisted pulsed laser evaporation for sensing applications*, Appl. Surf. Sci. **253**, 7937 (2007)
- A.P. Caricato, M.G. Manera, R. Rella, F. Romano, J. Spadavecchia, T. Tunno, D. Valerini, M. Martino, *Uniform thin films of TIO_2 nanoparticles deposited by Matrix-assisted Pulsed Laser Evaporation*, Appl. Surf. Sci. **253**, 6471 (2007)
- T. Tunno, A.P. Caricato, M. E. Caruso, A. Luches, M. Martino, F. Romano, D. Valerini, M. Anni, *Matrix-assisted pulsed laser evaporation of polyfluorene thin film*, Appl. Surf. Sci. **253**, 6461 (2007)
- A.P. Caricato, M. Fernàndez, G. Leggieri, M. Martino, F. Romano, T. Tunno, D.Valerini, A. Luches, *Reactive pulsed laser deposition of gold nitride thin films*, Appl. Surf. Sci. **253**, 8037 (2007)
- A. Luches, S.A. Mulenko, V.P. Veiko, A.P. Caricato, V.A Chuiko, Y.V. Kudryavtsev, A.V. Lopato, A.A. Petrov, F. Romano, D. Valerini, *Laser-assisted synthesis of semiconductor chromium disilicide films*, Appl. Surf. Sci. **253**, 6512 (2007)

- A.P. Caricato, M. Catalano, G. Ciccarella, R. Rella, F. Romano, J. Spadavecchia, A. Taurino, T. Tunno, D.Valerini, M. Martino, *Matrix Assisted Pulsed Laser Evaporation for TiO_2 nanoparticle thin film deposition*, Digest Journal of Nanomaterials and Biostructures **1**, 43 (2006)

- D. Valerini, A. Cretí, M. Lomascolo, L. Manna, R. Cingolani, and M. Anni, *Temperature dependence of the photoluminescence properties of colloidal CdSe/ZnS core/shell quantum dots embedded in a polystyrene matrix*, Phys. Rev. B **71**, 235409 (2005). Published also on:
  - Virtual Journal of Nanoscale Science & Technology, vol. 11, issue 25
  - Virtual Journal of Ultrafast Science, vol. 4, issue 7

- M. Anni, L. Manna, R. Cingolani, D. Valerini, A. Cretí, and M. Lomascolo, *Förster energy transfer from blue-emitting polymers to colloidal CdSe/ZnS core/shell quantum dots*, Appl. Phys. Lett. **85**, 4169 (2004) + *Erratum* Appl. Phys. Lett. **88**, 259901 (2006). Published also on:
  - Virtual Journal of Nanoscale Science & Technology, vol. 10, issue 20
  - Virtual Journal of Ultrafast Science, vol. 3, issue 12

Acknowledgements - Ringraziamenti

English version

Firstly the formal acknowledgements regarding the research activity of this Thesis.

I wish to thank my tutors Prof. Maurizio Martino and Dr. Mauro Lomascolo for the possibility they offered me to work and learn during these three years. Of course, together with them, I am grateful to all people I worked with: Dr. Anna Paola Caricato, Dr. Arianna Cretì, Dr. Tiziana Tunno, Dr. Francesco Romano and Dr. Elisabetta Caruso. Thanks are due to the wise Prof. Armando Luches too, for useful suggestions. I am very grateful to Massimo Corrado for the realization of the substrate heater and for all the other "gadgets" and helps in the laboratory. Many thanks to Dr. Francesco Romano and Prof. Giuseppe Majni for RBS measurements and to Prof. Gilberto Leggieri for RUMP simulations, to Dr. Anna Caricato and Dr. Marcella D'Elia for EDS measurements, to Donato Cannoletta for XRD measurements. Many thanks to Flavio Casino for the gas sensing set-up and to all other persons helping and/or following me at IMM-CNR in Lecce: Dr. Roberto Rella, Dr. Massimo Catalano, Dr. Pietro Siciliano; very particular thanks to Dr. Antonietta Taurino for all teaching and assistance in SEM measurements and for her continuous kindness. Finally I am grateful to all other persons I certainly forgot to mention above although they helped me somehow.

Now the informal acknowledgements.

Many people mentioned in the previous acknowledgments must be here too. I'm grateful to Mauro and Arianna for bearing me also when it seemed impossible. I'm very grateful to Anna Paola, Tiziana, Francesco and Elisabetta for the same reason, and for all funny breaks, discussions (in particular the non-scientific ones) and so on; in particular a lot of thanks are due to Francesco (this is the fourth time I thank him here! how many

times will he thank me in his Thesis?), since he's perhaps the one who had to bear me more during these three years at the university. Many thanks to all the other friends at the university for having fun, cakes, soccer, and so on... mmm and sometimes maybe some physics too.

Giant thanks to my company outside the university, in particular my brother Davide, Cinzia, Katya, David, Marco and Mauro, for all fun during the period of this Thesis, and for much more else.

Endless thanks to all those with whom I spent a lot of relaxing, funny and really pleasant moments, allowing me to take lots of truly nice breaks, mainly during the writing of this Thesis. I would have liked to spend more and more of these moments again, and even far better... → these dots are full of meanings.

Again some thanks are due to those I forgot to mention here.

Finally, the most important thanks are to my family for all support and nice moments: Massy, Davide, Cinzia, Rosy, Gabriele... and my greatest gratefulness is to my parents, since thanks to them I could reach this goal.

Versione italiana

(Solo ringraziamenti informali)

Tantissimi ringraziamenti a Mauro e Arianna per avermi sopportato anche quando sembrava impossibile. Grazie mille ad Anna Paola, Tiziana, Francesco ed Elisabetta per lo stesso motivo, e per tutti i momenti divertenti, le discussioni (in particolare quelle di carattere non scientifico) ecc.; un ringraziamento particolare a Francesco (e questa è la quarta volta che lo ringrazio, anzi la sesta se considero anche i due ringraziamenti in italiano! quante volte mi ringrazierà nella sua Tesi?), poiché probabilmente è stato quello che ha dovuto sopportarmi di più in questi tre anni in università. Tantissime grazie a tutti gli altri amici dell'università per i divertimenti, le torte, il calcetto ecc... mmm ("mmm" si

dice allo stesso modo in italiano e inglese? boh) e ogni tanto forse anche per qualcosina di fisica.

Dei ringraziamenti immensi vanno alla compagnia al di fuori dell'università, in particolare "fraima" Davide, Cinzia, Katya, David, Marco e Mauro, per tutto il divertimento trascorso in questo periodo e per tantissimo altro.

Infiniti ringraziamenti a chi mi ha fatto trascorrere tantissimi momenti rilassanti, divertenti e sinceramente piacevoli, pause belle, ma belle davvero, durante la scrittura della Tesi. Mi sarebbe piaciuto tantissimo trascorrere ancora una marea di momenti come questi, e anche molto migliori... → questi puntini di sospensione sono pienissimi di significato.

Ovviamente faccio i ringraziamenti anche a chi ho dimenticato di citare qui.

Per ultimi i ringraziamenti più importanti, quelli alla mia famiglia, per il supporto e i bei momenti: Massy, Davide, Cinzia, Rosy, Gabriele... e la gratitudine più grande è per i miei genitori, grazie ai quali ho potuto raggiungere anche quest'obiettivo.